

# **Thermal MEMS Gyroscope Design and Characteristics Analysis**

by

**Nilgoon Zarei**

B.Sc., Shiraz University, 2009

Thesis Submitted in Partial Fulfillment  
of the Requirements for the Degree of  
Master of Applied Science

in the

School of Engineering Science  
Faculty of Applied Science

© **Nilgoon Zarei 2013**

**SIMON FRASER UNIVERSITY**

**Spring 2013**

All rights reserved.

However, in accordance with the *Copyright Act of Canada*, this work may be reproduced, without authorization, under the conditions for "Fair Dealing." Therefore, limited reproduction of this work for the purposes of private study, research, criticism, review and news reporting is likely to be in accordance with the law, particularly if cited appropriately.

# Approval

**Name:** Nilgoon Zarei  
**Degree:** M.A.Sc  
**Title of Thesis:** Thermal MEMS Gyroscope Design and Characteristics Analysis

**Examining Committee:**

Chair: **Andrew Rawicz**  
Professor

---

**Albert Leung**  
Senior Supervisor  
Professor

---

**John Jones**  
Senior Supervisor  
Associate Professor

---

**Ash Parameswaran**  
Supervisor  
Professor

---

**Behraad Bahreyni**  
Internal Examiner  
Associate Professor

---

**Date Defended:** 22 Jan 2013

---

## Partial Copyright Licence



The author, whose copyright is declared on the title page of this work, has granted to Simon Fraser University the right to lend this thesis, project or extended essay to users of the Simon Fraser University Library, and to make partial or single copies only for such users or in response to a request from the library of any other university, or other educational institution, on its own behalf or for one of its users.

The author has further granted permission to Simon Fraser University to keep or make a digital copy for use in its circulating collection (currently available to the public at the "Institutional Repository" link of the SFU Library website ([www.lib.sfu.ca](http://www.lib.sfu.ca)) at <http://summit/sfu.ca> and, without changing the content, to translate the thesis/project or extended essays, if technically possible, to any medium or format for the purpose of preservation of the digital work.

The author has further agreed that permission for multiple copying of this work for scholarly purposes may be granted by either the author or the Dean of Graduate Studies.

It is understood that copying or publication of this work for financial gain shall not be allowed without the author's written permission.

Permission for public performance, or limited permission for private scholarly use, of any multimedia materials forming part of this work, may have been granted by the author. This information may be found on the separately catalogued multimedia material and in the signed Partial Copyright Licence.

While licensing SFU to permit the above uses, the author retains copyright in the thesis, project or extended essays, including the right to change the work for subsequent purposes, including editing and publishing the work in whole or in part, and licensing other parties, as the author may desire.

The original Partial Copyright Licence attesting to these terms, and signed by this author, may be found in the original bound copy of this work, retained in the Simon Fraser University Archive.

Simon Fraser University Library  
Burnaby, British Columbia, Canada

revised Fall 2011

## **Abstract**

Thermal MEMS gyroscope characteristics have been studied to optimize gyroscope performance. Different parameters such as gas properties, heaters power and switching frequency have been optimized to increase the device sensitivity.

A new Thermal MEMS gyroscope model referred to as “Forced Convection MEMS Gyroscope” has been introduced. In this design the output signal has been increased by adding external force to the system. Parameter optimization to increase the device efficiency has also been investigated. An experimental set up has been presented and the simulation study compared with experimental results.

Another model referred to as the “Three-axis MEMS gyroscope” has been defined to measure rotation along three axes of rotation. In this design a single heater replaces the two heaters of previous models. Simulation results have shown that using this design it may be possible to distinguish the rotation signal from the buoyancy effects associated with acceleration.

**Keywords:** Thermal MEMS Gyroscope; Coriolis Effect; Forced convection

## **Acknowledgements**

I would like to express my sincere gratitude to both my senior supervisors, Dr. Albert Leung and Dr. John Jones, for their kind supervision and guidance through two years of my master program. I cannot find words to express my appreciation toward them. I will be grateful for all of their help and support for the rest of my life. They are both among the most important people in my academic life.

My special thanks go to Dr. Ash Parameswaran, he encouraged and inspired me a lot and I am grateful for his valuable time that he allocated to me and it is my pleasure to have him in my master committee.

I am grateful to have Dr. Behraad Bahreyni as my thesis internal examiner and I want to thank him for giving me access to his research equipment.

With all of my heart, I want to thank my mother, Zohreh, who helped make my dream of successfully completing my master degree at Simon Fraser University come true.

I will forever be grateful to my best friend ,Mehdi, who although far away was always supportive; he inspired me a lot and he is the best role model for me.

I would like to specially thank my other best friend, Sam, for his unconditional help and endless care. He always stands by my side,there is no words to convey how much he helped me.

Also, I would like to thank Kourosh, Sadegh, Alireza and Rui Fang for their technical support throughout the years of my master studies.

## **Dedication**

To my mother Zohreh-The dearest person in my life.

# Table of Contents

Approval.....	ii
Partial Copyright Licence .....	iii
Abstract.....	iv
Acknowledgements .....	v
Dedication .....	vi
Table of Contents.....	vii
List of Tables.....	ix
List of Figures.....	x
List of Symbols.....	xiii
<b>1. Introduction .....</b>	<b>1</b>
1.1. Background.....	1
1.2. Thermal MEMS Gyroscope Technical Background.....	3
<b>2. Simulation Design .....</b>	<b>6</b>
2.1. COMSOL Simulation .....	8
2.2. Angular Rate, $\omega$ , and Gyroscope Sensitivity .....	15
<b>3. Design and Analysis of Micromachined Thermal Gyroscope .....</b>	<b>17</b>
3.1. Overview .....	17
3.2. Impact of Pressure on Sensitivity.....	17
3.3. Heater Switching Frequency and Gyroscope Sensitivity .....	19
3.4. Gas Velocity, $u$ , Monitoring by Varying Density .....	20
3.5. Viscosity Analysis .....	24
3.6. Ekman Number and Gyro Sensitivity .....	25
3.7. Changing Heater Power and Gas Velocity Monitoring .....	27
3.8. Signal-to-Interference Ratio (SIR) Discussion of Thermal MEMS Gyroscope .....	31
3.9. Conclusion and Discussion.....	39
<b>4. Forced-Convection Gyroscope .....</b>	<b>41</b>
4.1. Introduction .....	41
4.2. Forced-Convection Design, One heater.....	42
4.3. Forced-Convection Design, Two heaters.....	46
4.4. Fabrication .....	49
4.5. Heated-Sensor Design .....	51
4.6. Signal Correction.....	53
4.7. Conclusion .....	55
4.8. Future work .....	56
<b>5. Three-Axis MEMS Gyroscope.....</b>	<b>57</b>
5.1. Simulation Design .....	57
5.2. Gravity/Acceleration Effect .....	66
5.3. Conclusion .....	70
5.4. Future Work.....	70

<b>6. Conclusion and Future Work.....</b>	<b>71</b>
<b>References.....</b>	<b>73</b>
<b>Appendix.....</b>	<b>77</b>



## List of Tables

Table 1 Physical parameters of SF <sub>6</sub> and air used in the model .....	11
Table 2 Physical parameters of Silicon used in the model .....	11
Table 3 Temperature sensor locations in three-dimensional model .....	61
Table 4 Simulation results of different rotation cases.....	65
Table 5 Simulation results of different rotation cases.....	68

## List of Figures

Figure 1-1 Gyroscope different categories.....	3
Figure 1-2 Thermal Gyroscope operation with no rotation (a) and with rotation (b) [19] .....	4
Figure 1-3 Top view of thermal gyroscope structure <sup>[19]</sup> .....	5
Figure 2-1 COMSOL model showing the cavity, heaters, and temperature sensors.....	9
Figure 2-2 Two-D COMSOL mesh representing the gyro .....	10
Figure 2-3 Modelling air flow (a) with no rotation or gas bubble deviation, and (b) with rotation and gas bubble deviation .....	12
Figure 2-4 Device structure showing places of temperature sensors .....	13
Figure 2-5 Temperature variation of top sensor.....	14
Figure 2-6 Temperature difference monitored between the two temperature sensors.....	14
Figure 2-7 $\Delta TI$ monitoring for different values of $\omega$ , cavity filled with air .....	15
Figure 3-1 Average $\Delta TI$ versus Pressure, cavity filled with $SF_6$ .....	18
Figure 3-2 Average $\Delta TI$ versus Pressure, cavity filled with air .....	19
Figure 3-3 Comparing average of $\Delta TI$ in two cases, switching frequency equal to 12 Hz, blue curve, and switching frequency equal to 6 Hz, red dashed curve, cavity filled with air .....	20
Figure 3-4 (a) Monitoring $u$ in the middle of cavity, $P = 100$ kPa.....	21
Figure 3-5 Average $ u $ versus Pressure, cavity filled with $SF_6$ .....	22
Figure 3-6 (a) $u$ in the middle of cavity, $P = 100$ kPa .....	23
Figure 3-7 Average $ u $ versus Pressure, cavity filled with air .....	24
Figure 3-8 Average $\Delta TI$ versus viscosity (air & $SF_6$ ) .....	25
Figure 3-9 Average $\Delta TI$ versus Power (air).....	27
Figure 3-10 Average $TH_1$ versus Power (air) .....	28
Figure 3-11 Average $ u $ versus Power, (air) .....	28

Figure 3-12 Average $\Delta T_I$ versus Power, $SF_6$ .....	29
Figure 3-13 Average $TH_1$ versus power, $SF_6$ .....	30
Figure 3-14 Average $I_{ul}$ versus power, $SF_6$ .....	30
Figure 3-15 Average $I_{ul}$ versus power, dashed and solid curves represent $SF_6$ and air respectively .....	31
Figure 3-16 COMSOL Model, places of temperature sensors and heaters are shown .....	34
Figure 3-17 Temperature difference is monitored while the impact of gravity is eliminated, Thermal Gyroscope.....	35
Figure 3-18 Gyroscope different orientations while gravity is applied .....	36
Figure 3-19 Temperature difference is monitored while the impact of gravity is considered, and $\Phi = 90$ . Thermal Gyroscope.....	37
Figure 3-20 Temperature difference is monitored while the impact of gravity is considered, and $\Phi = 45$ Thermal Gyroscope .....	38
Figure 4-1 COMSOL Model, deviated gas due to rotation is shown.....	42
Figure 4-2 Boundary condition of Forced-convection design .....	44
Figure 4-3 Wall speed optimization .....	45
Figure 4-4 Temperature sensor location optimization .....	46
Figure 4-5 COMSOL model, places of temperature sensors, heaters and oscillating flow are shown, forced-convection design .....	47
Figure 4-6 Temperature difference is monitored while the impact of gravity is eliminated, Forced convection Gyroscope, Heater-sensor model .....	48
Figure 4-7 Temperature difference is monitored while the impact of gravity is considered, Forced convection Gyroscope, Heater-sensor model .....	48
Figure 4-8 Device mask layout.....	50
Figure 4-9 MEMS fabricated chip with copper tube .....	50
Figure 4-10 Setup for detecting sensors functionality .....	51
Figure 4-11 New Gyro design based on hot sensors .....	52
Figure 4-12 Output signal with different angular rate .....	53

Figure 4-13 Temperature difference is monitored while the impact of gravity is considered, Forced convection Gyroscope, Heated-sensor model.....	54
Figure 4-14 Temperature difference of heated-sensor design, different values of $\theta$ are considered .....	55
Figure 5-1 Deviation of a warm fluid bubble in One-heater Thermal Gyroscope .....	57
Figure 5-2 COMSOL structure, constructed from small cubes.....	58
Figure 5-3 COMSOL structure, shows the heater in a plus shape .....	59
Figure 5-4 Places of temperature sensors in three-dimensional model based on optimization .....	60
Figure 5-5 Temperature difference between two temperature sensors, for detecting rotation along x axis .....	62
Figure 5-6 (a) Temperature difference between two temperature sensors, for detecting rotation along y axis .....	63
Figure 5-7 Temperature difference between two sensors, for detecting rotation along y axis.....	64
Figure 5-8 Two-dimensional Thermal gyro model, gravity is added to the model.....	67
Figure 5-9 Simulation results of Thermal Gyroscope in the rotation case, $\omega = 40$ rad/s, and $\theta = 1^\circ$ .....	69

## List of Symbols

$c$	Specific heat
$k$	Thermal conductivity
$R$	Gas constant
$T$	Temperature
$u$	Velocity in $x$ direction
$v$	Velocity in $y$ direction
$w$	Velocity in $z$ direction
$x$	Cartesian coordinate
$y$	Cartesian coordinate
$z$	Cartesian coordinate
$a_x$	Acceleration in $x$ direction
$a_y$	Acceleration in $y$ direction
$a_z$	Acceleration in $z$ direction
$\omega_x$	Rotation frequency about $x$ axis
$\omega_y$	Rotation frequency about $y$ axis
$\omega_z$	Rotation frequency about $z$ axis
$\alpha$	Thermal diffusivity
$\beta$	Coefficient of expansion
$\mu$	Dynamic viscosity
$\rho$	Density

# 1. Introduction

## 1.1. Background

A gyroscope is a sensor that measures angular rate or speed of rotation. The gyroscope has a very long history and wide range of applications, for example in aircraft, satellites, automobiles, mobile phones, cameras and video-game controllers [1-3].

As early as the 14<sup>th</sup> century this device was used as a children's toy and in the 19<sup>th</sup> century scientists started to use gyroscopes to monitor angular rotation relative to an inertial frame of reference. The gyroscope was first used to measure the Earth's rotation at that time [4].

The first generation of gyroscopes, referred to as "Wheel Gyroscopes", consisted of a wheel that freely rotates and resists any rotation variations [4-5]. This rotating wheel has many disadvantages such as wearing and bearing friction [6].

A second category of gyroscopes, referred to as "Vibrating structure gyroscopes", achieve better reliability by replacing the wheel with a vibrating structure, thus eliminating the previous problems [7]. However, in this gyroscope there are still some mechanical problems such as stress induced by vibration. An example of this type of gyroscope is the Hemispherical Resonator Gyroscope (HRG).

An alternative technology, based on the Sagnac effect [8], results in a more effective and high performance device. Examples of this type of optical gyroscope are Fiber-Optic Gyroscope (FOG) and Ring Laser Gyroscope (RLG) [9]. In these gyroscopes all mechanical limitations such as wearing, friction and shock sensitivity have been completely eliminated [6]. However, they are expensive and bulky and thus not widely applicable, especially in places where size and cost are critical issues.

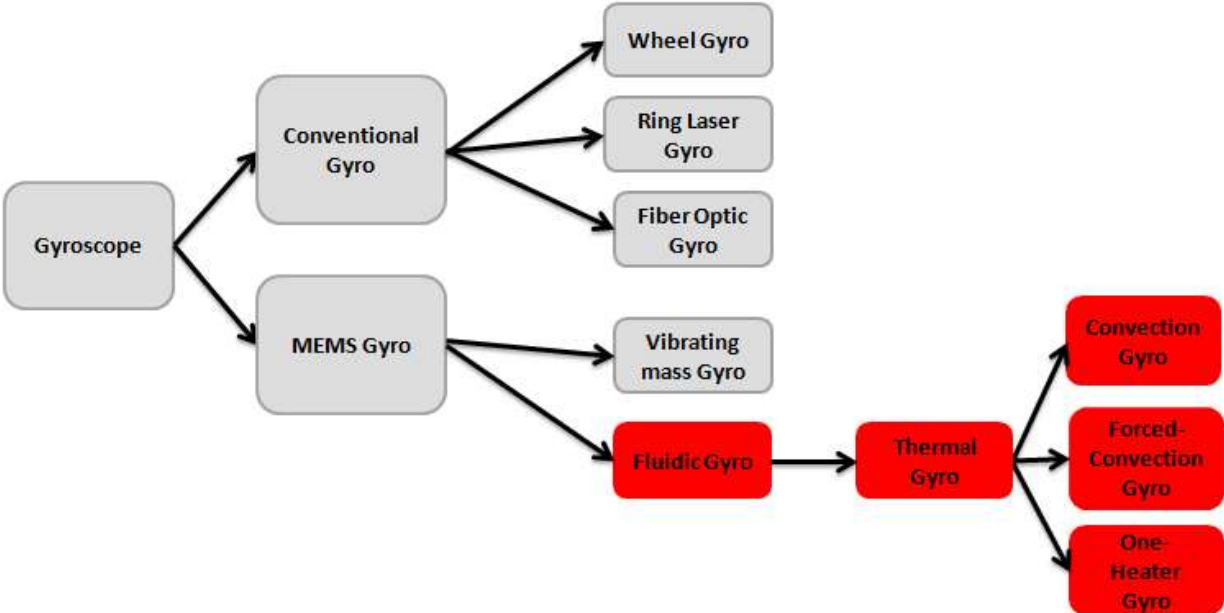
Around 1991 micromechanical gyroscopes emerged as an alternative technology with lower price and smaller size [10]. Microelectromechanical systems (MEMS) is an interdisciplinary technology that combines electrical and mechanical systems at very small scale,  $10^{-3}$  to  $10^{-6}$  m. Different devices that perform both electrical and mechanical functions on micro scales have been fabricated using photolithography and other techniques. These devices are classed as MEMS [6,11]. Micromachined gyroscope resolution has been improved significantly over the past few decades [12]. This type of gyroscope has been commercialized widely and, in comparison with previously designed gyroscopes, the cost has been reduced significantly. The fundamental operation of most micromachined gyroscopes is the measurement of the capacitance change induced by rotation between a vibrating silicon sensing element and a stationary silicon beam, where both are attached to a substrate [6,13]. This type of gyroscope is referred to as a "Vibrating mass gyroscope". Micromachined gyroscopes require both an actuating and a sensing mechanism. In many applications electrostatic actuation and capacitive sensing are used [6]. Robustness issues such as shock resistance, mechanical strength and the tendency of the vibrating element to stick to the substrate are among the important problems that need to be addressed in vibrating mass gyroscopes [14].

A new generation of micromachined gyroscopes, referred to as "Fluidic Gyroscopes", overcomes some of the issues that vibrating mass gyroscopes are encountering [15-18]. Different techniques [15-16] and various fluids such as water [16] have been used in the fluidic gyroscope to increase the device sensitivity. For example, in a few fluid gyroscopes pressure differences induced by the centrifugal force of rotation have been measured [15]. In more recent designs of Fluidic Gyroscope, a thermal accelerometer [21] and Coriolis mass flow meter are combined [23]. This new design of gyroscope, referred to as "Thermal MEMS Gyroscope", shows high shock resistance. The vibrating parts used in inertial gyroscopes have been eliminated. This device does not face mechanical issues such as wearing and as a result is more reliable [16, 21, 22]. The Thermal MEMS Gyroscope [21-22] has also some limitations. For example, in the presence of acceleration or a gravity field, an acceleration signal will interfere with the rotation signal and it is a challenge to distinguish the two.

In this thesis, modeling and analysis of different designs of Thermal MEMS gyroscope has been performed using the COMSOL Multiphysics software package. Different methods have been demonstrated for increasing the output signal of the device. Finding a technique to increase the range of thermal MEMS gyroscope reliability motivated us to come up with a design that we will

refer to as the "Forced Convection MEMS gyroscope ". The analysis of this design is explained in chapter 4. Furthermore, contemporary designed Thermal MEMS gyroscopes show some incapability of detecting rotation along three axes. This could be considered one of the major limitations of Thermal MEMS gyroscopes. In chapter 5 a three-dimensional finite-element model of the device is developed to investigate three-axis rotation detection. The effect of acceleration signal on this device is also investigated and we study some techniques for suppressing this interference.

Figure 1-1 shows different gyroscope categories.



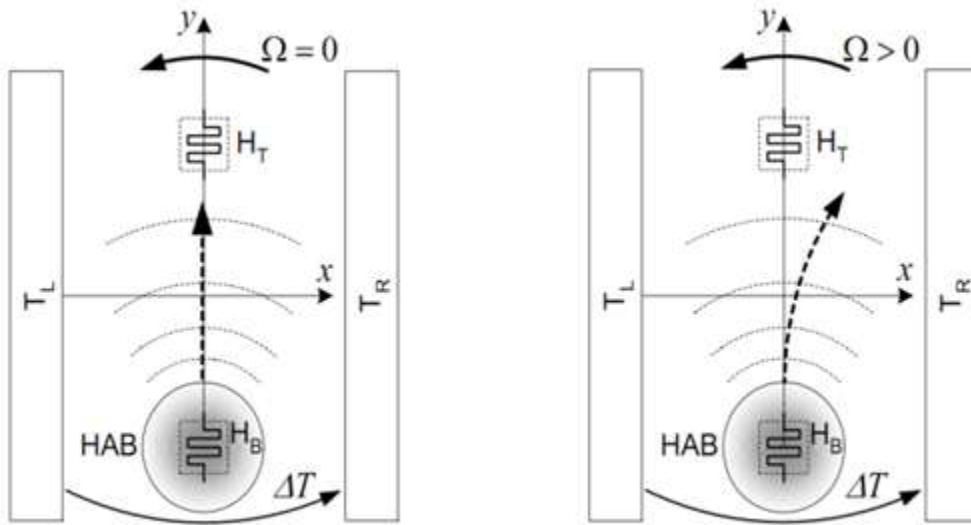
*Figure 1-1 Gyroscope different categories*

**1.2. Thermal MEMS Gyroscope Technical Background**

The operating principle of the Thermal MEMS gyroscope is the deflection of a current of moving hot fluid by the Coriolis force. The Coriolis force refers to the appearance of an object in rectilinear motion being deflected from its course if observed from an accelerating or rotating



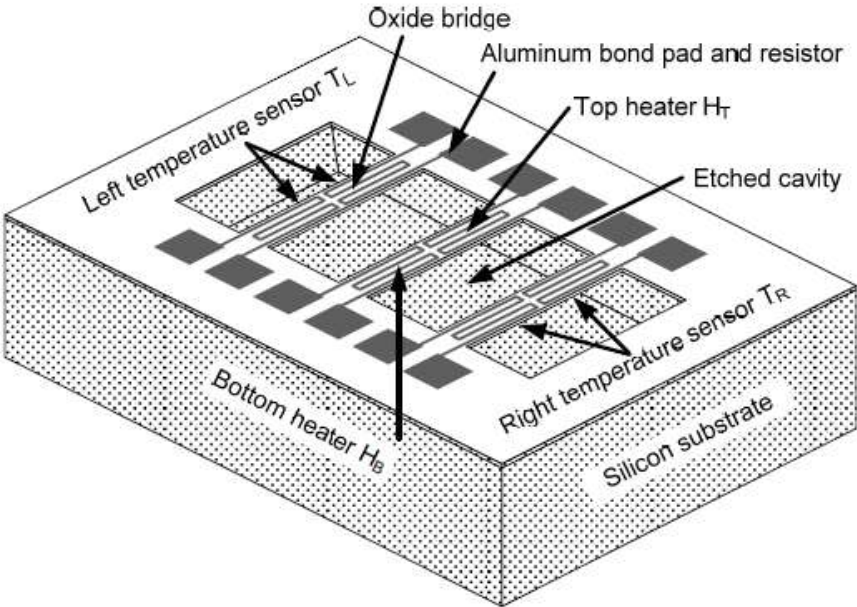
frame of reference. The Coriolis force is sometimes referred to as a “fictitious” force, since it disappears when the physics of the situation are described within an inertial frame of reference. Nevertheless, we find it convenient to describe the gyroscope’s operation from a frame of reference that rotates with the gyroscope and includes the Coriolis force. The same results could be obtained by describing its operation from an inertial frame, but such a description would be more cumbersome and less intuitive. In the Thermal MEMS gyroscope developed at Simon Fraser University [19], a flow of warm fluid is generated by heating the gas inside a micromachined cavity. The cavity is flanked by two temperature sensors,  $T_L$  and  $T_R$ . In the absence of rotation, the warm flow is symmetrically placed with respect to the two sensors and both will record the same temperature, Figure 1-2 (a). If rotation occurs, the Coriolis force will divert the flow to one side or the other, and a temperature differential between the two sensors will appear [19, 20, 22] as shown in Figure 1-2 (b), [19].



(a) Thermal Gyroscope : with no rotation      (b) Thermal Gyroscope: with rotation

**Figure 1-2 Thermal Gyroscope operation with no rotation (a) and with rotation (b) [19]**

The top view of thermal gyroscope structure is shown in Figure 1-3. Locations of heaters and sensors are shown in this figure.



**Figure 1-3 Top view of thermal gyroscope structure<sup>[19]</sup>**

## 2. Simulation Design

In order to predict the effect on Thermal MEMS gyroscope performance of varying different design parameters, it was necessary to develop a mathematical model of our system. This model could give us a better understanding of the device characteristics. With the knowledge obtained from this mathematical model it would be possible to optimize the gyroscope performance. There are complicated partial differential equations governing the Thermal gyroscope and it is very hard and time-consuming, or sometimes impossible, to find an analytical solution for them. For this reason we used the finite element method (FEM) to analyze our system. It is possible to find approximate solutions to partial differential equations (PDE) with FEM technique [24]. Device optimization could be achieved by modification of the device geometry, device size, switching frequency, power supplied to the heaters, placement of the heaters and sensors, and selection of the working gas. This model also allowed us to design new devices.

It might appear that the fluid flow and heat transfer occurring in this design variant could readily be modeled using one of the many existing Computational Fluid Dynamics, CFD, modules designed to simulate natural convection. However, this turns out not to be the case: most models of natural convection employ the Boussinesq [25] approximation, which represents the change in buoyancy of a heated fluid, but not its changed density. This approximation cannot serve our purposes, since we rely on the change in fluid density, coupled with the conservation of mass, to produce the fluid flow. The governing equations are as follows:

Conservation of Energy equation:

$$\alpha \frac{dT}{dt} - \frac{d^2T}{dx^2} - \frac{d^2T}{dy^2} - \frac{d^2T}{dz^2} + \alpha u \frac{dT}{dx} + \alpha v \frac{dT}{dy} + \alpha w \frac{dT}{dz} = 0 \quad (2-1)$$

This equation reflects the fact that the change in thermal energy at a point in the gas, represented by the first term on the left-hand side of the equation, is determined by the rates at which heat is conducted (second to fourth terms) and convected (fifth to seventh terms) to that point.

Conservation of Mass equation:

$$\frac{d\rho}{dt} + \frac{d\rho u}{dx} + \frac{d\rho v}{dy} + \frac{d\rho w}{dz} = 0 \quad (2-2)$$

This equation reflects the fact that the density change at any point in the gas is determined by the convective mass transport to and from that point.

Differential form of equation of state:

$$\frac{dP}{dt} - RT \frac{d\rho}{dt} - \rho R \frac{dT}{dt} = 0 \quad (2-3)$$

Equation (2-3) is obtained by taking the differential form of the equation of state ( $P = \rho RT$ ) for an ideal gas. Note that  $R$  here is the *specific* gas constant rather than the molar gas constant. This allows us to model the effect of changing the working fluid from air to a gas with a different molecular weight, such as sulfur hexafluoride. This equation links the heating of the gas to its change in density. This, together with Equation 2-2, creates the flow of hot gas on which the Coriolis force acts.

Conservation of Momentum, x direction, Coriolis force added:

$$\rho \left( \frac{du}{dt} + \frac{udu}{dx} + \frac{vdu}{dy} + \frac{wdu}{dz} \right) - \mu \frac{d^2u}{dx^2} - \mu \frac{d^2u}{dy^2} - \mu \frac{d^2u}{dz^2} + \frac{dP}{dx} = -2\rho v\omega_z + 2\rho w\omega_y - \rho_0\beta(T - T_0)acc_x \quad (2-4)$$

Conservation of Momentum, y direction, Coriolis force added:

$$\rho \left( \frac{dv}{dt} + \frac{udv}{dx} + \frac{vdv}{dy} + \frac{wdv}{dz} \right) - \mu \frac{d^2v}{dx^2} - \mu \frac{d^2v}{dy^2} - \mu \frac{d^2v}{dz^2} + \frac{dP}{dy} = -2\rho w\omega_x + 2\rho u\omega_z - \rho_0\beta(T - T_0)acc_y \quad (2-5)$$

Conservation of Momentum, z direction, Coriolis force added:

$$\rho \left( \frac{dw}{dt} + \frac{udw}{dx} + \frac{vdw}{dy} + \frac{wdw}{dz} \right) - \mu \frac{d^2w}{dx^2} - \mu \frac{d^2w}{dy^2} - \mu \frac{d^2w}{dz^2} + \frac{dP}{dz} = -2\rho w\omega_y + 2\rho u\omega_x - \rho_0\beta(T - T_0)acc_z \quad (2-6)$$

In Equations (2-1) to (2-6),  $T$  represents temperature in Kelvin,  $u$  is velocity in the  $x$  direction (m/s),  $v$  is velocity in the  $y$  direction (m/s),  $w$  is velocity in the  $z$  direction (m/s),  $\omega_x$  is rotation frequency about the  $x$  axis (1/s),  $\omega_y$  is rotation frequency about the  $y$  axis (1/s),  $\omega_z$  is rotation frequency about the  $z$  axis (1/s),  $\mu$  represents the dynamic viscosity of the fluid (Pa·s),  $\rho$  is fluid density (kg/m<sup>3</sup>),  $R$  is the specific gas constant (J/(kg·K)),  $\alpha$ , *thermal diffusivity*, is defined as

$$\alpha = \frac{k}{\rho_0 \cdot c}$$

where  $c$  is specific heat (J/(kg·K)),  $k$  is fluid thermal conductivity (W/(m·K)), and  $\beta$

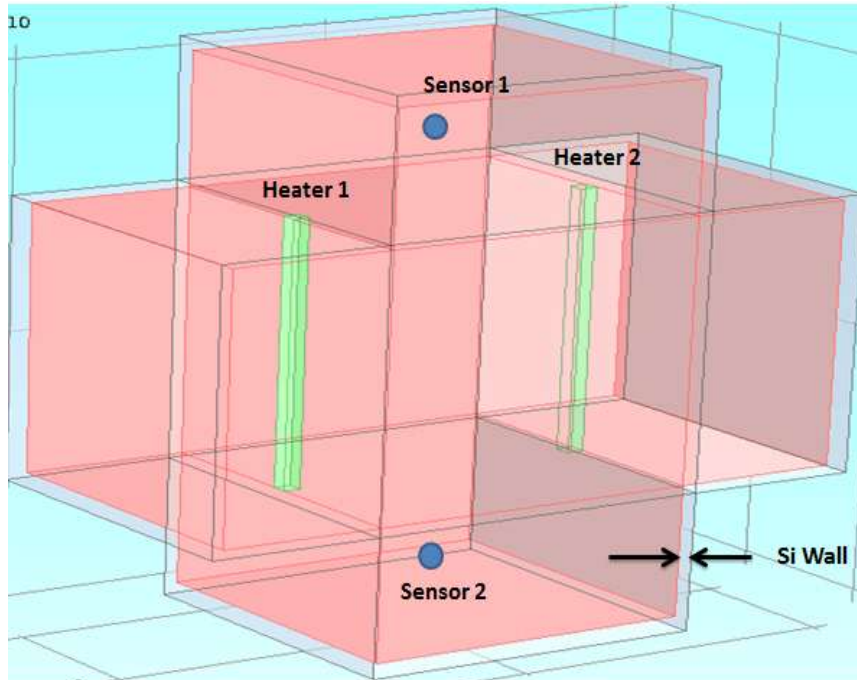
stands for the volumetric coefficient of expansion (1/K),  $a_x$  (m/s<sup>2</sup>),  $a_y$  (m/s<sup>2</sup>),  $a_z$  (m/s<sup>2</sup>) are accelerations along the  $x$ ,  $y$  and  $z$  axes respectively.

Equations (2-4), (2-5) and (2-6) are the Conservation of Momentum equations in the  $x$ ,  $y$  and  $z$  directions; the effect of the Coriolis force appears here. Depending on the orientation of the gyroscope, components of the buoyancy force may also appear in one or more of these three equations.

A numerical simulation package that could represent Coriolis force is necessary [26] to solve our partial differential equations. After investigation of different software such as MATLAB, ANSYS, and COVENTOR software, we decided to use COMSOL package, since this software allows us to specify our own PDEs and link them with other physics interfaces [27].

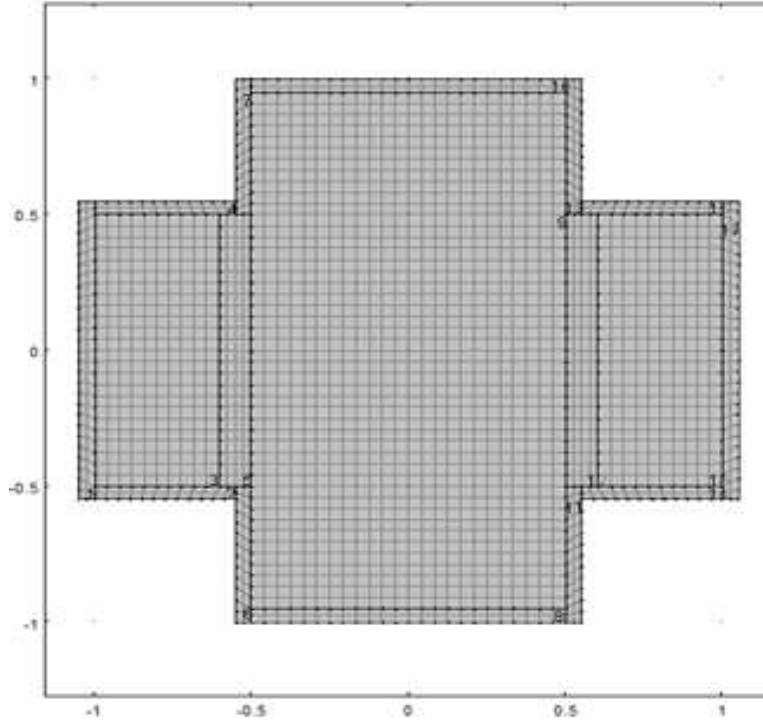
## 2.1. COMSOL Simulation

In order to analyze the performance of the gyroscope along with any design improvements, a simple MEMS gyroscope is modeled in COMSOL. The model consists of a cavity approximately one cubic millimeter in volume, with silicon resistive heaters at both ends as shown in Figure 2-1. The model geometry forms a 'plus' shape, rather than a square or rectangle, in order to minimize unnecessary heating and air flow in the otherwise open corner cavities. By switching the heaters on and off alternately, an oscillating gas flow will be created across the cavity.



**Figure 2-1 COMSOL model showing the cavity, heaters, and temperature sensors**

Our three-dimensional model took a very long time to run and solve the partial differential equations and we had to wait several days to find the solution. Computer memory failure was another limitation that we faced initially. As a result we decided to replace our three-dimensional model with a two-dimensional one. We then meshed the cavity as shown in Figure 2-2. The fluid in the cavity was represented by Equation (2-1) to (2-6) in two dimensions. In this two-dimensional model air has been chosen as a low-density gas and sulfur hexafluoride,  $\text{SF}_6$ , has been chosen as a denser gas. Our initial models simply had a fixed-temperature and zero-flow boundary condition set at the boundaries of the cavity. For increased accuracy, we have modeled the silicon walls surrounding the gas cavity, providing a more realistic description of the physical device. The properties of  $\text{SF}_6$ , air and the silicon forming the walls are shown in Table 1 and Table 2.



**Figure 2-2 Two-D COMSOL mesh representing the gyro**

**Table 1 Physical parameters of SF<sub>6</sub> and air used in the model**

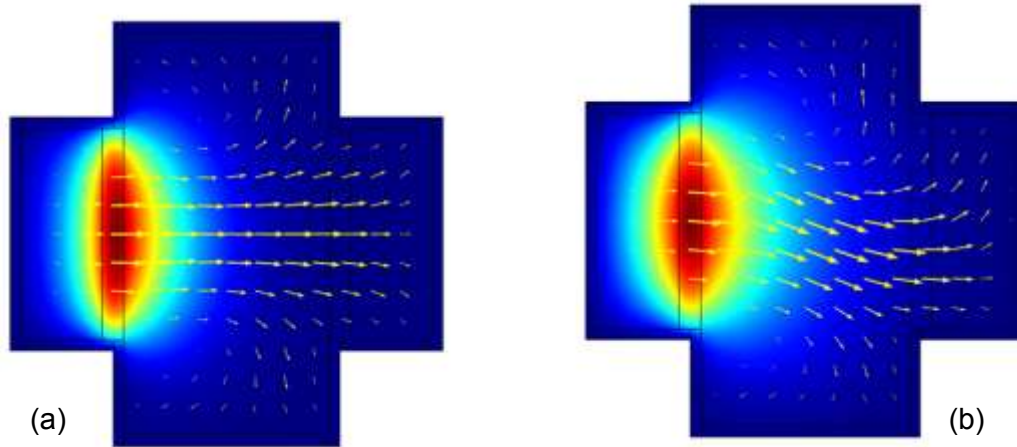
<b>Parameters</b>	<b>value (SF<sub>6</sub>)</b>	<b>value (Air)</b>	<b>Description</b>
$k$	0.012 W/(m•K)	0.0243 W/(m•K)	Gas thermal conductivity
$c$	670 J/(Kg•K)	1000 J/(Kg•K)	Gas specific heat capacity
$\mu$	14.2 $\mu$ Pa•s	10 $\mu$ Pa•s	Gas viscosity
$R$	57 J/(kg•K)	267 J/(kg•K)	Specific gas constant
$T_0$	300 K	300 K	Initial gas temperature
$P_0$	100 kPa	100 kPa	Initial gas pressure
$\rho_0$	6.23 kg/m <sup>3</sup>	1.29 kg/m <sup>3</sup>	Initial gas density at $T_0$ and $P_0$
$\alpha$	2.87 $\mu$ m <sup>2</sup> /s	18.83 $\mu$ m <sup>2</sup> /s	Thermal diffusivity
$\omega$	1 rad/s	1 rad/s	Angular rate

**Table 2 Physical parameters of Silicon used in the model**

<b>Parameters</b>	<b>value (Silicon)</b>	<b>Description</b>
$c_{Si}$	700 J/(Kg•K)	Si specific heat capacity
$k_{Si}$	147 W/(m•K)	Si thermal conductivity
$\rho_{Si}$	2,329 kg/m <sup>3</sup>	Si density
$\alpha_{Si}$	90.16 $\mu$ m <sup>2</sup> /s	Si thermal diffusivity



If the gyro is not rotating the gas flow follows a straight path, Figure 2-3(a). On the other hand, if the gyroscope is rotating, Coriolis forces will divert this oscillating flow to one side, then the other, Figure 2-3(b). We place temperature sensors in the path of the diverted flow, measure the resulting temperature difference, and deduce the speed and orientation of rotation.



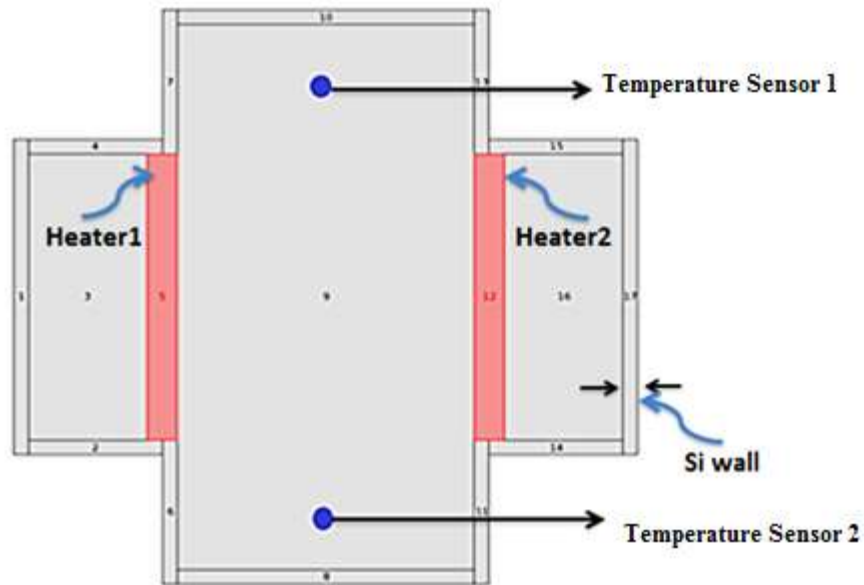
**Figure 2-3 Modelling air flow (a) with no rotation or gas bubble deviation, and (b) with rotation and gas bubble deviation**

The heaters are supplied with a square wave of input power, consuming 0.15 W at a 12 Hz frequency. By monitoring the temperature difference between the two temperature sensors (Coriolis-induced temperature difference between two temperature sensors when the device is rotating), we obtain the parameter responsible for determining the sensitivity of the gyroscope.

$$Sensitivity = \frac{\delta(Output\ Signal)}{\delta(Input\ Signal)} = \frac{\delta(\Delta T)}{\delta\omega} \quad (2-7)$$

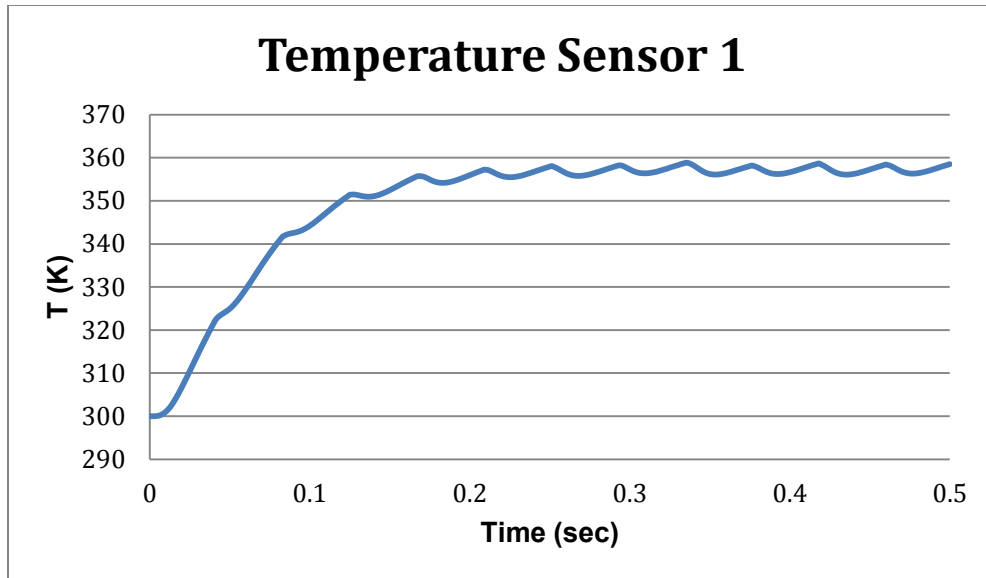
Device sensitivity indicates how much the sensor's output changes when the measured quantity changes. As shown in Equation (2-7), sensitivity is equal to the output signal variation divided by the input signal variation, where  $\delta$  represents a small variation in a specific quantity. If the relation between output and input signal is a straight line passing through the origin, it is possible to define  $Sensitivity = \frac{\Delta T}{\omega}$ . Our design goal is to increase the output signal,  $\Delta T$ , for a given  $\omega$ , thus increasing our device sensitivity.

In order to monitor  $\Delta T$  we have recorded the temperature at the bottom and top of the cavity as shown in Figure 2-4. These points correspond to the location of resistive silicon temperature sensors in the physical device; in the computational model, however, we do not represent the silicon sensors, we merely record the temperature at the corresponding points in the gas. We monitor the temperature difference between these two points and correlate it with the angular rate, as shown in Figure 2-5.



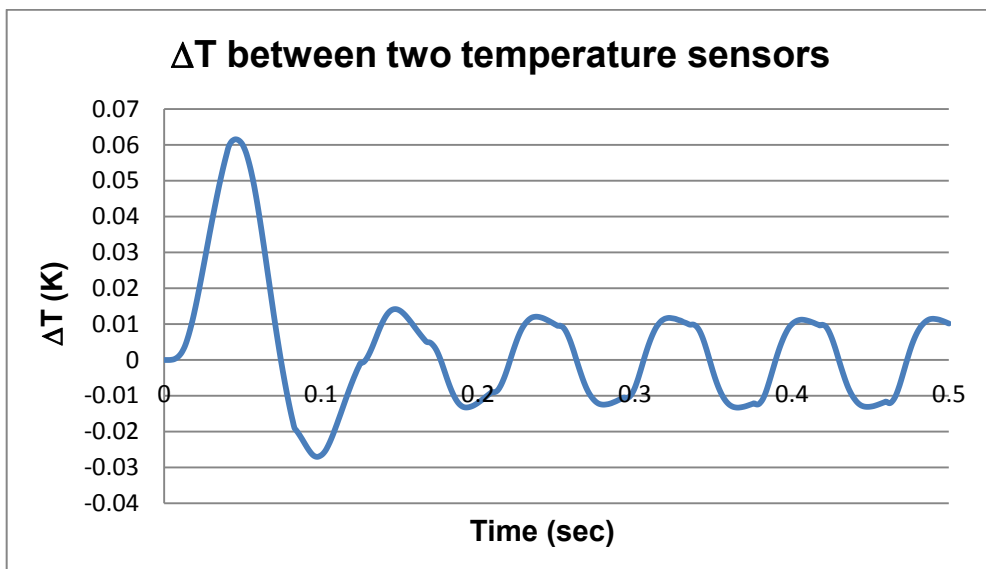
**Figure 2-4 Device structure showing places of temperature sensors**

Figure 2-5 shows the temperature variation of the top temperature sensor over the first 500 ms of operation. There is an initial transient of about 200 ms as the device warms up, after which it reaches a cyclic steady state.



**Figure 2-5 Temperature variation of top sensor**

We then calculated the temperature difference between the locations of the top and bottom temperature sensors, as shown in Figure 2-6.



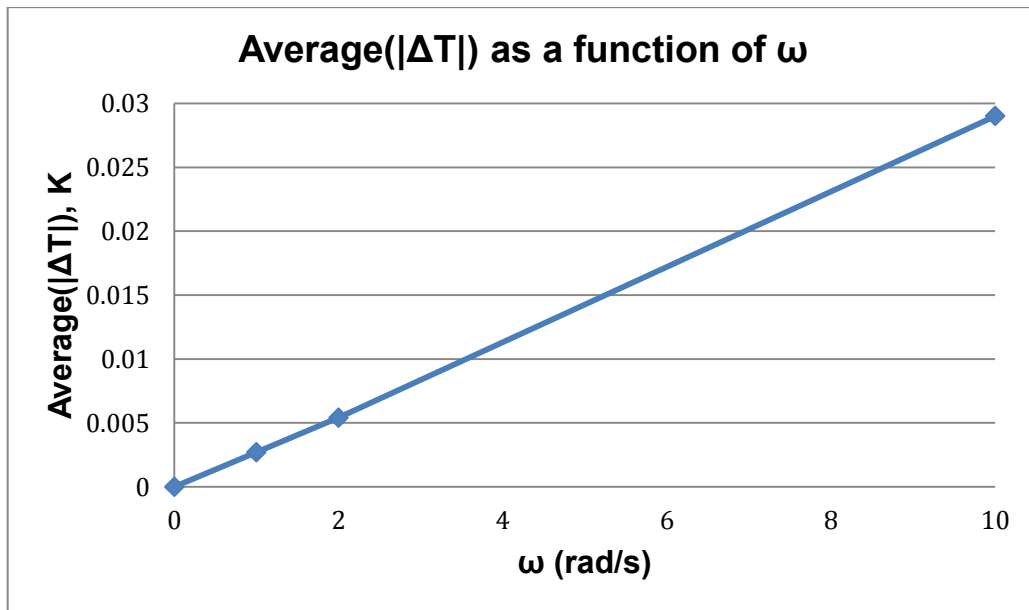
**Figure 2-6 Temperature difference monitored between the two temperature sensors**

Figure 2-6 shows a periodic signal with a large transient peak. Although we applied square-wave signals to the heaters to turn them on and off, the gas around the heaters takes some time

to warm up and to move, creating an almost sine-shaped periodic temperature fluctuation. We speculate that the large peak at the beginning of the cycle is due to rapid thermal expansion when the temperature of the system is still close to ambient. After a few cycles these transient effects die away and we have a cyclic steady state.

## 2.2. Angular Rate, $\omega$ , and Gyroscope Sensitivity

In this section the relation between angular rate,  $\omega$ , and gyroscope sensitivity will be discussed. Figure 2-7 shows the simulation results of varying  $\omega$ , for  $\omega = 1$  rad/s,  $\omega = 2$  rad/s and  $\omega = 10$  rad/s. We monitored the temperature difference between temperature sensors and calculated its average absolute value over the period of simulation, of about 0.5 second. The temperature difference during the initial transient time is excluded to eliminate the impact of the large peak at the beginning of each cycle. These results are plotted in Figure 2-7. According to this figure the relation between angular rate and output signal for small values of  $\omega$  is linear; however this might saturate and level off if the angular rate exceeds a certain value.



**Figure 2-7**  $|\Delta T|$  monitoring for different values of  $\omega$ , cavity filled with air

We can conclude that  $\Delta T$  is directly proportional to angular rate,  $\omega$ , over the range modelled. On theoretical grounds we can predict that the temperature differential cannot increase linearly for unlimited values of  $\omega$ ; it can never exceed the temperature difference between heater and ambient, for example.

## 3. Design and Analysis of Micromachined Thermal Gyroscope

### 3.1. Overview

In this chapter we will investigate the effect of fluid properties, operating pressure, heater power and heater switching frequency on the gyroscope performance.

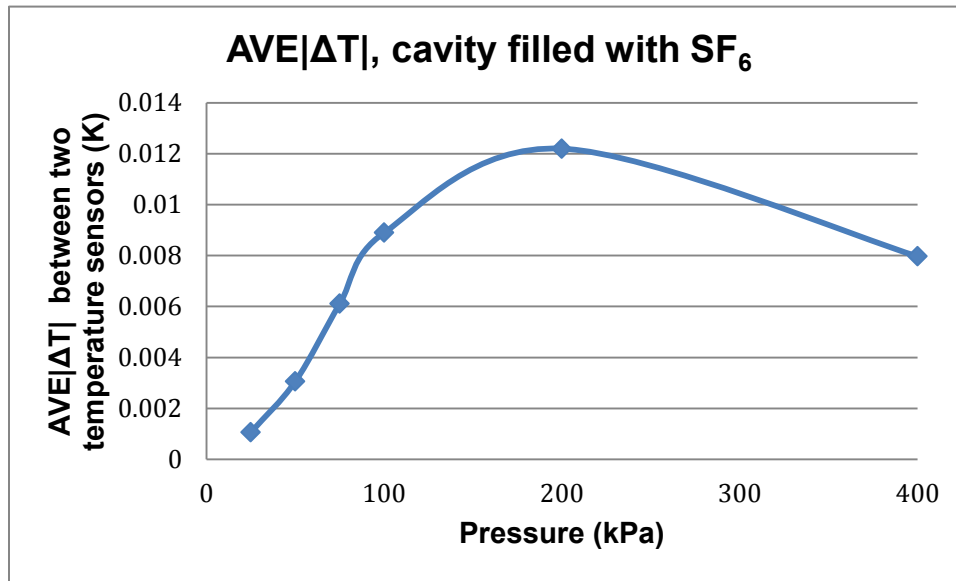
### 3.2. Impact of Pressure on Sensitivity

In this part of our work, we have considered air and SF<sub>6</sub> as the gases filling the cavity and we have considered a range of pressures. Varying  $P_0$  in the numerator of Equation (3-1) corresponds to filling the cavity at a certain gas pressure, while varying  $R$  corresponds to filling the cavity with gas of a particular molecular weight. These two factors jointly determine the density of the gas filling the cavity. We represent the gyroscope as rotating with an angular rate of  $\omega = 1$  rad/s.

$$\rho = \frac{P_0}{RT_0} \quad (3-1)$$

We monitored the temperature difference between two symmetrically placed temperature sensors. In the initial study we chose SF<sub>6</sub> as the working gas and considered different values of pressure ( $P = 25$  kPa,  $P = 50$  kPa,  $P = 75$  kPa,  $P = 100$  kPa,  $P = 200$  kPa,  $P = 400$  kPa). The resulting differential temperatures have been plotted in the Appendix, Figure 1-A, (a-e).

According to these simulation results, we conclude that sensitivity is directly proportional to pressure up to a certain limiting value. For ease of comparison the average value of  $|\Delta T|$  in each case over a period of 0.5 sec, omitting the initial transient, has been calculated. This result is shown in Figure 3-1.

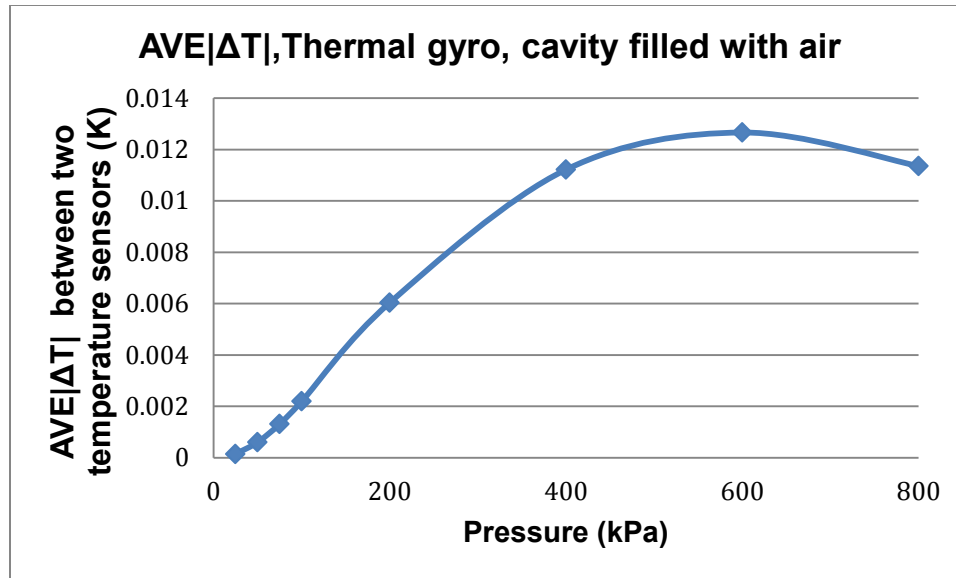


**Figure 3-1 Average  $|\Delta T|$  versus Pressure, cavity filled with  $SF_6$**

Figure 3-1 shows that by increasing pressure, sensitivity will increase almost linearly, up to 200 kPa, and then it will saturate and even after a while go down.

We repeated this series of studies using air, which has lower molecular weight. In this study different values of pressure ( $P = 25$  kPa,  $P = 50$  kPa,  $P = 75$  kPa,  $P = 100$  kPa,  $P = 200$  kPa,  $P = 400$  kPa,  $P = 600$  kPa,  $P = 800$  kPa) were considered, and a summary of these results is shown in the Appendix, Figure 2-A, (a-h).

The average value of  $|\Delta T|$  in each case over a period of 0.5 sec has been calculated, and this result is shown in Figure 3-2.



**Figure 3-2 Average  $|\Delta T|$  versus Pressure, cavity filled with air**

Figure 3-2 again shows that by increasing pressure sensitivity will increase almost linearly, up to 400kPa, and then it will saturate and even after a while will go down.

Figure 3-2 (for low-molecular-weight gas, air) and Figure 3-1 (for higher-molecular-weight gas, SF<sub>6</sub>) together suggest that sensitivity improves linearly up to a certain critical value of *density* (rather than a certain critical value of *pressure*), after which it levels off.

To sum up, there is a linear relation between density of the gas and sensitivity up to a certain limiting value, beyond which the sensitivity declines.

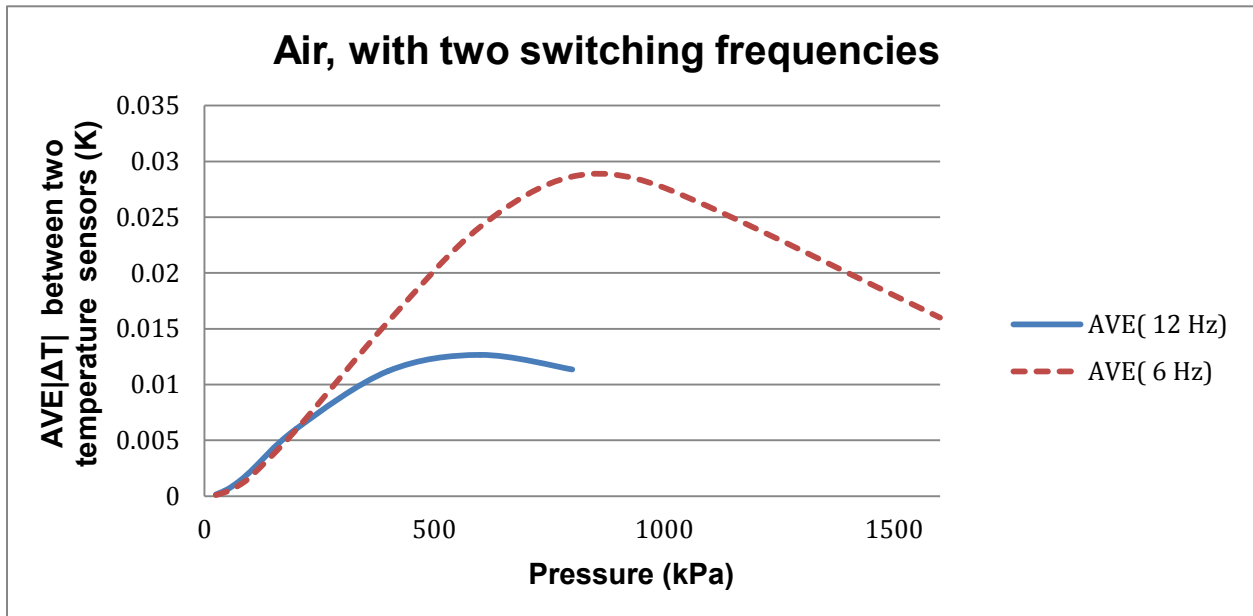
### 3.3. Heater Switching Frequency and Gyroscope Sensitivity

Why does the increase in sensitivity of the gyro with density level off at a certain critical value of density? We speculate that where the density of a particular gas is very high with a given switching frequency, the gas does not have time to warm up before the heaters switch, and as a result sensitivity will be reduced. The practical solution for this problem could be to increase the



time for which each heater is on, by decreasing the switching frequency of the heaters. In order to investigate this, the following simulation has been done.

The angular rate is again  $\omega = 1$  rad/s, the cavity is again filled with air and heater switching frequency is reduced to 6 Hz, half that of the previous simulation. The average values of  $|\Delta T|$  in each case over a period of 0.5 sec are plotted in Figure 3-3.



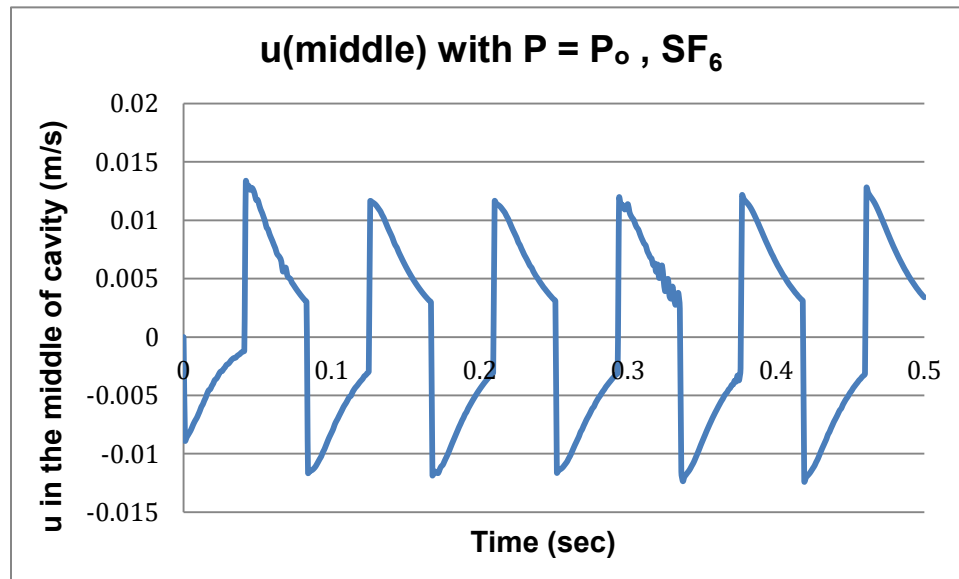
**Figure 3-3 Comparing average of  $|\Delta T|$  in two cases, switching frequency equal to 12 Hz, blue curve, and switching frequency equal to 6 Hz, red dashed curve, cavity filled with air**

From Figure 3-3 we see that by reducing the frequency of switching the heaters – that is, increasing the time for which each heater is on – we give the gas more time to warm up between switchings, and as a result the sensitivity continues to increase with increasing density, up to an increased critical value.

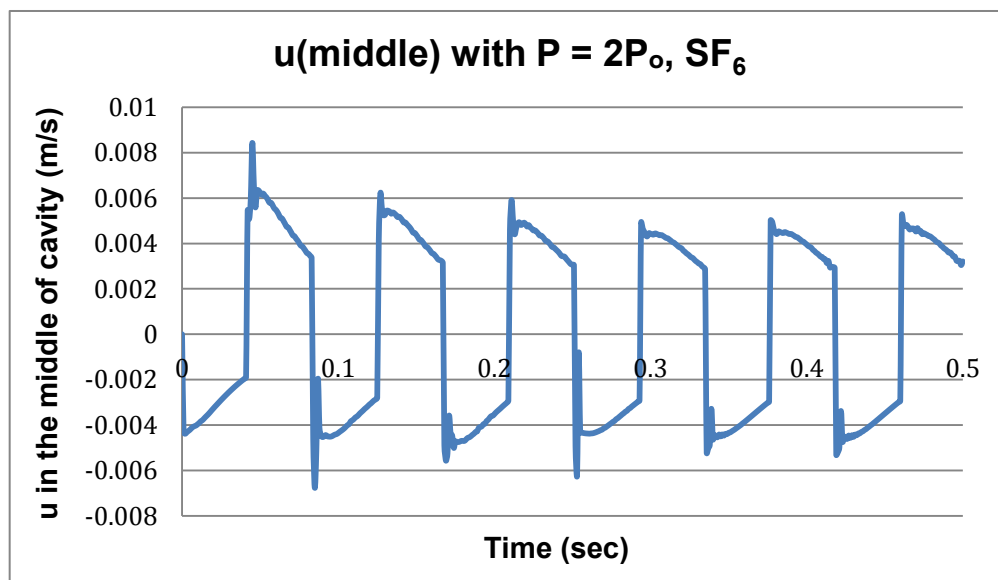
### 3.4. Gas Velocity, $u$ , Monitoring by Varying Density

The COMSOL model allows us to calculate the velocity  $u$  of the expanding gas stream. This gives us further insight into why the gyro sensitivity falls off when gas density increases beyond a certain value.

Changing the density of the gas might also change gas velocity. The model allows us to calculate the value of  $u$  in all the cases we have studied so far. Gas velocities in the middle of the cavity for  $P = 100 \text{ kPa}$  and  $P = 200 \text{ kPa}$  are shown in Figure 3-4 (a) and Figure 3-4 (b).



**Figure 3-4 (a) Monitoring  $u$  in the middle of cavity,  $P = 100 \text{ kPa}$**

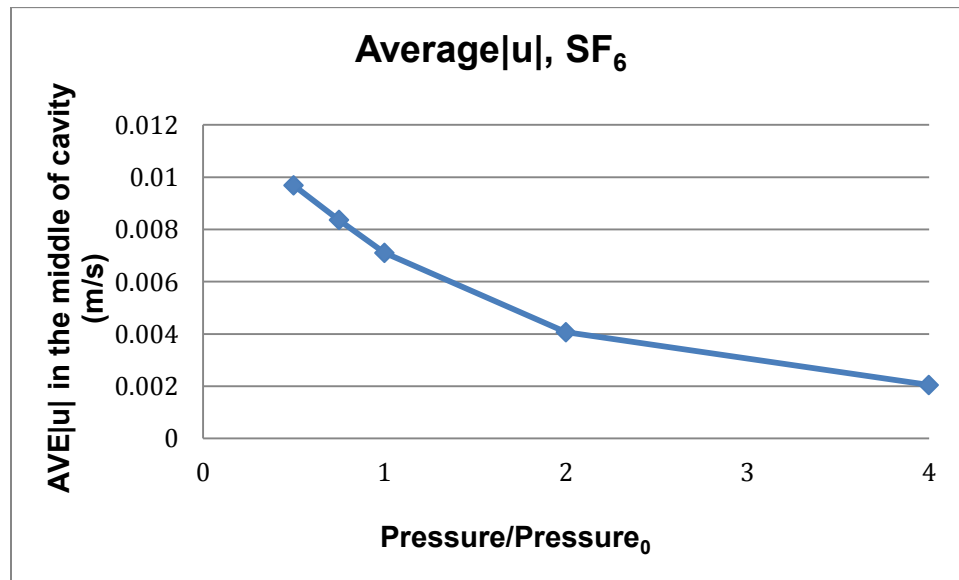


**Figure 3.4 (b) Monitoring  $u$  in the middle of cavity,  $P = 200 \text{ kPa}$**

Gas velocities for other values of pressure,  $P = P_0/4$ ,  $P = P_0/2$ ,  $P = P_0/1.33$ ,  $P = 4P_0$ , have been studied and the results are presented in Figure 3-A of the Appendix. It is observable that the peak value of  $u$  does not remain constant. Instead it decreases as the pressure increases. We speculate that this is because, as the gas gets denser, it warms up more slowly and so it expands more slowly and as a result gas velocity will decrease.

This result also suggests a new strategy for increasing sensitivity. Instead of increasing gas density, we could increase the switching frequency for a low-density gas, until the heaters are on just long enough for the gas to reach thermal equilibrium, as we show in previous section. This would increase  $u$  and hence increase sensitivity.

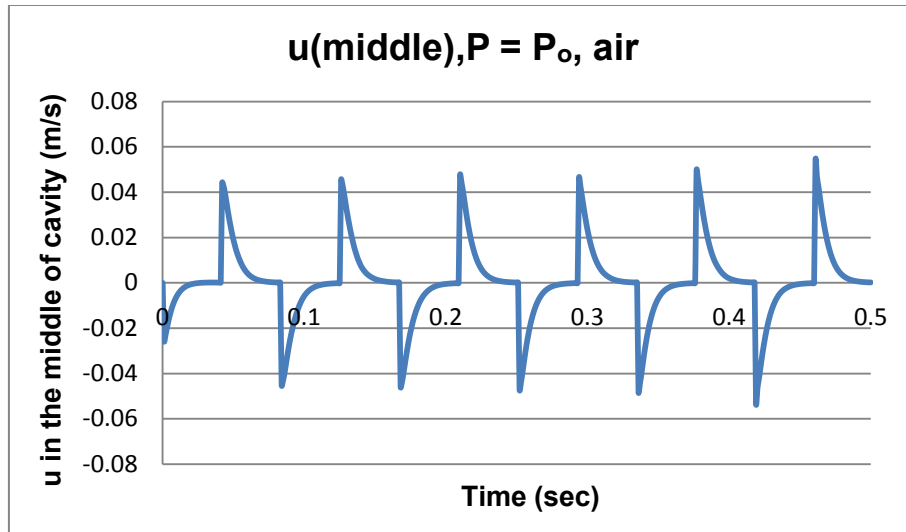
But now suppose instead of looking at the *peak* value of  $u$ , we look at *average* value of  $|u|$ . Plotting the average absolute value of  $u$  for duration of 0.5 sec gives us Figure 3-5.



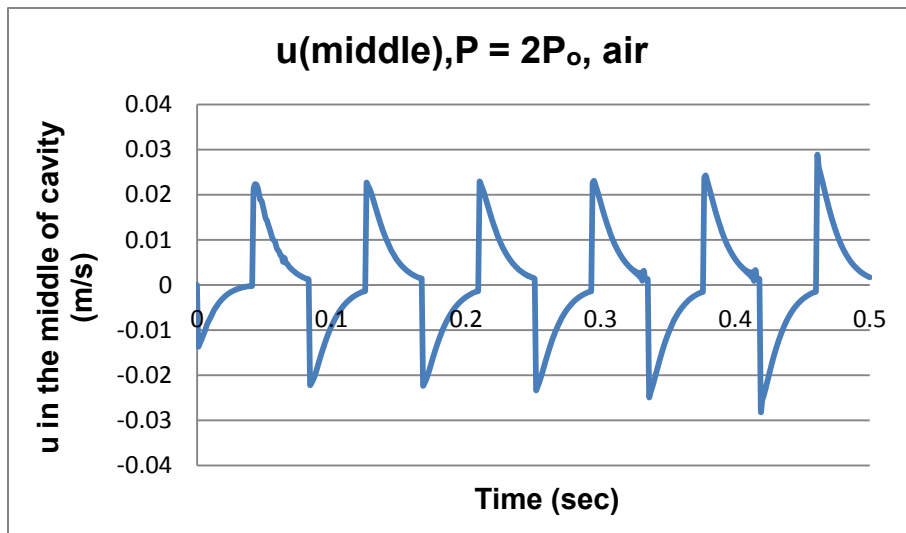
**Figure 3-5 Average  $|u|$  versus Pressure, cavity filled with  $SF_6$**

Figure 3-5 shows a decrease in average value of absolute velocity as pressure, and hence density, is increased. We will discuss this effect in this chapter with more details.

We also simulated the situation where the cavity is filled with air. Results for both cases  $P = P_0$ , and  $P = 2P_0$  are shown in Figure 3-6 (a) and Figure 3-6 (b).



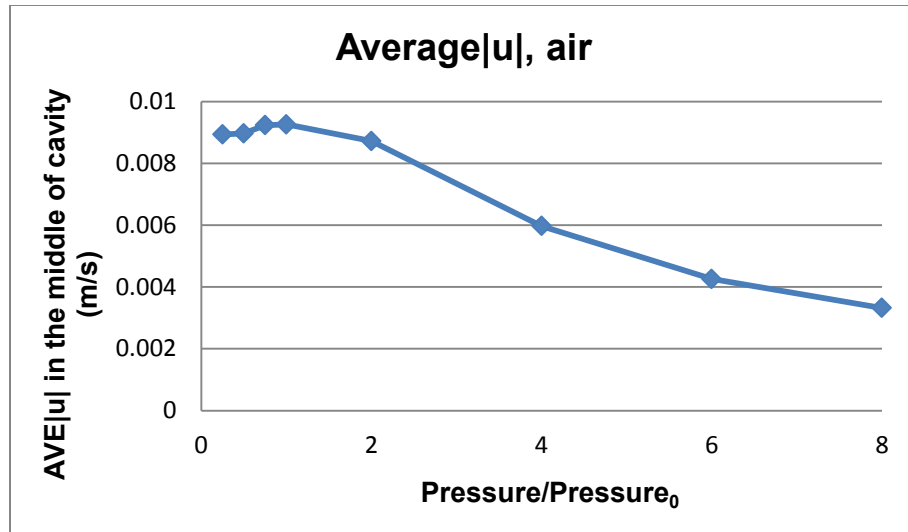
**Figure 3-6 (a)  $u$  in the middle of cavity,  $P = 100$  kPa**



**Figure 3-6 (b)  $u$  in the middle of cavity,  $P = 200$  kPa**

We have also studied other values of pressure,  $P = P_o/4$ ,  $P = P_o/2$ ,  $P = P_o/1.33$ ,  $P = 4P_o$ ,  $P = 6P_o$ ,  $P = 8P_o$ , these results are plotted and shown in Figure 4-A of the Appendix.

Again suppose instead of looking at the *peak* value of  $u$ , we look at the *average* value of  $|u|$ . Finding the average of absolute value of  $u$  for duration of 0.5 sec, and plotting it gives us Figure 3-7.



**Figure 3-7 Average |u| versus Pressure, cavity filled with air**

We see that the average value of absolute gas velocity falls off once we pass a certain critical value of pressure for both cases where cavity is filled with SF<sub>6</sub> and with air, Figure 3-5 and Figure 3-7 respectively, and that the critical value of pressure is higher for the lower-molecular-weight gas. This confirms that the factor responsible for the falling-off is gas density. So we have an explanation for the falling-off in sensitivity at higher densities: beyond a certain value of density, the factor  $u$  in the Coriolis term of Equation (2-5) falls off, so that the product of  $u$  and  $\rho$  remains constant.

But why does gas velocity fall off as density exceeds a critical value, and what determines this critical value? We speculate that the limiting value occurs at the point where it takes the gas longer to reach its equilibrium temperature than the period for which each heater is on. We confirmed this speculation in the previous section, where we reduced the switching frequency of the heaters, so that each heater remained on for a longer time (Figure 3-3).

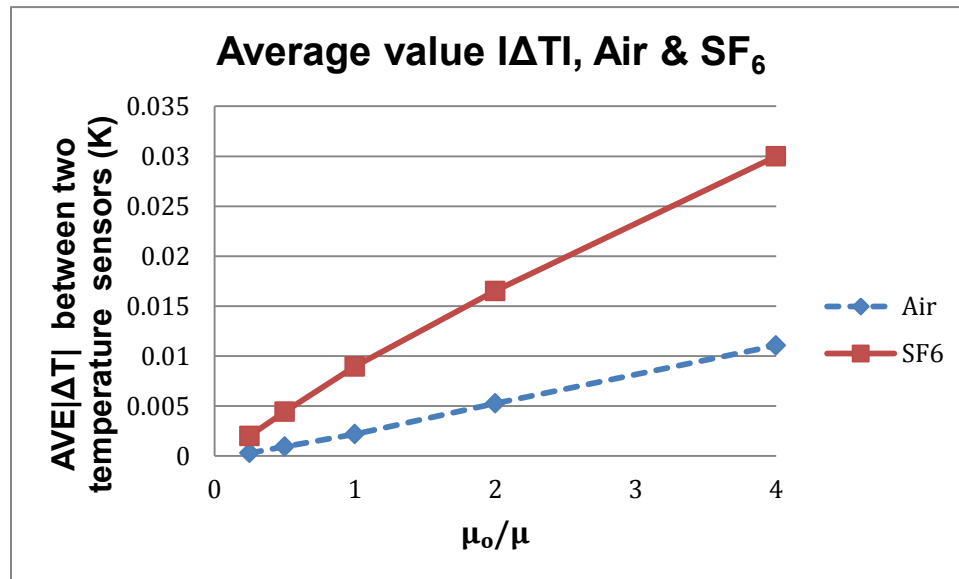
### 3.5. Viscosity Analysis

In this section we study the impact of gas viscosity on the gyroscope sensitivity. Viscosity is a resistive force which describes a fluid's internal resistance to flow. The more viscous a fluid is, the harder it will be to create a flow. Hence we would expect that increasing the gas viscosity

will result in decreasing the gas velocity,  $u$ , and hence, according to Equation 2-5, reducing the Coriolis force, and as a consequence sensitivity will decrease.

In the first set of simulations we have considered  $SF_6$  as the gas filling the cavity in the baseline case, and have then compared this baseline case with hypothetical working fluids having viscosities from four times lower than that of  $SF_6$  to four times higher. We repeated our simulations using air instead of  $SF_6$ . In all cases the angular rate,  $\omega$ , is 1 rad/s. The results of this study are shown in Figure 5-A and Figure 6-A of the Appendix for  $SF_6$  and air respectively.

Average values of absolute temperature difference over the period of 0.5 sec for both gases,  $SF_6$  and air, for the range of  $\mu_o/\mu$  have been plotted in Figure 3-8.



**Figure 3-8 Average  $|\Delta T|$  versus viscosity (air &  $SF_6$ )**

According to Figure 3-8, we can conclude that by decreasing viscosity,  $\mu_o/\mu$  will increase, and as a result sensitivity will increase.

### 3.6. Ekman Number and Gyro Sensitivity

We can sum up the results obtained so far in this chapter in terms of a single non-dimensional number, the Ekman number, The Ekman number is defined as:

$$Ekman\ Number = \frac{Viscosity\ Force}{Coriolis\ Force} = \frac{F_v}{F_c} \quad (3-1)$$

The Coriolis force shown in the denominator is given by the equation

$$F_c = -2m\omega u \quad (3-2)$$

where  $m$  stands for mass of the fluid,  $\omega$  represents angular rate,  $u$  is the velocity of the fluid. Equation (3-2) can also be presented as:

$$\frac{F_c}{V} = -2\rho\omega u \quad (3-3)$$

where  $\rho$  stands for density.

The viscosity force shown in the nominator of Equation (3-1) given by the following equation:

$$F_v \propto \mu \cdot u \quad (3-4)$$

where  $\mu$  stands for dynamic viscosity and  $u$  represents fluid flow velocity.

Our hypothesis is that the relation between sensitivity and Ekman number is given by:

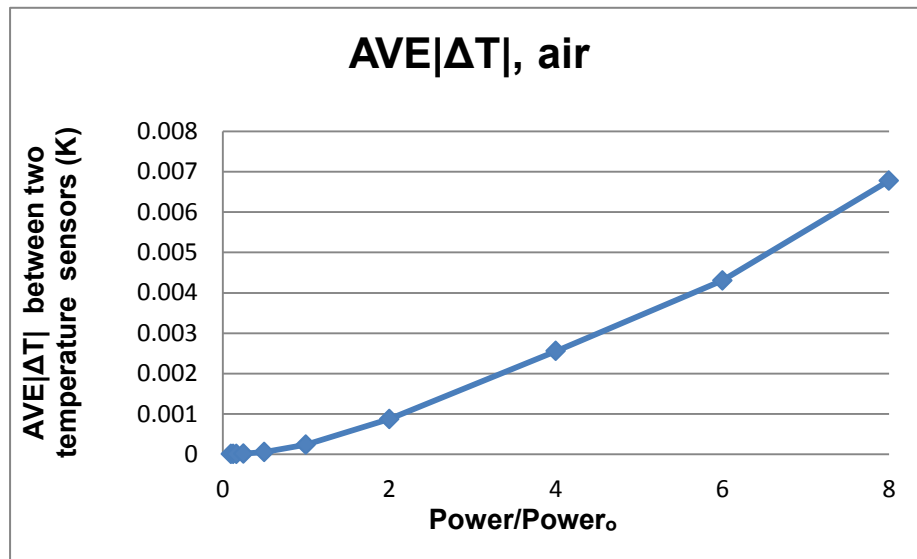
$$Sensitivity \propto \frac{1}{Ekman\ Number} \quad (3-5)$$

Equation (3-5) shows that sensitivity is inversely proportional to Ekman number. This implies that the device sensitivity will increase in direct proportion to gas density, as implied by Equation (3-1), (3-3) and Equation (3-5), and in inverse proportion to gas viscosity, as implied by Equation (3-1), (3-4) and Equation (3-5). However, when the gas density increases to the point where the heaters cannot bring the gas to equilibrium temperature within the switching time, the factor  $u$  in Equation (3-3) will drop in value and the sensitivity will no longer increase.

### 3.7. Changing Heater Power and Gas Velocity Monitoring

As previously discussed, another factor which can change gas velocity ( $u$ ) is the heater power. In the next set of simulations, all parameters are kept constant except heater power. The mean absolute temperature differences between the two temperature sensors and the gas velocity  $u$  have been studied and the results of this work are shown in Figure 6-A of the Appendix.

The average value of  $|\Delta T|$  in each case over a period of 0.5 sec has been calculated for air at atmospheric pressure. This result is shown in Figure 3-9. Power has been varied from one-eighth of its baseline value to eight times its baseline value. The results at the upper end of the power range are not entirely realistic, since they correspond to heater temperatures at which radiative heat transfer, which is not represented in our model, would be significant. At the extreme end of the range, the heater would melt. However, within the range of applicability of the model, Figure 3-9 shows that sensitivity increases superlinearly with heater power.



**Figure 3-9 Average  $|\Delta T|$  versus Power (air)**

The average temperature value of one heater has been plotted in Figure 3-10 and it shows a linear relation between power and average heater temperature,  $TH_1$ . In our simulation, high



power has been applied to the gyroscope heaters to scale up the output signal and facilitate comparison between different output signals. However, as noted above, in reality it is not possible to heat up the device to the highest values.

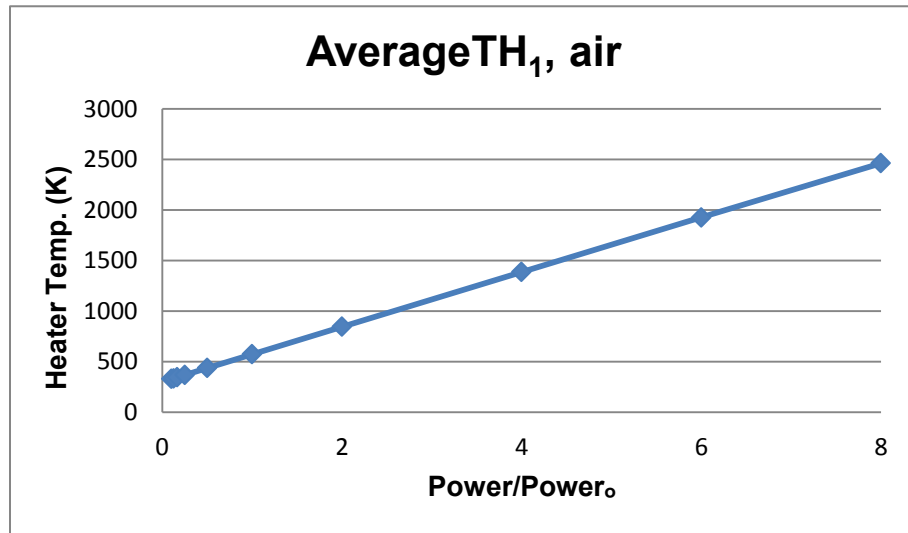


Figure 3-10 Average  $TH_1$  versus Power (air)

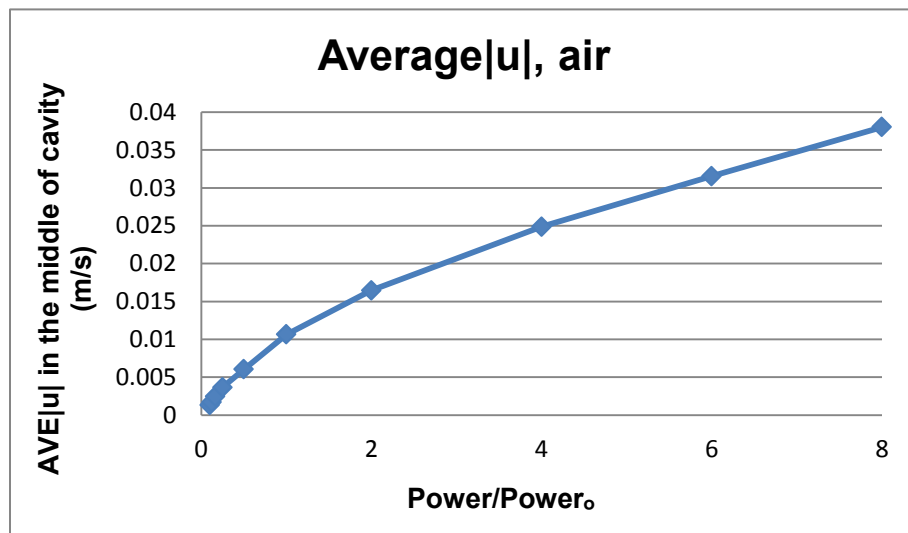
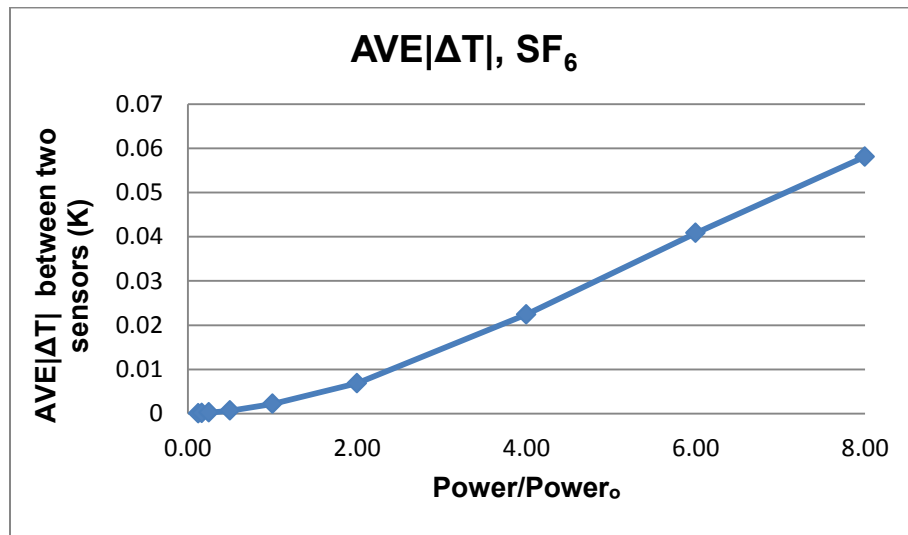


Figure 3-11 Average  $|u|$  versus Power, (air)

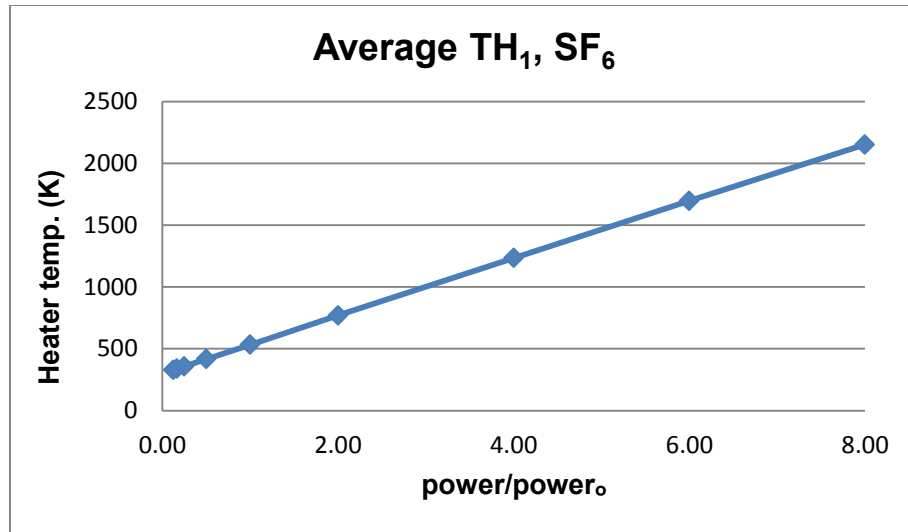
By increasing heater power, the average value of temperature of the heater will increase linearly,  $Q = h(T_H - T_E)$  where  $Q$  is the rate of convection heat transfer,  $h$  is the convective heat transfer coefficient,  $T_H$  represents heater temperature and  $T_E$  stands for ambient temperature. If the velocity of the gas were constant, this increase in heater power would result in linear increase in sensitivity, since the sensors would be immersed in a constant flow of increasingly hot gas. But the velocity of the gas will *also* increase almost linearly, Figure 3-11, resulting in an *additional* increase in the sensitivity. As a consequence, sensitivity will increase quadratically with power.

We repeat the simulations by changing the working gas from air to  $SF_6$ . The results, shown in Figure 7-A of the Appendix, confirm the results obtained with air. The average value of  $|\Delta T|$  in each case over period of 0.5 sec has been plotted in Figure 3-12.

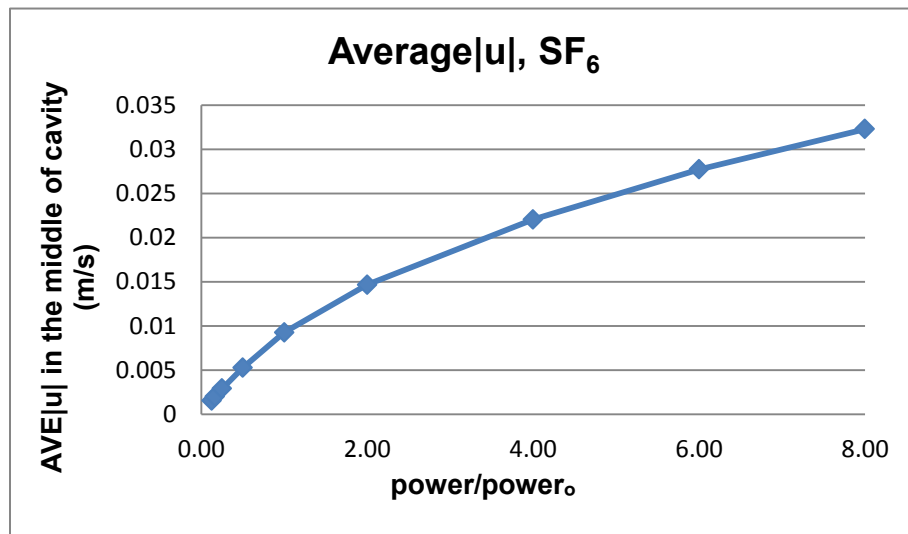


**Figure 3-12 Average  $|\Delta T|$  versus Power,  $SF_6$**

Also, the average temperature of one heater has been plotted in Figure 3-13 and it shows a linear relation between power and average heater temperature,  $TH_1$ .

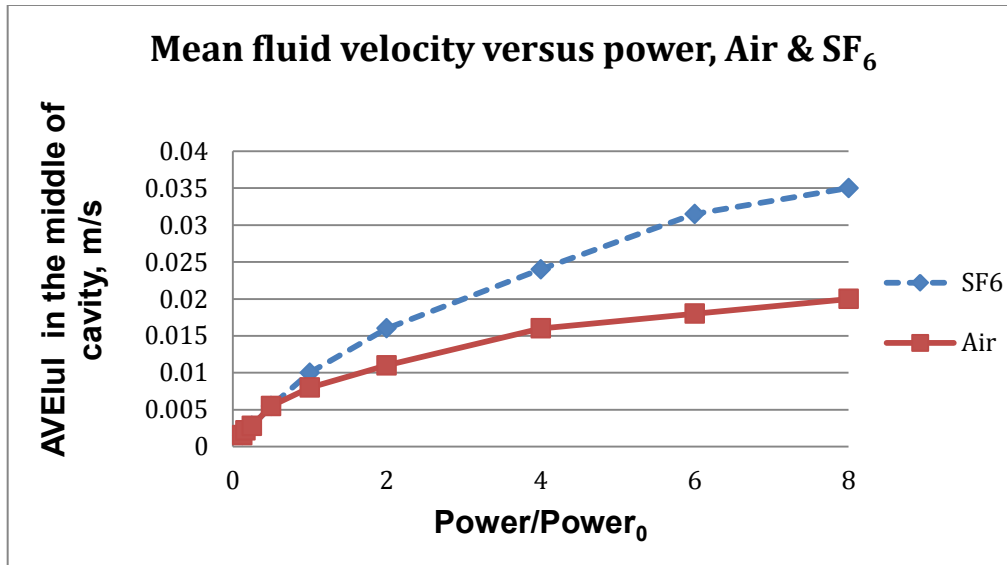


**Figure 3-13 Average  $TH_1$  versus power,  $SF_6$**



**Figure 3-14 Average  $|u|$  versus power,  $SF_6$**

The same results have been observed after changing the gas filling the cavity from air to  $SF_6$ . We have plotted the average value of  $|u|$  versus power for  $SF_6$  and air in Figure 3-15 for comparison.



**Figure 3-15 Average  $lul$  versus power, dashed and solid curves represent  $SF_6$  and air respectively**

We can conclude that by increasing power, the temperature of the heaters will increase. According to Figure 3-10 and Figure 3-13, the relation between heater power and heater temperature is linear for air and  $SF_6$ . This would result in a linear increase in sensitivity if velocity of the gas were constant. But the velocity of the gas will also increase almost linearly, Figure 3-11 and Figure 3-14, and result in a further increase in sensitivity. As a consequence, sensitivity will increase quadratically with power, Figure 3-9 and Figure 3-12. In reality, however, the experimental results might not increase as fast as predicted by simulation. This could be due either to increased conductivity of the working gas at higher temperatures, or to increased radiative heat losses, neither of these factors being represented in the simulation.

### **3.8. Signal-to-Interference Ratio (SIR) Discussion of Thermal MEMS Gyroscope**

Signal-to-interference ratio (SIR) shows how easily the output signal can be extracted from background interference.

We note that the Thermal gyroscope is very similar in design to the Hot-Air accelerometer [21]. But the gyroscope is intended to measure rotation, not acceleration. So any response that the

gyroscope makes to acceleration must be considered as an interference signal interfering with the measurement of rotation. We know from earlier work [21] that the signal resulting from acceleration depends on the Grashof number. This, combined with the results obtained earlier in this chapter, allows us to define a number that can be used to estimate the signal-to-interference ratio resulting from this interference.

Grashof number can be formulated as:

$$Gr = \frac{g\beta\Delta TL^3\rho^2}{\mu^2} \quad (3-6)$$

where  $g$  stands for acceleration due to gravity,  $\beta$  stands for volumetric thermal expansion coefficient,  $L$  is length,  $\rho$  represents density, and  $\mu$  is the dynamic viscosity.

More generally, it is possible to define the Grashof number as

$$Gr = \frac{\text{Buoyancy Force}}{\text{Viscous Force}} \quad (3-7)$$

According to Equation (3-1) the Ekman number is defined as

$$\text{Ekman Number} = \frac{\text{Viscous Force}}{\text{Coriolis Force}}$$

By multiplying Equation (3-1) and (3-7) we will create a new non-dimensional number:

$$\text{Gyointerference Number} = \text{Ekman Number} \cdot Gr = \frac{\text{Buoyancy Force}}{\text{Coriolis Force}} \quad (3-8)$$

Coriolis force per unit volume is given by the following equation:

$$F_c = -2\rho\omega u \quad (3-9)$$

Buoyancy force is given by the following equation:

$$F_b = -g\rho\Delta V \quad (3-10)$$

where  $\rho$  is the fluid density,  $g$  is the acceleration or gravity field, and  $\Delta V$  is the displaced fluid volume. By substitution of the equation of state ( $P = \rho RT$ ) in buoyancy force, we can define buoyancy force per unit volume:

$$F_b = -g\rho\beta(T_H - T_0) \quad (3-11)$$

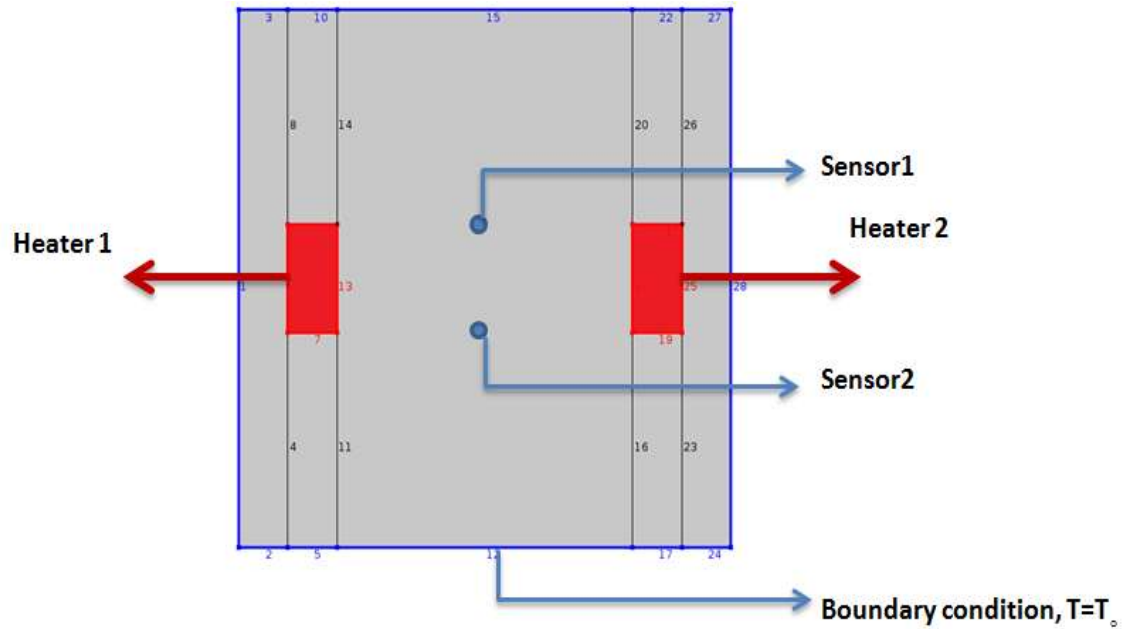
where  $\beta$  is bulk coefficient of expansion.

We can rewrite the gyrointerference number, Equation (3-8), as following:

$$GI = \frac{g\beta(T_H - T_0)}{2\omega u} \quad (3-12)$$

For a given geometry with lower value of gyrointerference number we expect to observe higher SIR. Unfortunately, the expression we have derived for GN does not contain many parameters that could be optimized to improve SIR. The factor  $\rho$  has cancelled out, and the parameters  $g$  and  $\omega$  are not under our control. To add to the difficulty, in the original design of the thermal gyroscope, the velocity  $u$  of the expanding gas stream is proportional to the product of  $\beta$  and the factor  $(T_H - T_0)$ , so these factors would also cancel out. We will assess how serious the problem of interference is, then, in the following chapter, consider one strategy for improving SIR.

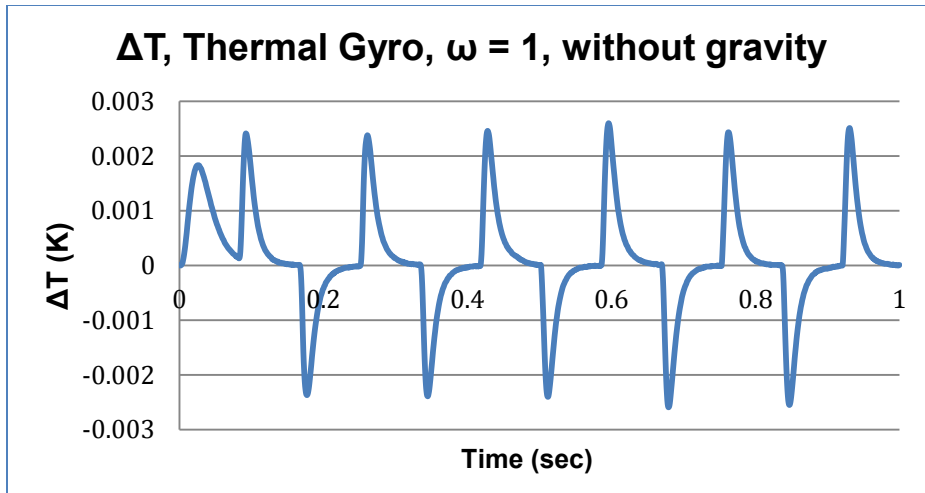
Figure 3-16 shows a rectangular model of the thermal MEMS gyroscope, where, as explained previously, the cavity is filled with gas. The heaters, coloured in red, are on the left and right sides of the cavity, and two temperature sensors are located on top and bottom.



**Figure 3-16 COMSOL Model, places of temperature sensors and heaters are shown**

In this model the heaters are alternately turning on and off. Heater switching frequency is 6 Hz, and 0.3 watts of power are allocated to each heater.

Simulations were carried out for the case with no acceleration signal, i.e.  $a_x = a_y = 0$  in Equation (2-4) and Equation (2-5), and the gyroscope is rotating with  $\omega = 1$  rad/sec. The temperature difference between the two sensors is observed and shown in Figure 3-17.



**Figure 3-17 Temperature difference is monitored while the impact of gravity is eliminated, Thermal Gyroscope**

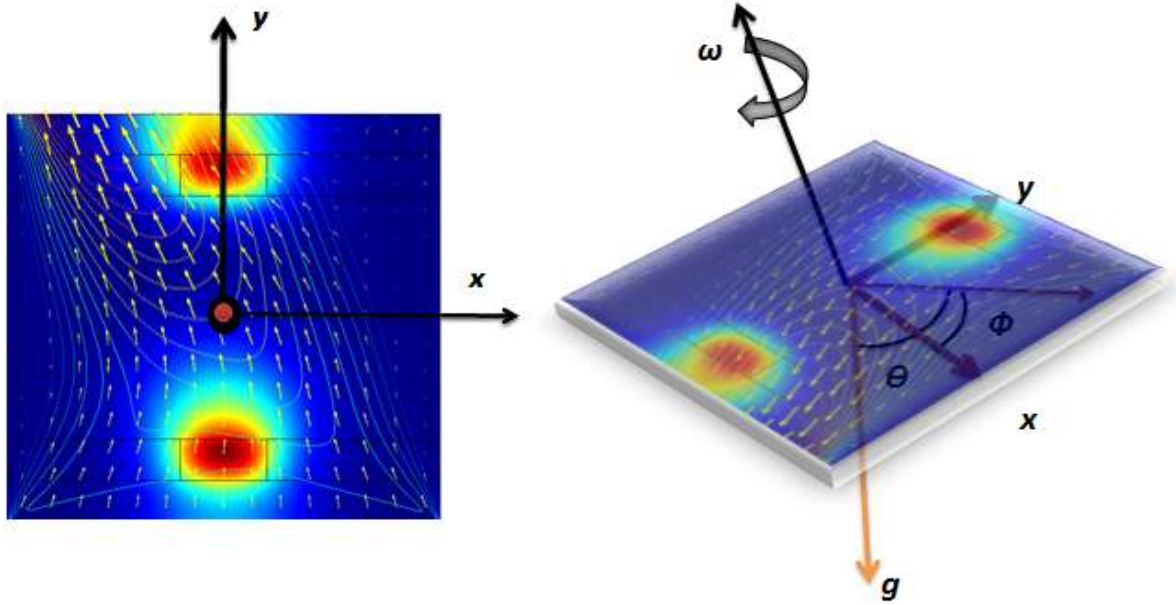
In the next step of the work we considered the impact of acceleration due to gravity. We implemented acceleration terms in the following equations:

$$a_x = g\sin(\theta)\cos(\omega t + \Phi) \quad (3-13)$$

$$a_y = g\sin(\theta)\sin(\omega t + \Phi) \quad (3-14)$$

These equations correspond to the representation of the gyroscope as lying in the  $xy$  plane, with the centroids of the two temperature sensors lying on the  $x$  axis and those of the two heaters lying on the  $y$  axis. The acceleration signal is applied along a line going through the origin, as shown in Figure 3-18. This axis makes an elevation angle  $\theta$  with the  $z$  axis, and its projection on the  $xy$  plane makes an azimuthal angle  $\Phi$  with the  $x$  axis.

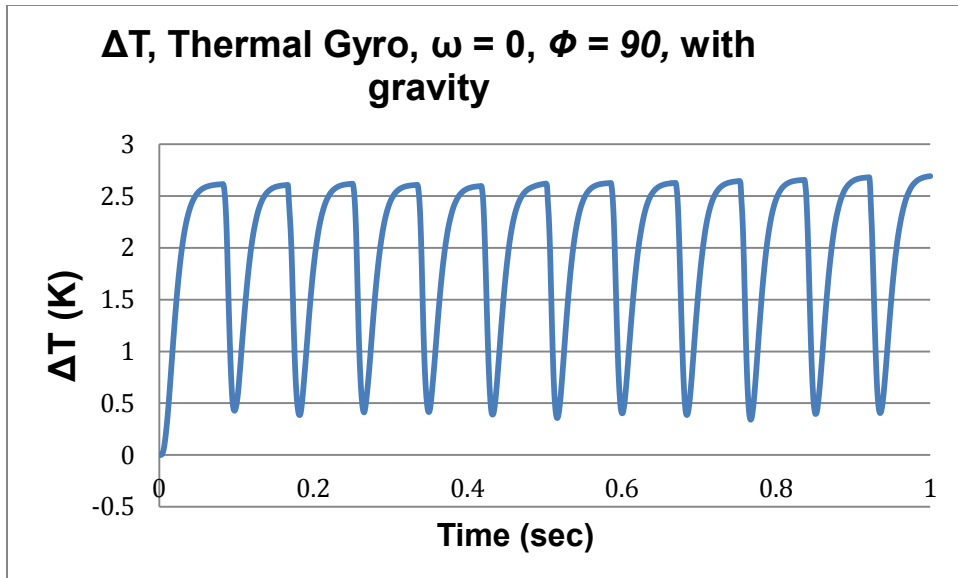




**Figure 3-18 Gyroscope different orientations while gravity is applied**

In order to analyze the impact of acceleration signal (in our simulation acceleration due to gravity) different simulations have been conducted where rotation is zero,  $\omega = 0$  rad/sec and we varied the angle between rotation vector and gravity vector. In the first study we have considered  $\Phi = 90^\circ$  and  $\theta = 0^\circ$ . This corresponds to the gravity vector lying in the  $xy$  plane along the line joining the centroids of the heaters. The simulation results of temperature difference between two temperature sensors show zero output, as we would expect, since the two sensors are symmetrically placed with respect to the gravity vector and hence the impact of buoyancy force on both temperature sensors will be the same, so the temperature difference between them,  $\Delta T$ , will be zero. (No figure is shown for this result, since it would simply be a line coinciding with the  $x$ -axis.)

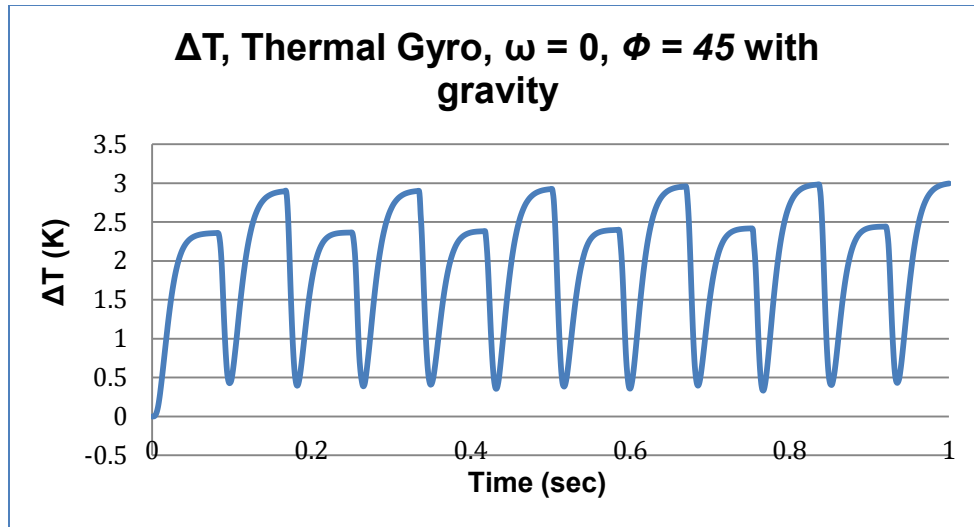
We then simulated a second case where again  $\omega = 0$  rad/sec and  $\theta = 0^\circ$ , but now  $\Phi = 0^\circ$ . This corresponds to the gravity vector again lying in the  $xy$  plane, but now at a  $90^\circ$  angle to the line joining the heaters. Figure 3-19 shows the simulation results of this study.



**Figure 3-19 Temperature difference is monitored while the impact of gravity is considered, and  $\phi = 90$ . Thermal Gyroscope**

Figure 3-19 shows a positive signal where the amplitude of two successive peaks is the same. This is what we would expect: one sensor is always 'higher' than the other, so it is preferentially heated by the buoyant hot air, whichever heater is on. The signal dips as the heaters are switched, since the heating of the sensors is superlinear with respect to the power supplied to the heaters. This signal must be regarded as interference, but, as will be shown, it can be filtered out.

In the next study we have also considered  $\omega = 0$  rad/s, but in this simulation  $\phi = 45^\circ$  and  $\theta = 0^\circ$ . This corresponds to the gravity vector lying in the  $xy$  plane, pointing in a direction intermediate between the heater axis and the sensor axis. Figure 3-20 shows the simulation results of this case.



**Figure 3-20 Temperature difference is monitored while the impact of gravity is considered, and  $\Phi = 45$  Thermal Gyroscope**

The electronic circuits of the gyro use signal processing to filter out interference. In our system we invert the output signal, shift the inverted signal by 180 degrees, and then add the result to the original signal. If the original signal is defined as  $\Delta T(t)$ , the processed signal is  $\Delta T(t) - \Delta T(t+t_1)$ , where  $t_1$  is the heater switching time. Applying this processing to the signal presented in Figure 3-19 will leave us with zero signal. However, applying the same processing to the signal shown in Figure 3-20 will leave us with an oscillating but non-zero signal, where the amplitude of the oscillation signal depends on the difference in height between the high and low peaks. This difference between any two successive peaks in Figure 3-20 is considered to be *unfilterable* interference, because it will not be eliminated by the filtering method we have described. Extensive investigation on this study with different filtering methods has been conducted by another member of our research group at Simon Fraser University, MEMS laboratory [28].

According to Figure 3-20 the amplitude of the interference is 0.59 K, and signal-to-interference ratio could be calculated based on the following formula:

$$SIR = \frac{P_{signal}}{P_{interference}} = \left( \frac{A_{signal}}{A_{interference}} \right)^2 \quad (3-15)$$

Where  $P$  represents power and  $A$  stands for amplitude.

According to Figure 3-17 and Figure 3-20, the calculated SIR is equal to:

$$SIR = \left( \frac{A_{signal}}{A_{interference}} \right)^2 = \left( \frac{0.0052}{0.59} \right)^2 = 7.767 \times 10^{-5}$$

The value of SIR is very low, and further improvements in the design are needed to increase this value.

### 3.9. Conclusion and Discussion

Micromachined Thermal gyroscope characteristics have been analyzed in this chapter. We started our study by investigating the impact of the fluid properties on the gyroscope sensitivity. It has been shown that by using a denser gas inside the cavity, it is possible to increase the gyroscope sensitivity. However, the gas velocity will drop when the density is very high if switching time of the heaters is not long enough to let the gas reach the equilibrium. As a result the device sensitivity will not increase any more. To compensate for the effect of heater switching frequency while using a dense gas, we studied the heater switching frequency's impact on the gyroscope sensitivity. According to the results obtained from simulation, the loss of sensitivity of the high-density gas could be avoided by decreasing the frequency of the heaters so that heaters would have enough time to heat up the gas inside the cavity.

Gas viscosity has also been studied in this chapter. We showed that sensitivity will decrease by using a more viscous fluid. The flow of a viscous fluid is harder to maintain than the flow of a less viscous fluid. This will reduce fluid velocity and, as a consequence, sensitivity will also decrease. Furthermore, in this chapter we studied the impact of heater power on gyroscope sensitivity and, according to the simulation results, sensitivity will increase quadratically with heater power.

As mentioned previously, gas velocity will be decreased by using a dense gas. This observation suggests a new design where gas flow is generated from an external device, and this new

design will be presented in the next chapter. Moreover, Thermal MEMS gyroscope shows very low SIR, and consequently design refinement to improve SIR is necessary. In the next section, we will introduce a new model referred to as “Forced-convection gyroscope” where an external force has been applied to move the stream of gas.

## 4. Forced-Convection Gyroscope

### 4.1. Introduction

In this chapter we will illustrate a new design of Thermal MEMS gyroscope that we will refer to as “Forced-convection Gyroscope”. As explained in the discussion section of Chapter 3, we expect to observe higher sensitivity with this design because this design has lower Ekman Number.

Furthermore, the signal-to-interference ratio (SIR) of the Thermal MEMS gyroscope presented in the previous chapter is compared with this model. In this design the output signal is increased by adding external force to the system. This force, generated by electrostrictive or magnetic actuators [29-34], or, in our work, a simple pump, will create an alternating gas stream. This stream is subsequently heated, and is deviated toward alternating temperature sensors by the Coriolis effect [29-34]. A heating element is still used, but its primary purpose is now to warm the flowing gas so that it can be detected by the temperature sensors. Furthermore, a refined model of this design referred to as “Heated-sensor Forced-Convection” is presented in which the heaters are completely eliminated, and the temperature sensors function as hot-wire anemometers [29-34].

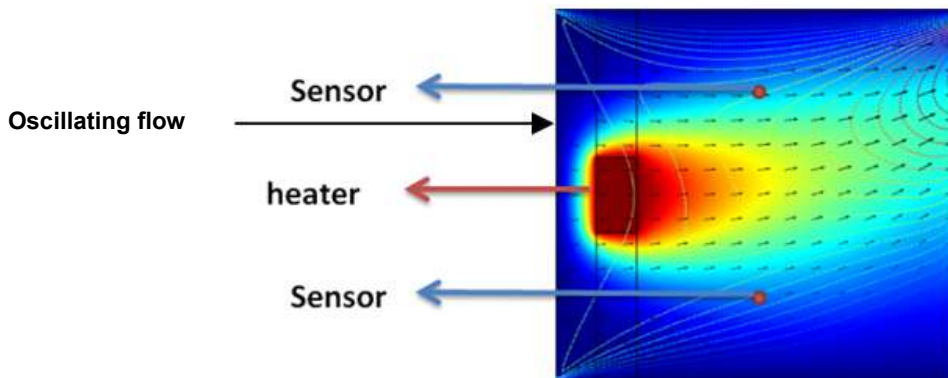
Development of micromachined Forced-Convection Gyroscopes [30, 31], also known as “Thermal Gas Gyroscopes”, goes back to before 2005. However they showed inadaptability with batch processing in MEMS [29]. A new MEMS-compatible approach on the millimeter scale has been presented in 2005 [29] and further improvements have been made in the following years (2007) [30, 31]. In these designs a piezoelectric pump has been used to force the gas flow through a fine nozzle and a micro-thermal-sensing element has been used as a hot wire anemometer to sense the gas deflection caused by rotation [29-34]. These designs of Forced Convection Gyroscope had limited ability to sense high flow deflection resulting from high rate of rotation. This problem resulted from the inappropriate placement of temperature sensors (hot wires) [31]. In this chapter we will present temperature sensor-placement optimizations to

compensate for this problem. Moreover, we will show that our ultimate design of forced-convection gyroscope has an advantage in comparison to its precedents [29-34] by reducing the impact of acceleration. Our experimental set-up is demonstrated at the end of this chapter.

## 4.2. Forced-Convection Design, One heater

In order to address the problems of Thermal MEMS gyroscope mentioned in the previous chapter an alternative design has been modeled where an external force has been added to the system.

We have been able to use the heat transfer module of COMSOL to model this design; a specially-derived set of equations is no longer necessary, since we are no longer modeling a gas flow created by expansion of a heated gas.

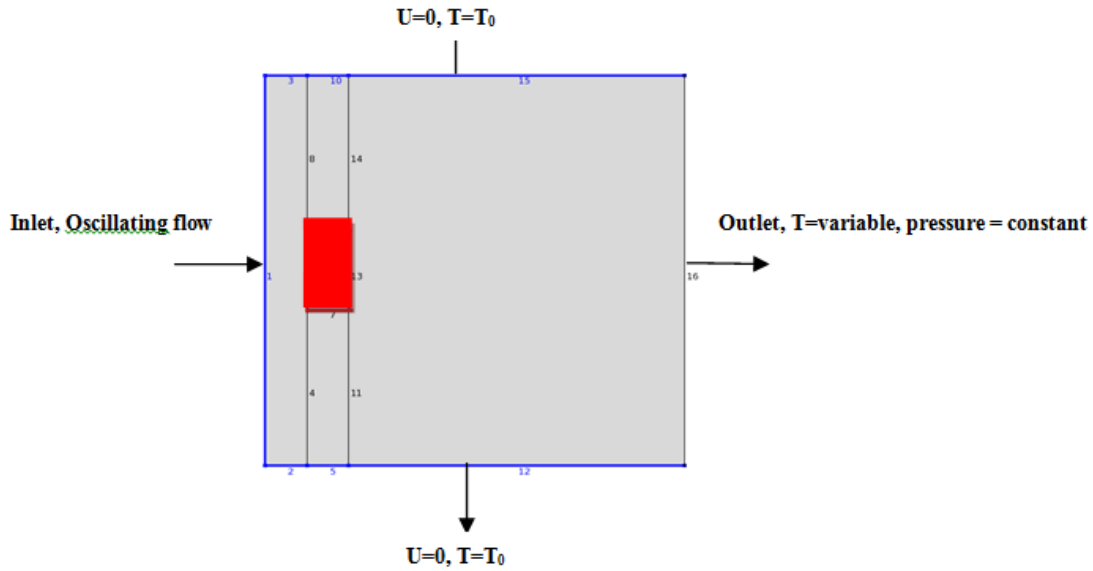


**Figure 4-1 COMSOL Model, deviated gas due to rotation is shown**

Figure 4-1 shows a gas-filled cavity, with one heater, coloured red, on the left and two temperature sensors on top and bottom. Unlike the previous design, in this case the heater is continually on. Temperature sensors in our model are simply notional points at which we monitor temperature. In the real device they can be temperature-sensitive resistors whose temperature will change if they come into contact with hot gas.

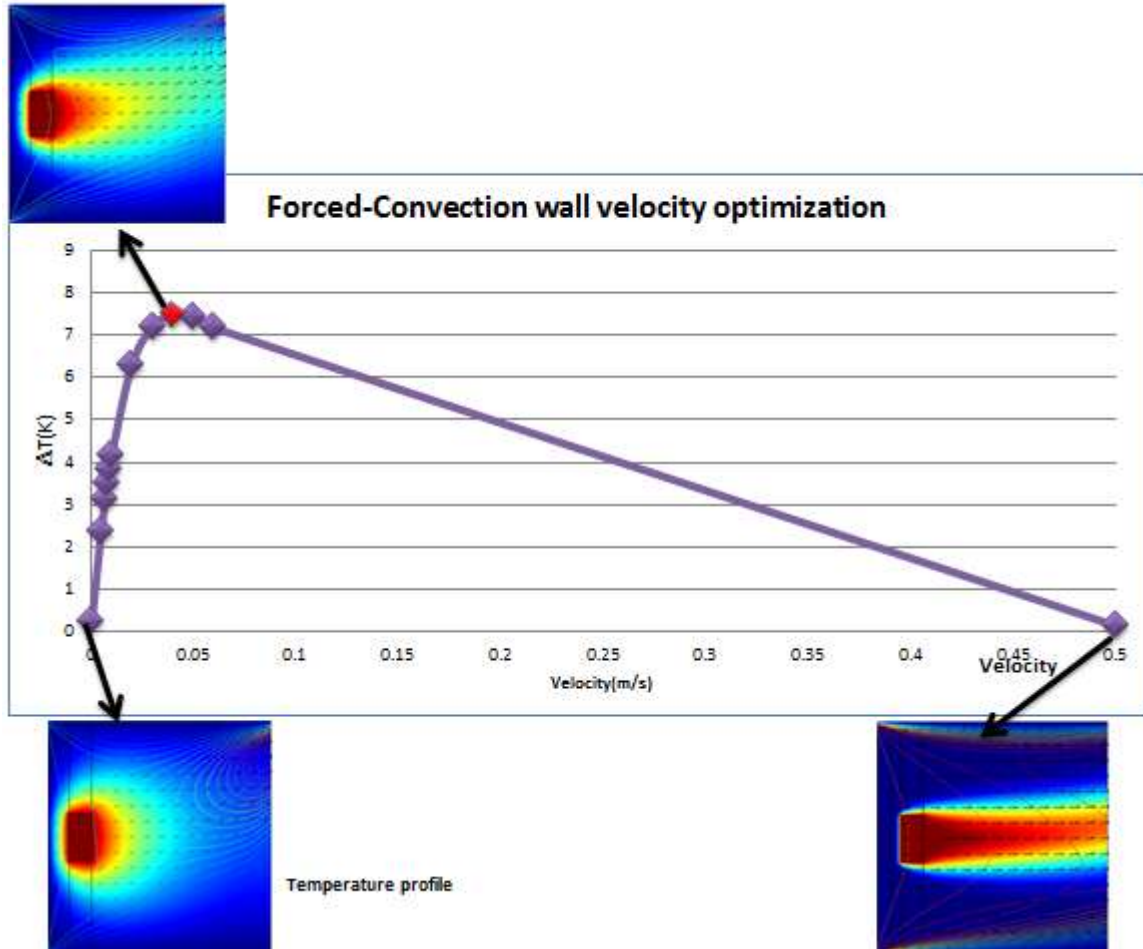
SF<sub>6</sub> has been chosen as a dense gas to fill the cavity in the simulations. In this simulation we have specified an oscillating flow of gas as the left-hand boundary condition. This oscillating flow will push the hot gas surrounding the heater to the right and, if the device is rotating around an axis orthogonal to the plane containing the heater and temperature sensors, the Coriolis force will deviate the flow. The deviated flow will reach the temperature sensors but because the flow has been deviated, one temperature sensor will receive more heat than the other. If we monitor their temperature difference we are able to correlate it with speed of rotation. The small black arrows in Figure 4-1 show the path of gas that has been deviated from its straight path as a result of rotation. In this figure it is obvious that the top temperature sensor is receiving more heat. Boundary conditions are shown in Figure 4-2. The temperature boundary condition is set at  $T_0$  for all the boundaries except the left and right-hand boundaries during periods of outward flow, when the temperature of the outflowing gas is calculated by the model. The top and bottom boundaries are defined as having zero flow in both  $x$  and  $y$  directions. The velocity of the gas at the left-hand boundary is represented by the equation:  $U = U_0 \sin(\omega t)$ . The right hand boundary condition is defined as constant pressure, and the flow rate through this boundary is determined by calculation.





**Figure 4-2 Boundary condition of Forced-convection design**

Simulations were carried out for inlet speeds ranging from 0.0005 m/s to 0.5 m/s, and the acceleration due to gravity is considered to be zero. Each data point in Figure 4-3 represents the temperature difference between two temperature sensors vs. wall velocity. The velocity profile shows that, for relatively small velocities, the gas does not gain enough velocity to be significantly deviated due to the Coriolis effect during rotation. If the velocity of the gas is too great, the Coriolis effect will not have enough physical space to act on the gas flow due to geometric constraints, and as a result the temperature difference at the temperature sensors is minimal. There is an optimal wall velocity, found to be 0.045 m/s for the given cavity dimensions and the given placement of the temperature sensors, where the Coriolis effect has the greatest impact on the temperature difference between temperature sensors.

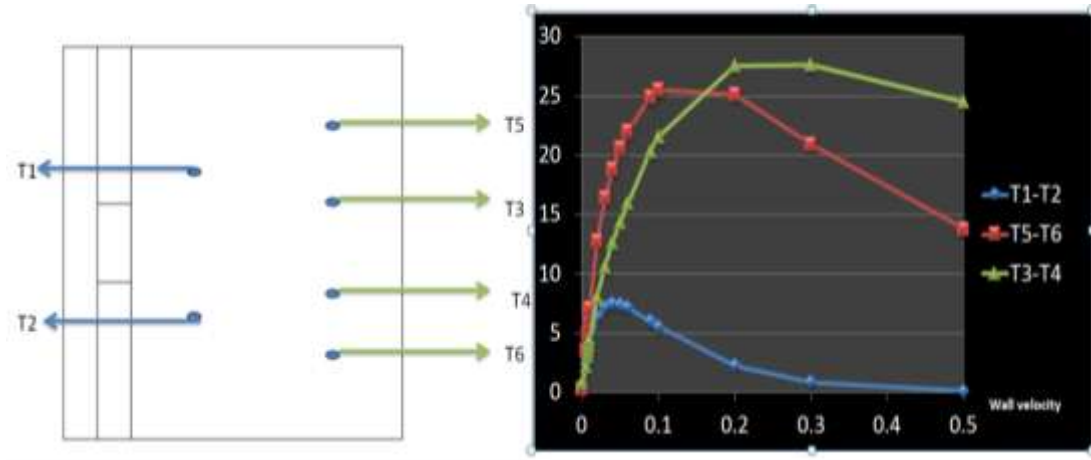


**Figure 4-3 Wall speed optimization**

The red dot in Figure 4-3 shows the optimum speed for the boundary condition in our model. According to Figure 4-3 the optimum velocity of the oscillating flow is 0.045 m/s.

We continued the simulation by finding the optimum location for our temperature sensors. As mentioned above, while it is possible to optimize wall velocity (due to an external force) for a given geometry, we can also optimize temperature sensor placement given a varying set of wall velocities. Different positions of the temperature sensors have been considered for varying wall velocities, shown in Figure 4-4.

$T_1, T_2, T_3, T_4, T_5$  and  $T_6$  are temperature sensor locations. Temperature differences between the pairs  $(T_1, T_2), (T_3, T_4)$  and  $(T_5, T_6)$  are monitored.

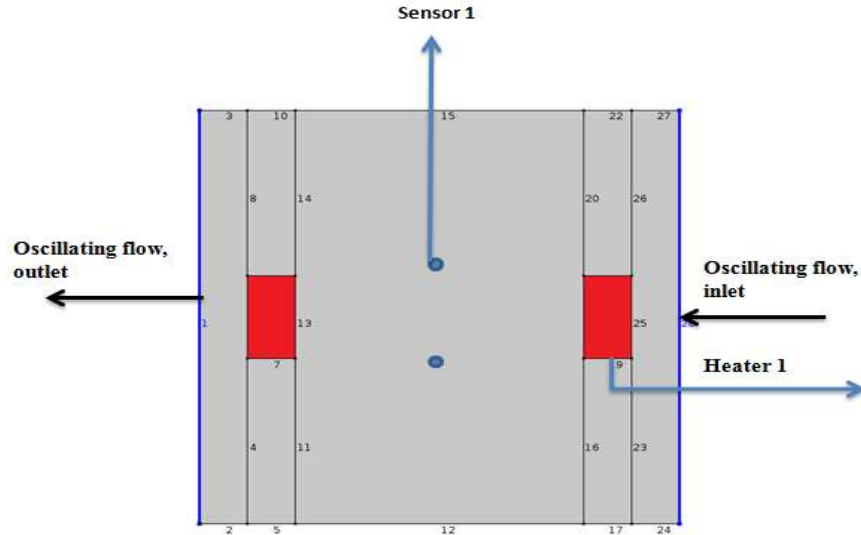


**Figure 4-4 Temperature sensor location optimization**

It can be seen that for the velocity ranges we have considered, it is important to allow enough space for the Coriolis effect to act and to place the temperature sensors far away enough from the heater to sense the gas temperature at the point of greatest deviation. For example, the lowest curve in Figure 4-4 shows very low sensitivity because the temperature sensors are close to the heater and the heated gas flow is not greatly deviated before being detected by temperature sensors. The other important feature that we can observe is that when the velocity of the wall is high, the temperature sensors must be placed closer together. This is shown in Figure 4-4, where the curve corresponding to the temperature sensor pair  $(T_3, T_4)$  is the most sensitive at high flow rates. On the other hand, when the boundary velocity is low it would be better if the temperature sensors were placed farther apart, as shown in Figure 4-4, for the curve corresponding to the temperature sensor pair  $(T_5, T_6)$ .

### 4.3. Forced-Convection Design, Two heaters

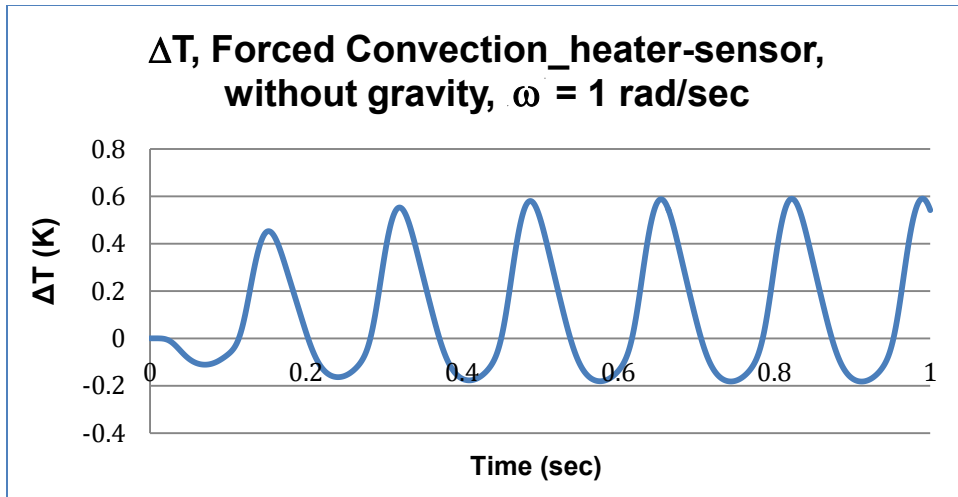
In the next design, to maintain symmetry a second heater has been added to the model as shown in Figure 4-5.



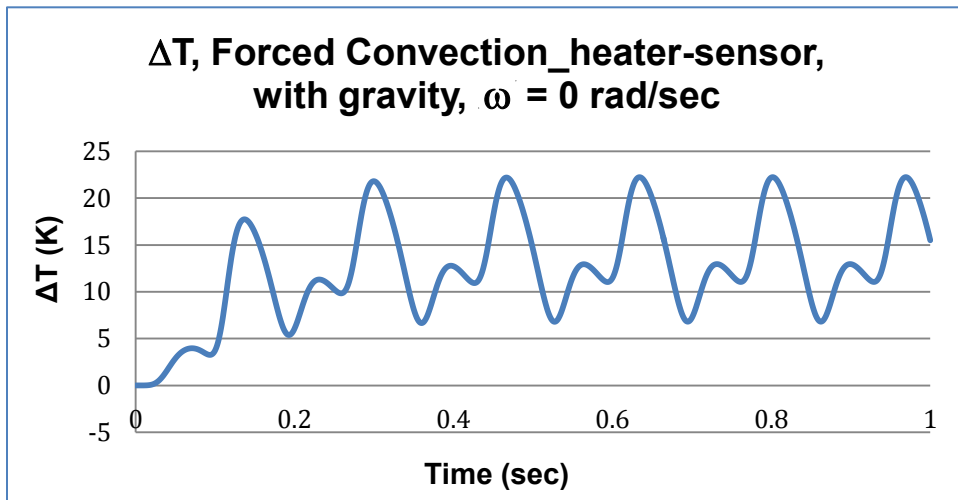
**Figure 4-5 COMSOL model, places of temperature sensors, heaters and oscillating flow are shown, forced-convection design**

The model structure is an exact duplicate of Thermal gyroscope. The only difference, as shown, is the boundary condition where we have specified an externally-generated flow rate. Also in this model both of the heaters are continuously on, though their primary purpose now is to warm the flowing gas so that it can be detected by the temperature sensors.

Simulations were carried out for flow speeds with 0.01 m/s amplitude and 6 Hz frequency. The results for two different cases, one without imposed acceleration and the other subject to acceleration, are shown in Figure 4-6 and Figure 4-7 respectively. In both cases the acceleration is due to gravity.



**Figure 4-6** *Temperature difference is monitored while the impact of gravity is eliminated, Forced convection Gyroscope, Heater-sensor model*



**Figure 4-7** *Temperature difference is monitored while the impact of gravity is considered, Forced convection Gyroscope, Heater-sensor model*

Figure 4-6 shows the output signal where acceleration is absent. The oscillating temperature difference between two temperature sensors as observed in Figure 4-7 is not orientated symmetrically in response to the y axis. It can be seen that the amplitude of the peaks are higher than the valleys and the peaks are sharper than the valleys, which are the results of difference in flow rates over the right and left boundaries of the cavity. We confirmed this

conclusion by applying the sinusoidal-flow boundary condition to the right boundary instead of the left boundary, and observed that as a result these asymmetries were reversed.

In the presence of an acceleration along the  $y$ -axis, as shown in Figure 4-7, the observed signal is vertically shifted upward. This happens because when the device is not rotating the upper temperature sensor is always surrounded by hotter gas than the lower temperature sensor, due to buoyancy. Also in Figure 4-7 two successive peaks are observed. In each cycle, the bigger peak coincides with the maximum value of rightwards flow, and the smaller peak coincides with the maximum value of leftwards flow.

The difference between two successive peaks in Figure 4-7 is unfilterable interference. The signal-to- interference ratio can be calculated based on Equation (3-15):

$$SIR = \left( \frac{A_{signal}}{A_{interference}} \right)^2 = \left( \frac{0.77}{9.23} \right)^2 = 7 \times 10^{-3}$$

Comparing SIR of this system with previous system, Thermal gyro, the SIR has been improved 100 times. However, the magnitude of the output signal still depends on  $\theta$ . This encouraged us to design a new model, referred to as Heated-Sensor design, which will be presented in Section 4.5.

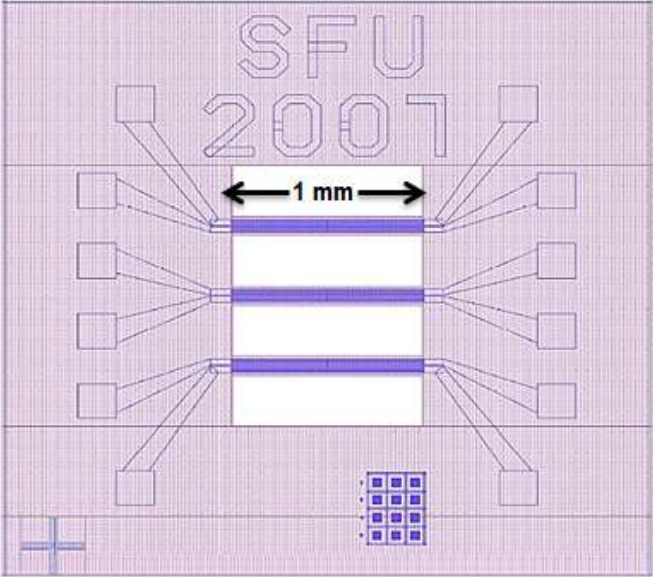
In the next section the fabrication process and experimental set-up for the forced convection model is presented.

## 4.4. Fabrication

Positive simulation results motivated us to fabricate a prototype of the “Forced Convection MEMS” gyroscope. Producing a fully functional forced-convection gyroscope is beyond the scope of this thesis. The prototype reported here, however, allowed us to demonstrate a subset of this device’s operation and function.

The first step in MEMS fabrication process is to design a mask to be used for the microfabrication process. Figure 4-8 shows the mask layout of a thermal gyroscope built for

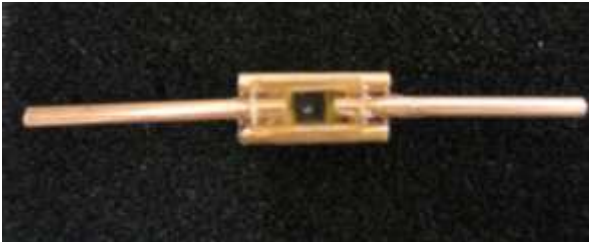
another research project. To add external force to the Thermal MEMS gyro we used an existing chip and employed an external pump to generate oscillating flow to the system.



**Figure 4-8 Device mask layout**

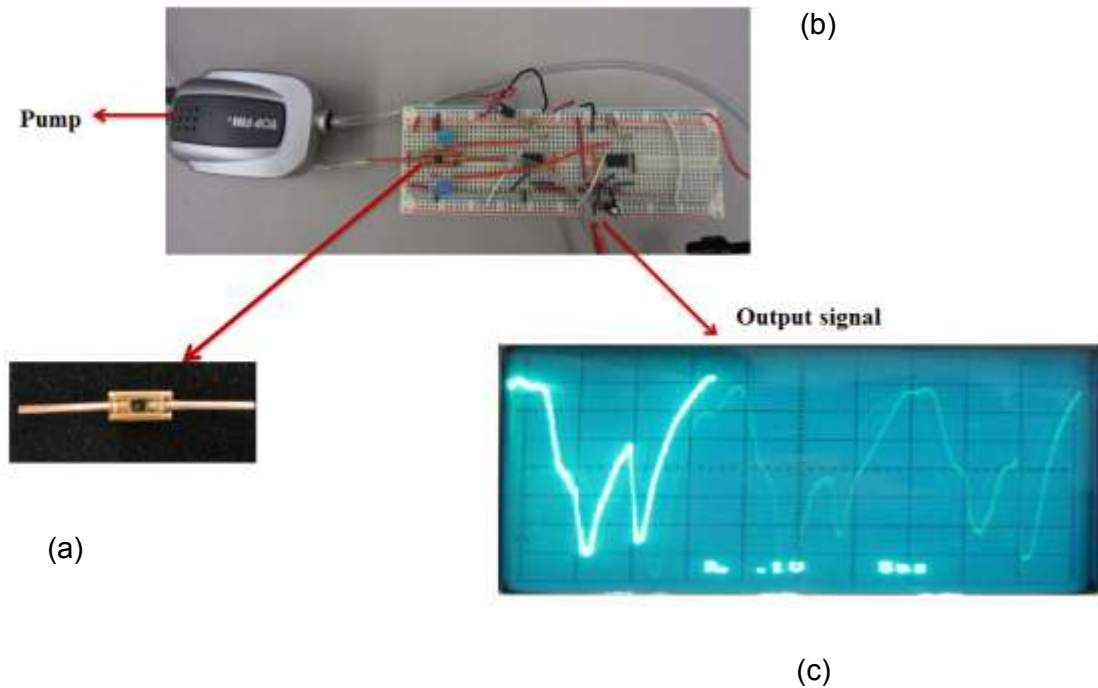
In the above picture each bridge can be used for either temperature sensor or heater, they are simply resistors whose resistance will change if they are in contact with hot air.

We added copper tubing to the packaging and sealed the package as shown in Figure 4-9.



**Figure 4-9 MEMS fabricated chip with copper tube**

We added a circuit for heating the temperature sensors and observed whether it is possible to cool them down with pump, as shown in Figure 4-10.



**Figure 4-10 Setup for detecting sensors functionality**

Figure 4-10 (c) shows the output signal, cooling down and heating up are shown in this figure.

We can observe similarity between experimental output signal of Figure 4-10 (c) and COMSOL simulation results, Figure 4-7. Both figures show the same path with different vertical shift depending on the value of  $\theta$ .

The next step will be having a platform to rotate the system and observe the output signal.

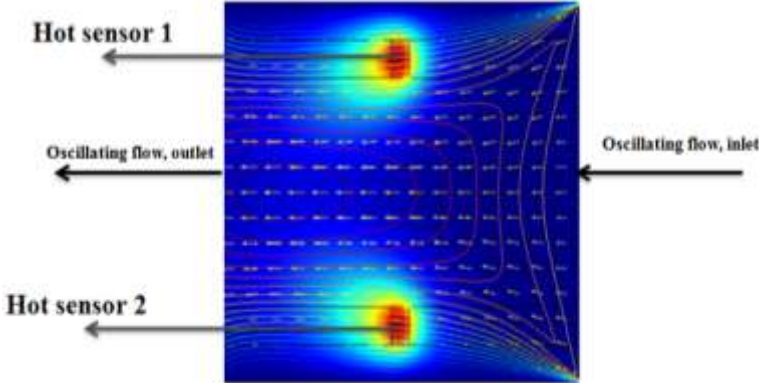
## 4.5. Heated-Sensor Design

In this system we completely eliminated the heaters and replaced the temperature sensors with heated sensors which will work as “Thermal Mass Flow Meter”. The temperature sensors will be *cooled* by deviated gas, again yielding temperature differences between the two temperature



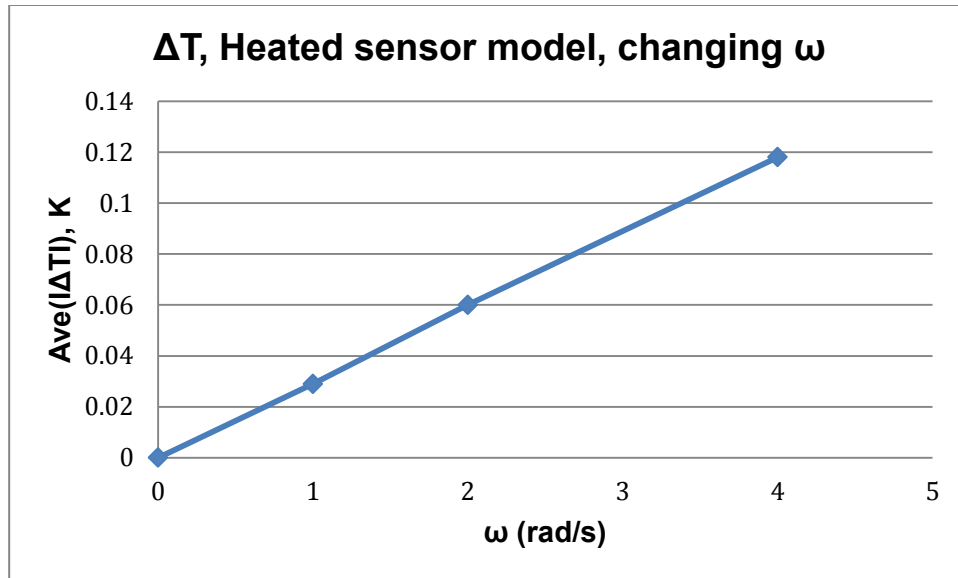
sensors. This technique has the reverse strategy in comparison with previous technique. In the previous method, hot gas produced by the heaters would reach the temperature sensors and heat them up, in this method cool gas will travel toward hot temperature sensors and cool them down. This method works exactly as a thermal anemometer works: the flow of air cools small heat-sensitive temperature sensors which are in contact with the flow.

Figure 4-11 shows a new model based on the above method, which has been designed and simulated in COMSOL.



**Figure 4-11 New Gyro design based on hot sensors**

In the next step of this study we monitored the relation between angular rate and output signal of Heated-Sensor design. We have considered  $\omega = 1 \text{ rad/s}$ ,  $\omega = 2 \text{ rad/s}$  and  $\omega = 3 \text{ rad/s}$  cases, then plotted the amplitude of output signal in each case in response to angular rate.

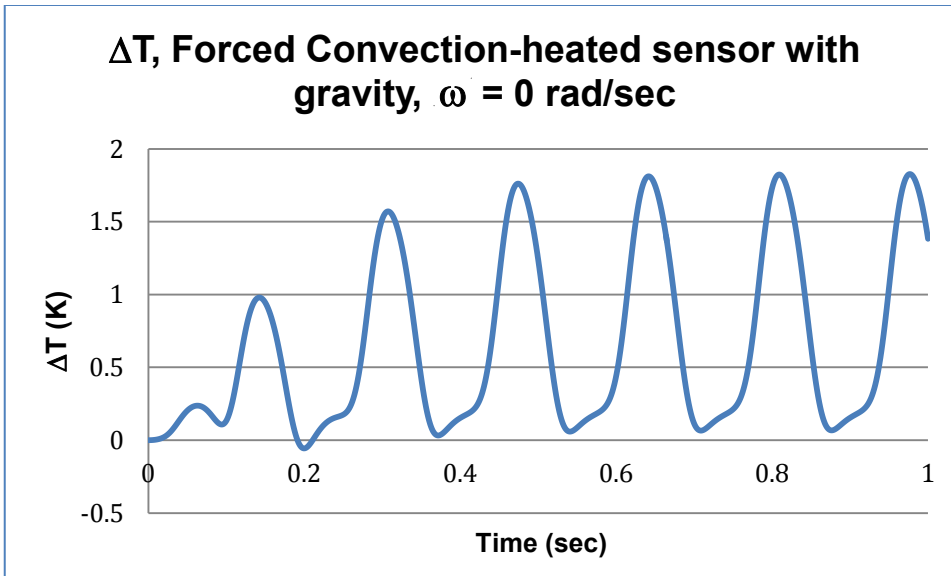


**Figure 4-12** Output signal with different angular rate

According to Figure 4-12 the relation between output signal and angular rate is linear. However for sufficiently high angular rate the curve would level off. This could be compensated for by adding extra temperature sensors for high angular rate measurements, as explained earlier in this chapter.

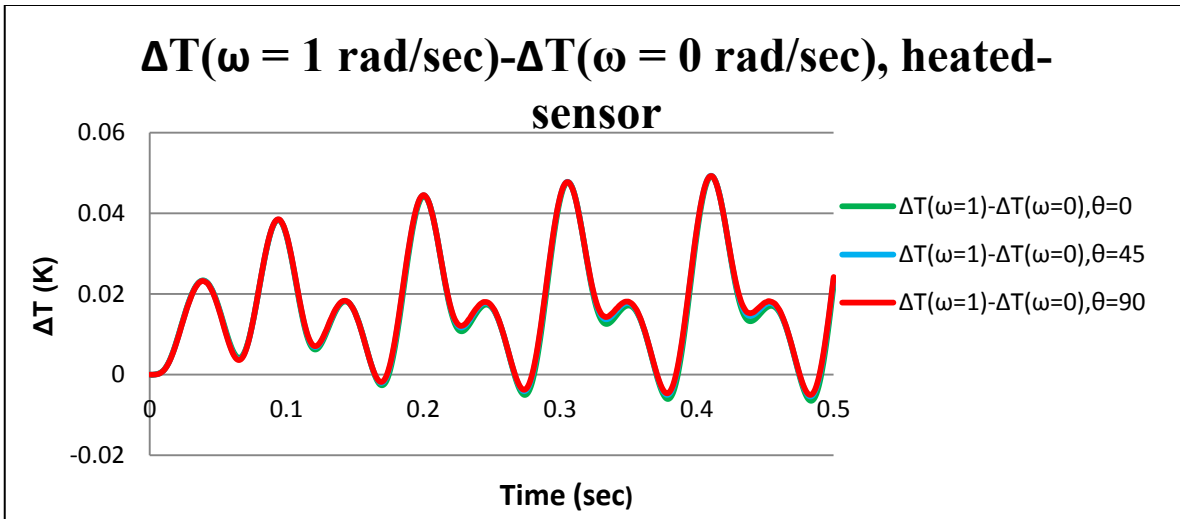
## 4.6. Signal Correction

Figure 4-13 shows the result of a simulation of the heated-sensor gyroscope in the absence of rotation and with gravity acting along the y-axis. This will produce a differential temperature signal varying in phase with the imposed flow, which interferes with the measurement of rotation and hence counts as interference. However, if the gyroscope can store a sample of this signal, it can subsequently detect a *change* caused by rotation. This requires a more complex form of filtering: a sample of the differential signal for non-rotating operation must be stored, then subtracted from subsequent signals. To evaluate this method of signal correction, we conduct a series of studies, rotating and non-rotating, for different values of the tilt angle  $\theta$  (the angle that the normal to the plane of the gyro makes with the gravity vector).



**Figure 4-13 Temperature difference is monitored while the impact of gravity is considered, Forced convection Gyroscope, Heated-sensor model**

Figure 4-14 shows the corrected output signal for different values of  $\theta$ . In all these cases the non-rotation signal ( $\omega = 0$  rad/s) has been subtracted from the rotation signal. All three curves are superimposable, showing that the corrected output signal does not depend on  $\theta$ .



**Figure 4-14 Temperature difference of heated-sensor design, different values of  $\theta$  are considered**

Figure 4-14 shows that the signal stabilizing from 0.35 sec onwards. Whereas ‘corrected’ signals for the previous Two-Heater Forced-Convection gyro showed dependence on  $\theta$ , meaning that the ‘corrected’ signal still included effects of the buoyancy force, the current Forced-convection Heated-sensor model has no such dependence on  $\theta$ , as shown by Figure 4-14. This could be considered the main advantage of this design in comparison with previous designs.

The reason for this independence of  $\theta$  is thought to be that in the heated-sensor model, the hot sensors are small and placed far apart from each other. As a result they will not affect each other via the buoyancy force. So differences in their temperature will result solely from the deviation of the oscillating flow by Coriolis force, which will cool down one hot sensor in preference to the other.

## 4.7. Conclusion

A new design of Thermal MEMS gyroscope has been modeled which is referred to “Forced Convection MEMS Gyroscope”. Different techniques have been considered to eliminate the

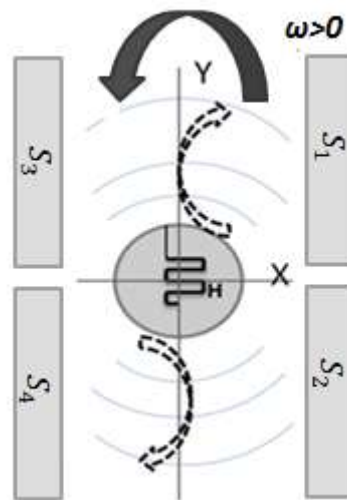
impact of acceleration signal and extract the signal precisely. Hot sensor model could be considered as the best model and is functional even if the device is rotating in different angles of inclination. A prototype of the device has been fabricated, and a practical set up is constructed to extract sensor signal.

#### **4.8. Future work**

As future work we are looking forward to building a rotary platform to rotate the whole system and extract the rotation signal to be compared with simulation results.

## 5. Three-Axis MEMS Gyroscope

In this new design, the two heaters presented in the first model have been merged to build a new model that we will refer to as “One-heater Thermal Gyroscope” shown in Figure 5-1. We will show that this new model can detect rotation about the y and z axes in addition to the x axis. Furthermore, we will illustrate techniques for eliminating the impact of acceleration signal resulting from gravity.



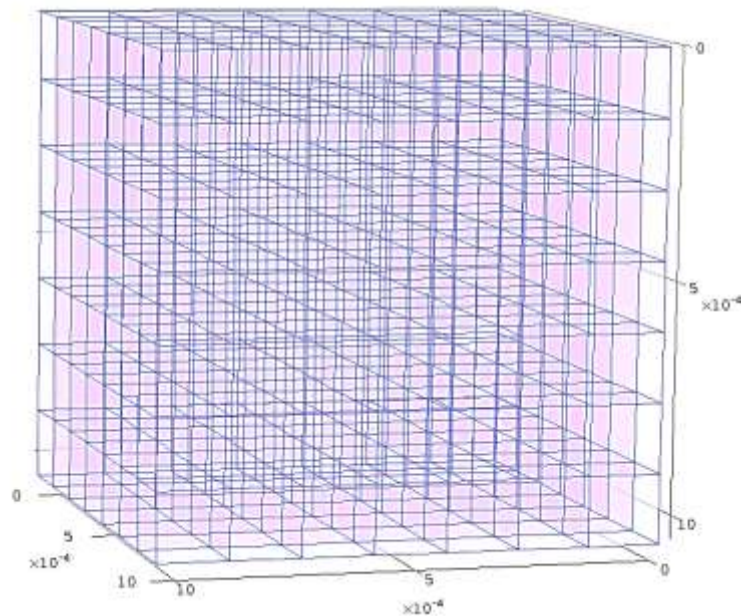
*Figure 5-1 Deviation of a warm fluid bubble in One-heater Thermal Gyroscope*

### 5.1. Simulation Design

A three-dimensional geometric model of a micromachined cavity was constructed and meshed using the COMSOL modeling package, and the fluid in the cavity was represented by Equation

(2-1) to (2-6). Sulfur hexafluoride,  $\text{SF}_6$  has been chosen as a dense gas to fill the cavity in the simulations. The properties of sulfur hexafluoride and Si walls are shown in Table 1 and Table 2.

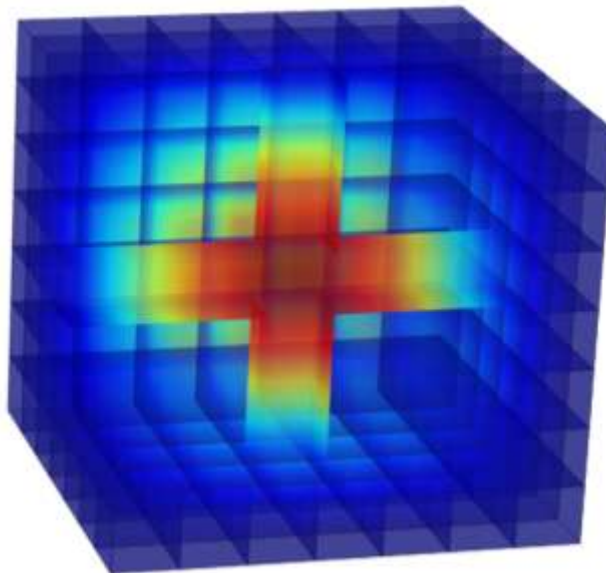
In order to make the structure meshing symmetrical we have constricted our model from small cubes each of them 0.15 mm on a side. The main structure, a cube with 1.05 mm sides, is constructed from these small cubes, as shown in Figure 5-2.



**Figure 5-2 COMSOL structure, constructed from small cubes**

A heater in the form of a “plus” shape in the middle of the cube is shown in Figure 5-3. The thickness of the heater in our model is 0.15 mm. The heater is pulsed on and off at regular intervals of 0.04 seconds, corresponding to a frequency of 25 Hz. Our basis for selecting this switching interval is that we want to maximize the measured temperature difference between

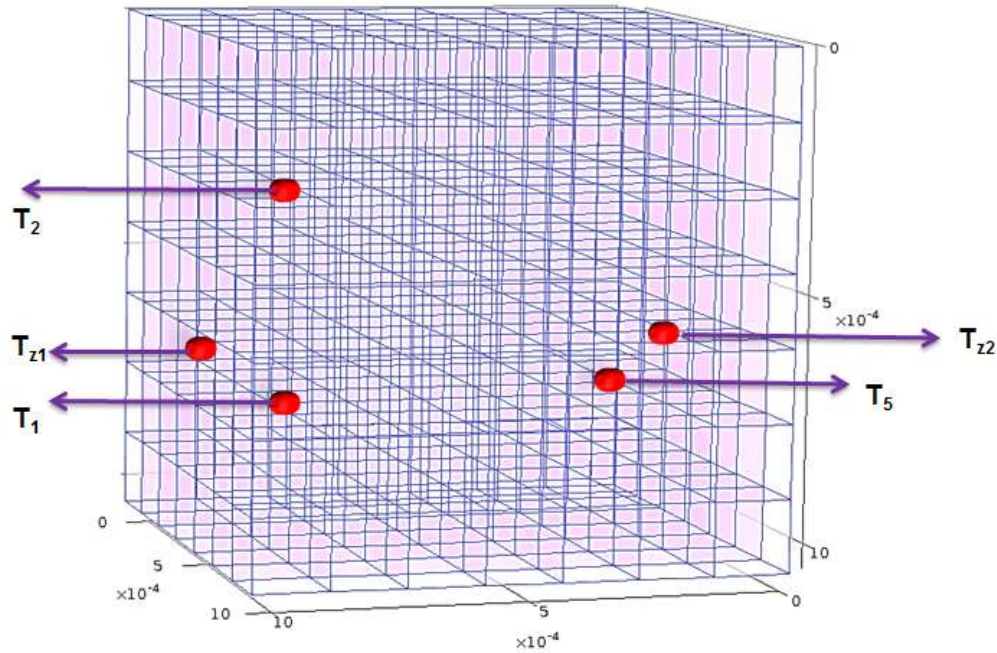
temperature sensors. This difference is due to the deflection of the expanding gas flow by the Coriolis force, and will therefore reach a maximum when the average flow rate of the expanding gas is at a maximum. When the heater is switched on, the temperature of the gas around it increases until an equilibrium temperature is reached, at which point the expansion flow stops and the gyroscope ceases to function. We therefore set the heater to pulse off just before the equilibrium temperature is reached. Calculation and experiment show that this period is about 0.04 seconds.



***Figure 5-3 COMSOL structure, shows the heater in a plus shape***



Temperature sensor positions are shown in Figure 5-4.



**Figure 5-4 Places of temperature sensors in three-dimensional model based on optimization**

In Figure 5-4,  $T_1$ ,  $T_2$ ,  $T_5$ ,  $T_{z1}$ , and  $T_{z2}$  are the temperature sensor locations.

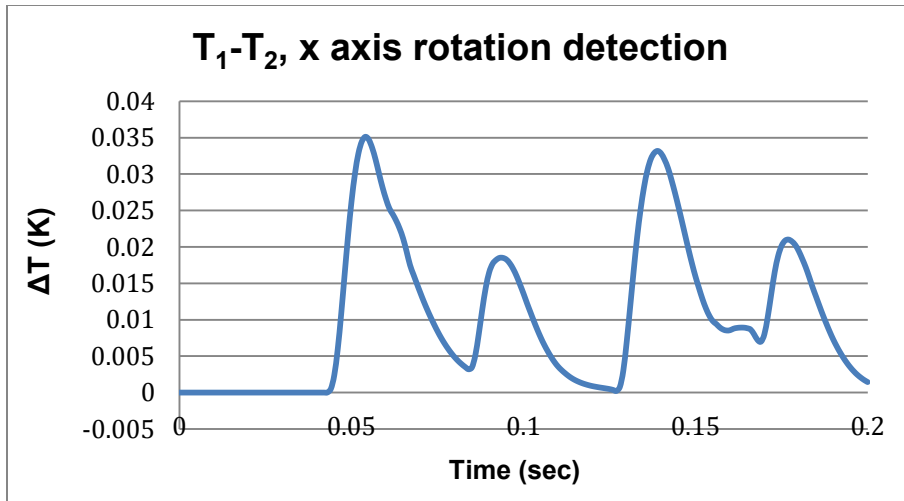
If the temperature sensors were placed symmetrically within the cavity, the fluid deflection due to Coriolis effect toward each of the temperature sensors would be the same, so monitoring temperature differences between temperature sensors will generate no signal. In order to observe temperature differences between temperature sensors it is necessary to disturb the symmetry and place the temperature sensors in asymmetrical places. Table 3 shows the temperature sensor locations in  $x$ ,  $y$  and  $z$  coordinates, where the coordinate origin is at the left back lower corner of the cavity.

**Table 3 Temperature sensor locations in three-dimensional model**

Sensor name	Function	Location (x,y,z) mm
$T_1$	x & y rotation monitoring	(0.3,0.3,0.3)
$T_2$	x rotation monitoring	(0.3,0.75,0.3)
$T_5$	y rotation monitoring	(0.75,0.3,0.3)
$T_{z1}$	z rotation monitoring	(0.2,0.42,0.45)
$T_{z2}$	z rotation monitoring	(0.85,0.42,0.45)

By monitoring the temperature differences between  $T_1$  and  $T_2$  we are able to detect rotation along x axis, also by monitoring  $T_1$  and  $T_5$  we can sense rotation along y axis.  $T_{z1}$  and  $T_{z2}$  are the temperature sensors placed for detecting rotation along z axis.

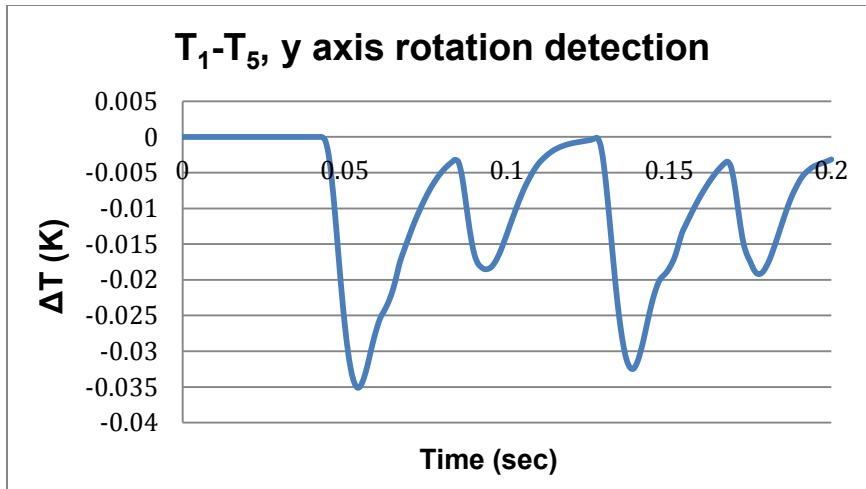
Figure 5-5 shows the simulation results of rotation about the x axis. In this study  $\omega_x = 20$  rad/s,  $\omega_y = \omega_z = 0$ .



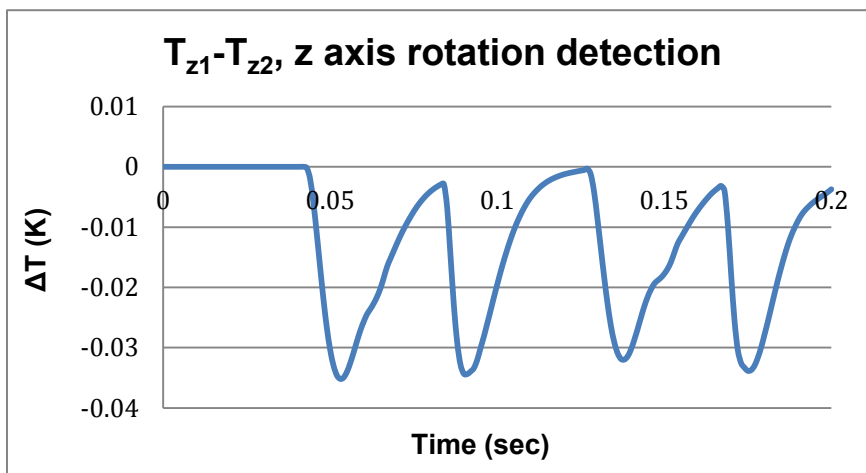
**Figure 5-5 Temperature difference between two temperature sensors, for detecting rotation along x axis**

Figure 5-5 shows that the signal of  $T_1 - T_2$  is measurable, and it was observed that the signals from the other pairs of temperature sensors are negligible. In other words, the temperature sensors designed to detect rotation along x axis picked up a significant signal and the other pairs of temperature sensors showed negligible noise. These results matched our expectation.

Other cases have also been simulated. In Figure 5-6, (a-b), simulation results of rotation about the y axis have been shown, in this study,  $\omega_y = 20$  rad/s,  $\omega_x = \omega_z = 0$ .



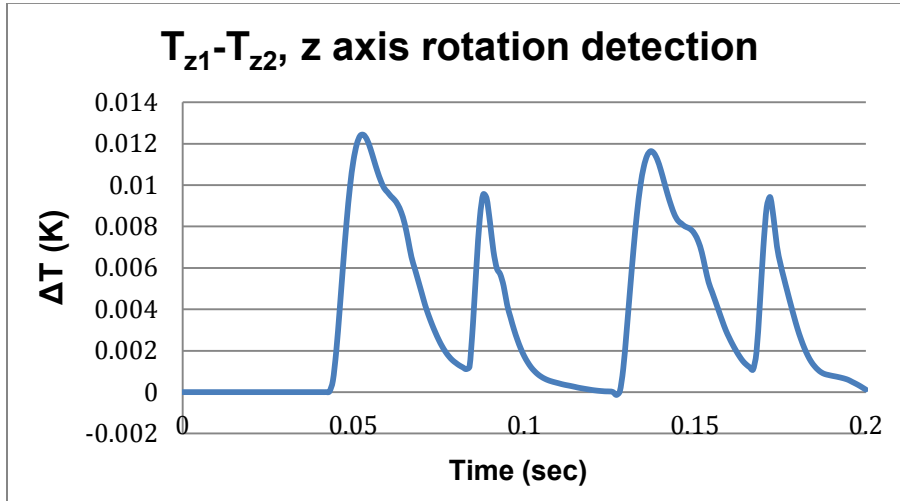
**Figure 5-6 (a) Temperature difference between two temperature sensors, for detecting rotation along y axis**



**Figure 5-6 (b) Temperature difference between two temperature sensors, for detecting rotation along z axis**

Simulation results show the temperature difference between  $T_1$ ,  $T_2$  was negligible, since there was no rotation about the x axis. But, disturbingly, Figure 5-6 (b) shows a significant signal regardless of the fact that there was no rotation about the z axis. Before drawing any conclusion at this stage, we continued the work by simulating the case of rotation about the z axis while

rotation about the two other axes,  $x$  and  $y$ , was considered to be zero, in other words,  $\omega_z = 20$  rad/s,  $\omega_x = \omega_y = 0$ . The results of this study are shown in Figure 5-7.

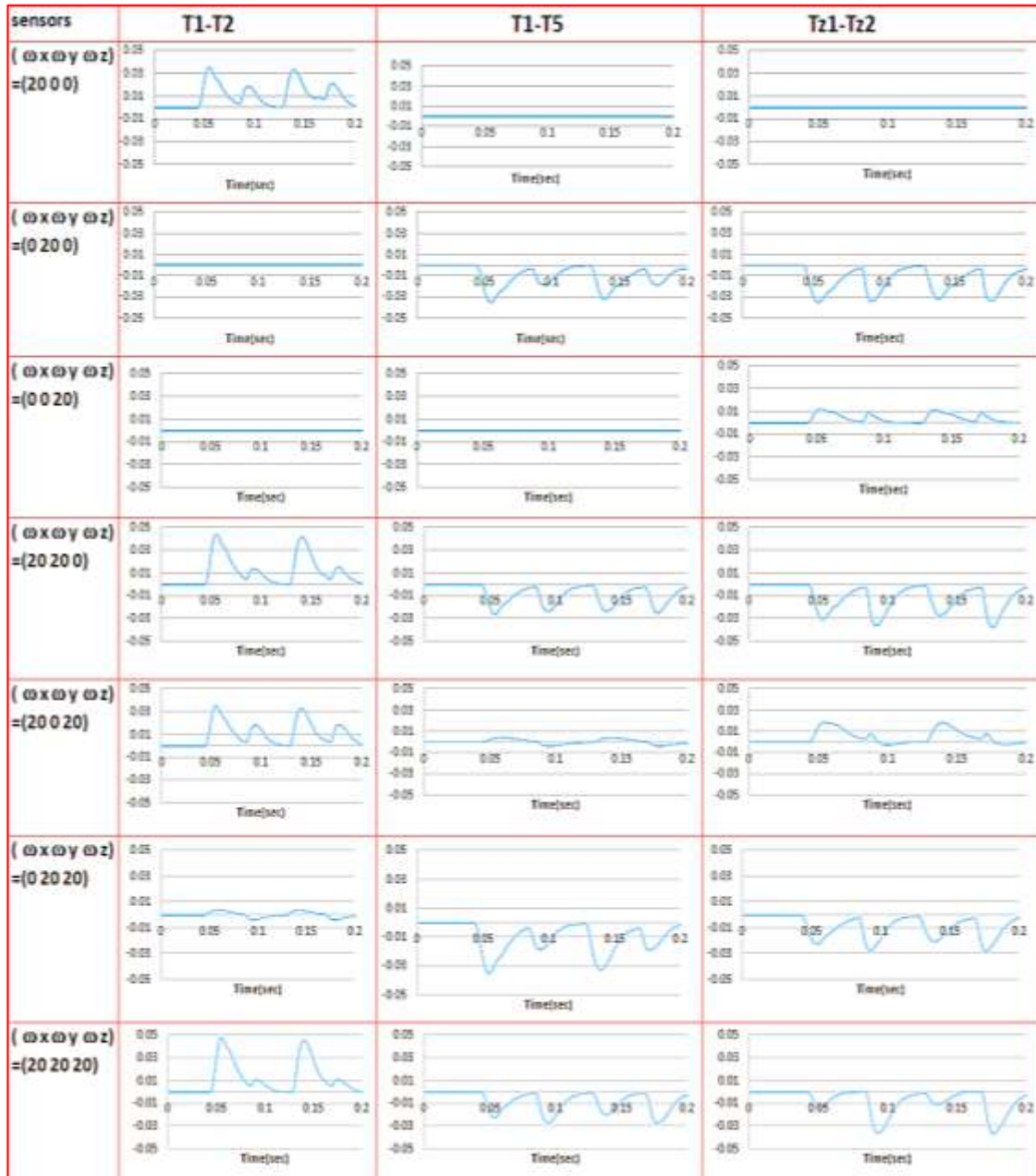


**Figure 5-7 Temperature difference between two sensors, for detecting rotation along y axis**

Simulation results show that the temperature differences between the sensor pairs ( $T_1, T_2$ ) and ( $T_1, T_5$ ) were negligible while rotation about  $x$  and  $y$  axes was zero. But the pair ( $T_{z1}, T_{z2}$ ) does yield a significant signal, shown in Figure 5-7, and represents rotation about the  $z$  axis.

Each case shows unique signals. This makes it possible to monitor all three sets of temperature sensors and compare the results with Table 4 to resolve rotation about different axes.

**Table 4 Simulation results of different rotation cases**



## 5.2. Gravity/Acceleration Effect

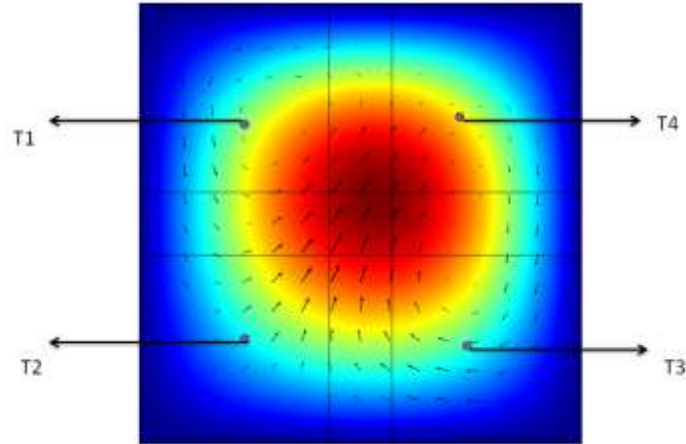
The impact of acceleration due to gravity or other imposed accelerations has not yet been considered. For simplicity we have constructed a two-dimensional model of the gyroscope where the buoyancy terms in Equation (2-4) and (2-5) are given by.

$$a_x = g\sin(\theta)\cos(\omega t) , a_y = g\sin(\theta)\sin(\omega t)$$

In this design  $\omega$  represents rotation about the axis perpendicular to the  $xy$  plane, which we can think of as the  $z$  axis, and  $\theta$  represents the angle that the acceleration vector makes with the  $z$  axis.

In the presence of gravity, it is no longer necessary to pulse the heater on and off to produce currents of heated gas. Instead, we can keep the heater on continually and rely on the buoyancy effect to create natural convection currents, which will be deflected by the Coriolis force. Thermal MEMS gyroscopes based on natural convection have been analysed by previous researchers. However, they failed to measure three axes of rotation [35].

Figure 5-8 shows the two-dimensional model of Thermal gyroscope. Small black arrows show the direction of fluid velocity within the cavity.





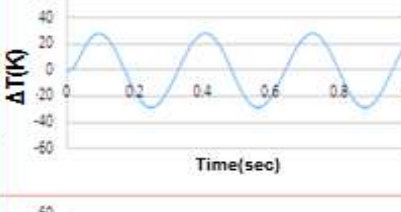

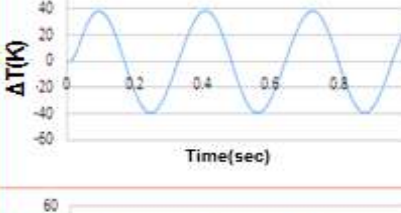

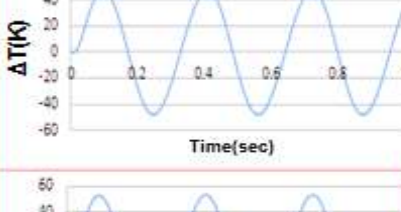

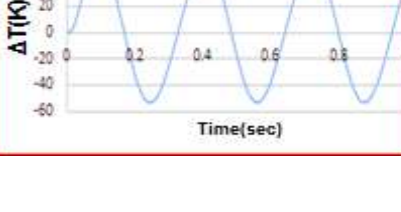
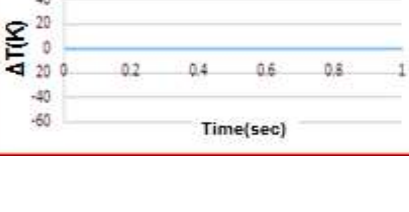


**Figure 5-8 Two-dimensional Thermal gyro model, gravity is added to the model**

In Figure 5-8,  $T_1$ ,  $T_2$ ,  $T_3$  and  $T_4$  are the temperature sensor positions. The temperature difference between one pair of temperature sensors, ( $T_1$  and  $T_2$ ), has been monitored for two rotation and non-rotation cases. These results are summarized in , where  $\theta$  is considered to be a variable and  $\omega = 20$  rad/s.



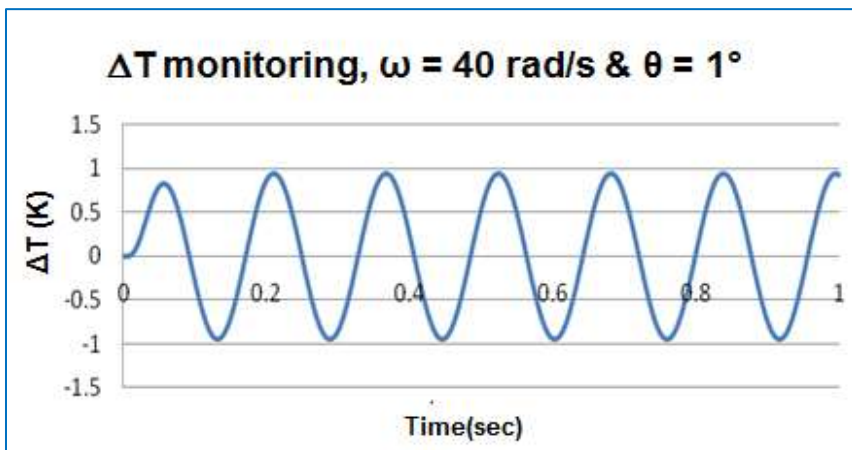
**Table 5 Simulation results of different rotation cases**

Angle \ Model	Rotation case, $\omega = 20 \text{ rad/s}$ $\Delta T(K)$	Not-Rotation case, $\omega = 0 \text{ rad/s}$ $\Delta T(K)$
$\theta = 1^\circ$		
$\theta = 2^\circ$		
$\theta = 30^\circ$		
$\theta = 45^\circ$		
$\theta = 60^\circ$		
$\theta = 90^\circ$		

According to the amplitude of the signal for the non-rotation case is negligible, however, the detected signal in rotation case is significant, and we can draw the conclusion that when the device is placed at an angle and is not rotating, the observed signal will be zero.

All Figures in column two of show that, as the device rotates, the convection current rising from the heater sweeps around the cavity, crossing the positions of the two temperature sensors alternately. The amplitude of the differential signal is proportional to the component of gravity in the plane of the temperature sensors,  $g \sin(\theta)$ .

Further simulations show that the frequency of the differential signal is synchronous with the angular rate of the rotation, Figure 5-9.



**Figure 5-9 Simulation results of Thermal Gyroscope in the rotation case,  $\omega = 40 \text{ rad/s}$ , and  $\theta = 1^\circ$**

We can conclude that frequency of the signal gives us information about the angular rate, while the amplitude of the signal gives us information about the angle between acceleration vector and rotation axis.

### **5.3. Conclusion**

In the first part of this study it has been shown that with the Single Heater Thermal Gyroscope it is possible to detect rotation along all three axes,  $x$ ,  $y$ ,  $z$ . This new design in comparison with previously designed Thermal gyroscope shows more capability for monitoring rotation since the previous design of Thermal gyroscope just has the ability to detect rotation about a single axis.

In the second part of this study we showed that with Single Heater Gyroscope it is possible to eliminate the impact of acceleration signal as this interference was previously the big disadvantage of Thermal MEMS Gyroscope.

To sum up, "One Heater Thermal Gyroscope" appears to have advantages in comparison with existing Thermal MEMS gyroscope

### **5.4. Future Work**

As future work we hope to work on MEMS fabrication processes to fabricate our designed MEMS gyroscope so that we could test this new model of gyroscope experimentally.

## 6. Conclusion and Future Work

Finite-element models of the Thermal MEMS gyroscope have been studied to optimize gyroscope performance. The effects of heater switching frequency, gas properties such as viscosity and density, and heater power on gyroscope sensitivity have been investigated. We have shown that by using a denser gas inside the cavity, it is possible to increase the gyroscope sensitivity up to a certain point, after which the sensitivity will decline. In order to compensate for this decline we studied the impact of heater switching frequency and showed that the loss of sensitivity by using a very dense gas could be compensated for by decreasing the heater switching frequency. We also investigated the impact of gas viscosity and showed that sensitivity will decrease by using a more viscous fluid. These results could be used as a guide to optimization of gyroscope sensitivity as a function of device pressure, heater power, heater switching frequency, and properties of the working gas. These conclusions were summed up by the introduction of the Ekman number as a single dimensionless parameter affecting sensitivity.

The thermal MEMS gyroscope shows low SIR with respect to the spurious signal produced by accelerations, including gravity. A new dimensionless parameter, the 'gyrointerference number', was introduced to summarise the parameters affecting SIR. We introduced a new Thermal MEMS gyroscope model referred to as "Forced Convection MEMS Gyroscope". In this design the output signal is increased by adding external force to the system. This force was generated by an external pump in our experimental systems. We also investigated signal-processing techniques to extract the rotation signal and eliminate the impact of acceleration signal. Our promising COMSOL simulation results encouraged us to consider building a rotary platform to rotate our experimental setup as future work. We are looking forward to comparing experimental results with our COMSOL simulation studies.

Further design improvements resulted in the last model, referred to as "Three-axis MEMS gyroscope": the two heaters in the previous designs were merged into one cross-shaped heater located in the middle of the cavity. We built a three-dimensional COMSOL model of this design. Simulation results of this study were promising and we showed it is possible to extract rotation signal if the impact of acceleration signal is disregarded. Initial two-dimensional studies

suggested that even in the presence of acceleration, rotations could be resolved and measured by tracing the natural convection flows. The possibility of eliminating acceleration impact on the rotation signal with this design needs more investigation and is among our future studies.

## References

- [1] A. Burg, "MEMS Gyroscopes and Their Applications," Northwestern University, <http://clifton.mech.northwestern.edu/~me381/project/done/Gyroscope.pdf>, (accessed 2013, January 9)
- [2] M. Armenise, C. Ciminelli, F. Olio, and V. Passaro, "Advances in Gyroscope Technologies," first edition, ISBN 978-3-642-15493-5, Springer Berlin Heidelberg, 2011.
- [3] W. Wrigley and W. Hollister, "The Gyroscope Theory and Application," Science, Vol. 149, No. 3685, pp. 713-721, Aug. 1965.
- [4] [http://solarsystem.nasa.gov/scitech/display.cfm?ST\\_ID=327](http://solarsystem.nasa.gov/scitech/display.cfm?ST_ID=327) (accessed 2013, January 26)
- [5] Wikipedia, <http://en.wikipedia.org/wiki/Gyroscope>, Wikipedia (accessed 2013, January 9)
- [6] C. Acar, and A. Shkel, "MEMS Vibratory Gyroscopes: Structural Approaches to Improve Robustness," Springer US, 2009.
- [7] D. Rozelle, "Hemispherical Resonator Gyroscope", Sr. Research Scientist, Northrop Grumman Co, Navigation Systems Division, 21240 CA, US, [http://usdynamicscorp.com/literature/precision\\_instruments/AN-005%20USD%20Spinning%20Mass%20Gyroscopes.pdf](http://usdynamicscorp.com/literature/precision_instruments/AN-005%20USD%20Spinning%20Mass%20Gyroscopes.pdf) (accessed 2013, January 9).
- [8] E.Post, "Sagnac Effect," Review of Modern Physics, Vol.36, No.2, Air Force Cambridge Research Laboratories, Bedford, Massachusetts, 1967.
- [9] J. Fraden, "Handbook of Modern Sensors Physics Designs and Applications," Third edition, San Diego, CA, USA, Springer, 2004.
- [10] P. Greiff, B. Boxenhorn, T. King, and L. Niles, "Silicon monolithic micromechanical gyroscope," International Conference on Solid-State Sensors and Actuators, San Francisco, CA, US, 1991.
- [11] T. Adams and R. Layton, "Introductory MEMS: Fabrication and Applications" ISBN: 978-0-387-09510-3, Springer US 2010.
- [12] N. Yazdi, F. Ayazi, and K. Najafi, "Micromachined Inertial Sensors," Proceedings of the IEEE, Vol.86, No.8, pp.1640-1659, Aug. 1998.

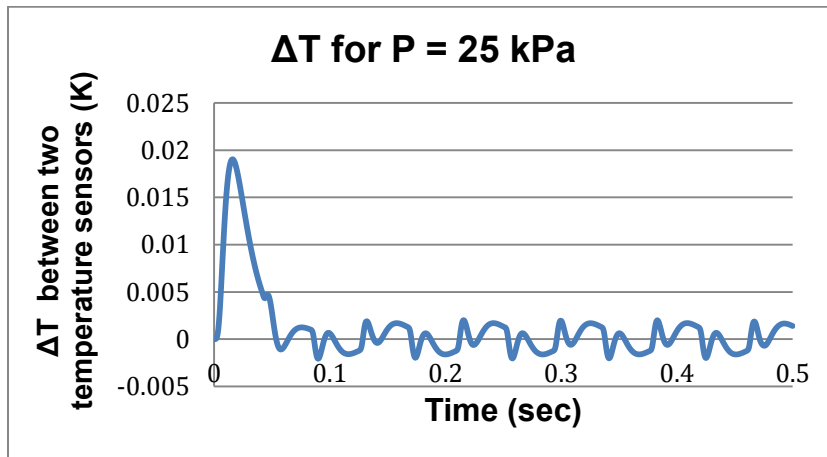
- [13] S. Nasiri, "A Critical Review of MEMS Gyroscopes Technology and Commercialization Status," 3150A Coronado Drive, Santa Clara, California, US
- [14] C. Acar, "Robust Micromachined Vibratory Gyroscopes," PhD Thesis dissertation, UC Irvine, CA, US, 2004.
- [15] B. Zhang and F. Zhang, "Analysis of Piezoelectric Fluidic Gyroscope Sensitive Mechanism", IEEE International Conference, China, June 2005.
- [16] G. Piazza and P. Stephanou, "Micromechanical Thermo-fluidic Single-axis Yaw Rate Sensor," University of California Berkeley, 2004.
- [17] V. Dau, O. Tomonori, T. Dinh, D. Dao, and S. Sugiyama, "A Multi-Axis Fluidic Inertial Sensor," IEEE Sensors, Italy, 2008.
- [18] T. Dinh and Y. Ogami, "Design and simulation of MEMS-based dual-axis fluidic angular velocity sensor," Science Direct, Sensors and Actuators, Volume 189, 15 January 2013, Pages 61–66
- [19] A. Leung, "A Low-Cost Thermal MEMS Gyroscope," Hilton Head Workshop 2010: A Solid-State Sensors, Actuators and Microsystems Workshop, pp. 364-367, Hilton Head Island, South Carolina, US, June 2010.
- [20] R. Zhu, H. Ding, Y. Su, and Z. Zhou, "Micromachined Gas Inertial Sensor Based on Convection Heat Transfer," Science Direct, Sensors and Actuators, pp. 68–74, 2006.
- [21] A. Leung, "Micromachined Accelerometer Based on Convection Heat Transfer," MEMS 98, pp. 627-630, Italy, January 1998.
- [22] N. Zarei, A. Leung, and J. Jones, "Design and Analysis of a Micromachined Gyroscope," Vol. 8251, 82510 X, SPIE Conference, San Francisco, CA, US, Jan 2012.
- [23] Y. Zhang, "A Micromachined Coriolis-force-based Gyroscope for Direct Flow and Fluid Density Measurement," Transducers' 01, June 2001.
- [24] C. Desai and J. Abel, "Introduction to the Finite Element Method: A Numerical Method for Engineering Analysis" ISBN 10: 0442220839 New York 1971.
- [25] Boussinesq, J., 'Théorie de l'écoulement tourbillonnant et tumultueux des liquides dans les lits rectilignes a grande section , Vol.1, pp899-902., Washington D.C., US Dec., 1997.
- [26] S. Vosloo, "Analytical Modelling and Optimization of a Thermal Convective Microfluidic Gyroscope," University of Stellenbosch, M.Sc thesis, 2010.
- [27] <http://www.comsol.com/products/multiphysics>, COMSOL Software. (accessed 2013, January 9)
- [28] P. Shooshtari, A. Leung and J. Jones, "Suppression of Spurious Signals in Thermal MEMS Gyroscope," IEEE Sensors Conference, Taipei, Taiwan, 2012.

- [29] V. Thanhha, D. Dao, T. Shiozawa, H. Kumagai and S. Sugiyama, "A Single-Axis Thermal Convective Gas Gyroscope," *Sensors and Materials*, Vol. 17, No. 8, Japan, Jan. 2005.
- [30] T. Shiozawa, V. T. Dau, D. Kumagai and, and S. Sugiyama, "A Dual-Axis Thermal Convective Silicon Gyroscope," *Micro-Nanomechatronics and Human Science Conference*, Japan, 2004.
- [31] D. Dao, V. Dau, T. Shiozawa, and S. Sugiyama, "Development of a Dual-Axis Convective Gyroscope with Low Thermal-Induced Stress Sensing Element," *Microelectromechanical Systems Journal*, Vol. 16, No. 4, Aug 2007.
- [32] V. Daul, T. Dinh, and D. Dao, "Design and Simulation of Convective Inertial Sensor," *Micro-NanoMechatronics and Human Science Conference*, Japan, 2008.
- [33] V. Thanhha, D. Dao, T. Shiozawa, H. Kumagai and S. Sugiyama, "Design and Fabrication of a Convective 3-DOF Angular Rate Sensor," *IEEE Sensors Conference*, Atlanta, US, 2007
- [34] V. Daul, T. Dinh, and D. Dao, "Design and Simulation of Convective Inertial Sensor," *Micro-NanoMechatronics and Human Science Conference*, Japan, 2008.
- [35] N. Zarei, A. Leung, and J. Jones, "Modeling a Novel MEMS Gyroscope," *The Society for Solid-State and Electrochemical Science and Technology Conference*, Seattle, US, May 2012.

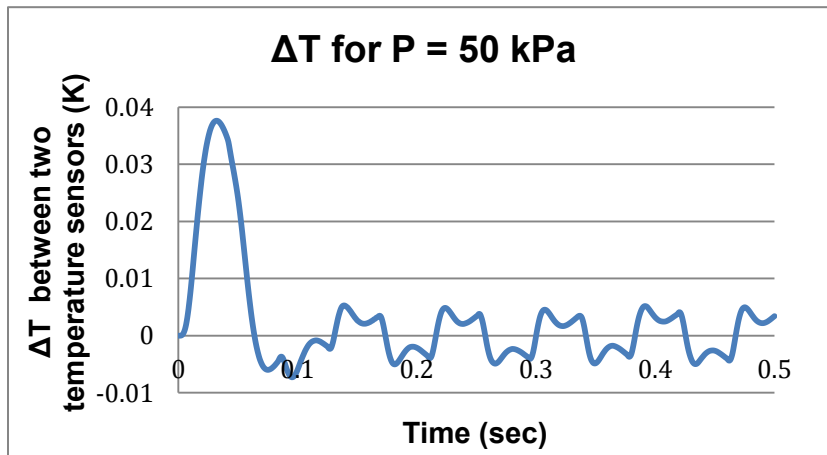




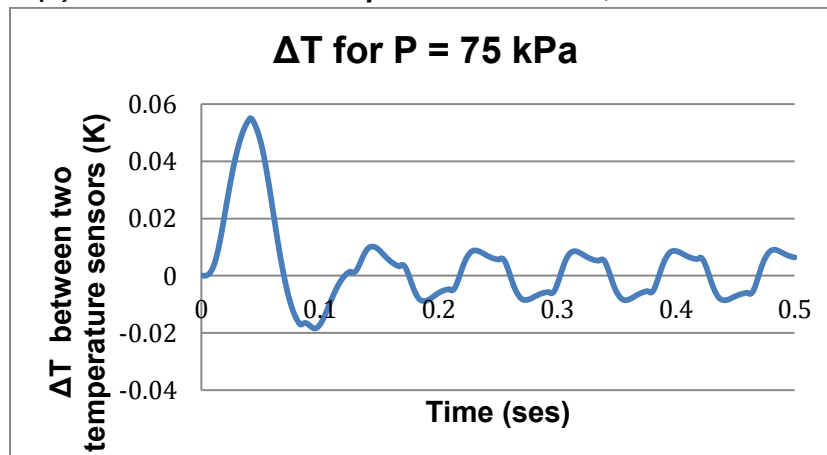
## Appendix



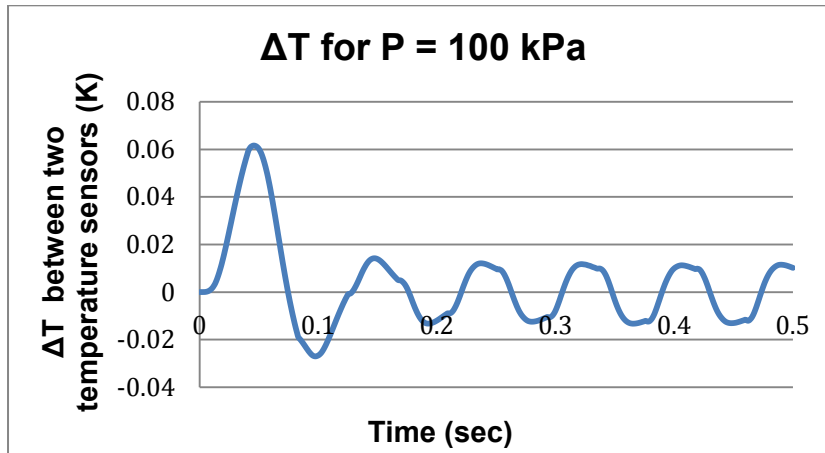
(a)  $\Delta T$  between two temperature sensors,  $P = 25 \text{ kPa}$



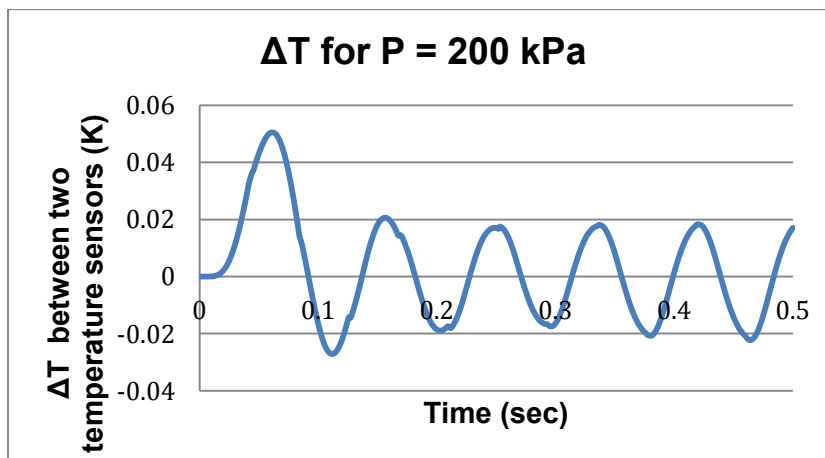
(b)  $\Delta T$  between two temperature sensors,  $P = 50 \text{ kPa}$



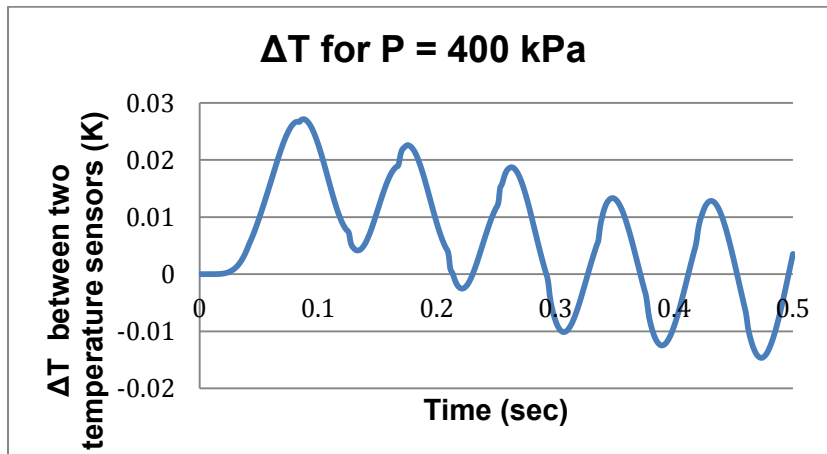
**(c)  $\Delta T$  between two temperature sensors,  $P = 75 \text{ kPa}$**



**(d)  $\Delta T$  between two temperature sensors,  $P = 100 \text{ kPa}$**

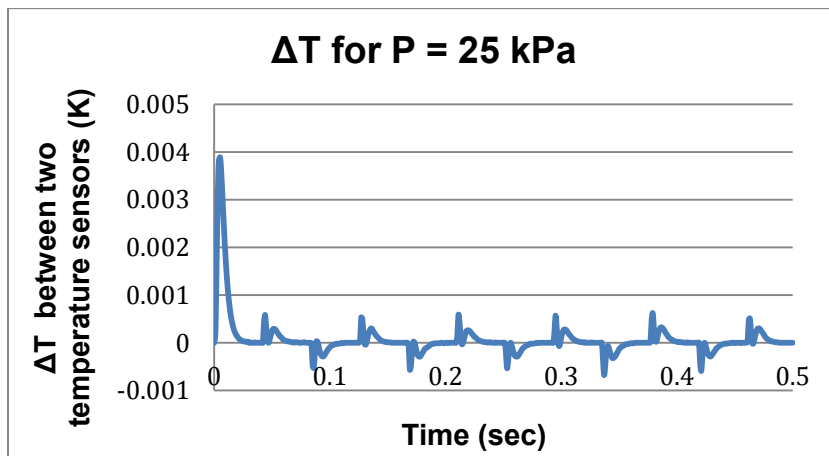


**(e)  $\Delta T$  between two temperature sensors,  $P = 200 \text{ kPa}$**

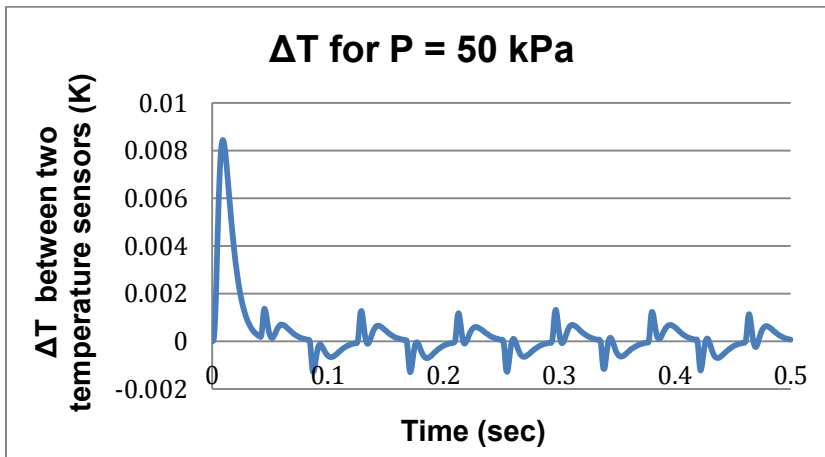


(f)  $\Delta T$  between two temperature sensors,  $P = 400$  kPa

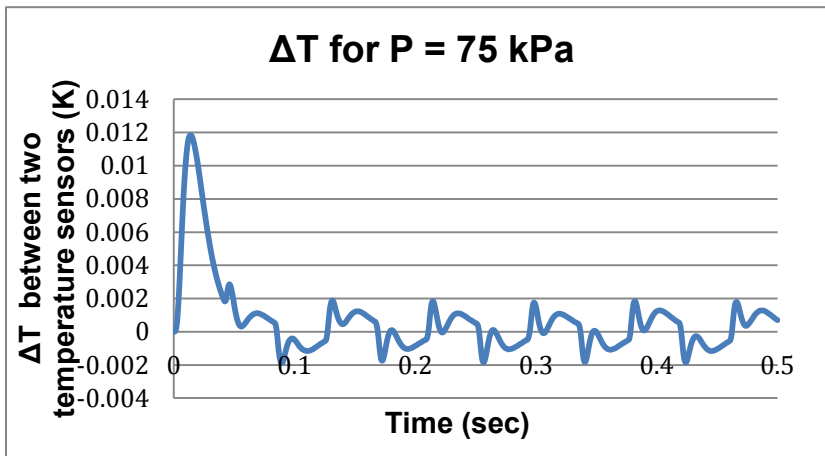
Figure 1-A  $\Delta T$  plot between two temperature sensors, by varying pressure. Cavity filled with  $SF_6$  and angular rate is 1rad/sec.



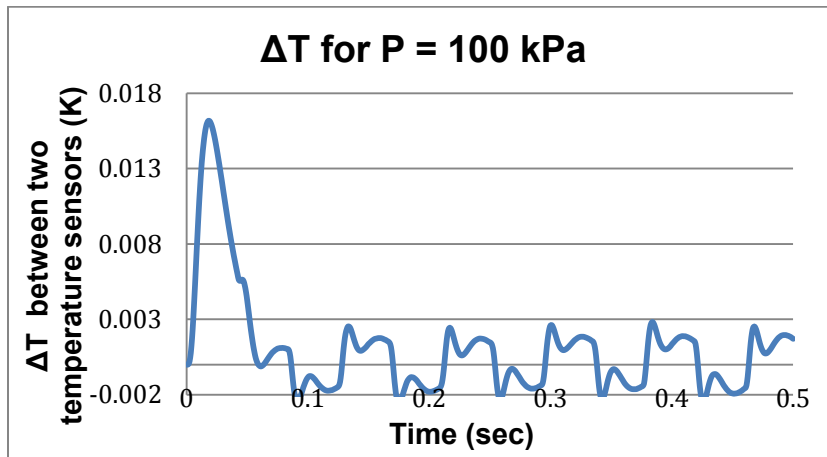
(a)  $\Delta T$  between two temperature sensors,  $P = 25$  kPa



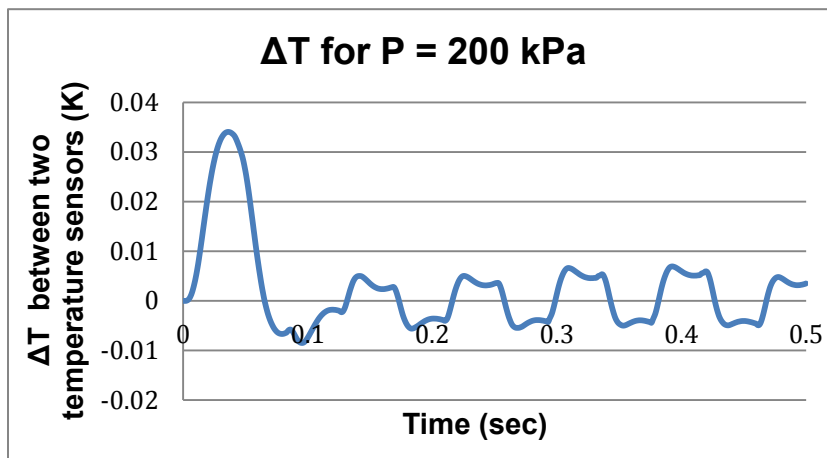
*(b) ΔT between two temperature sensors, P = 50 kPa*



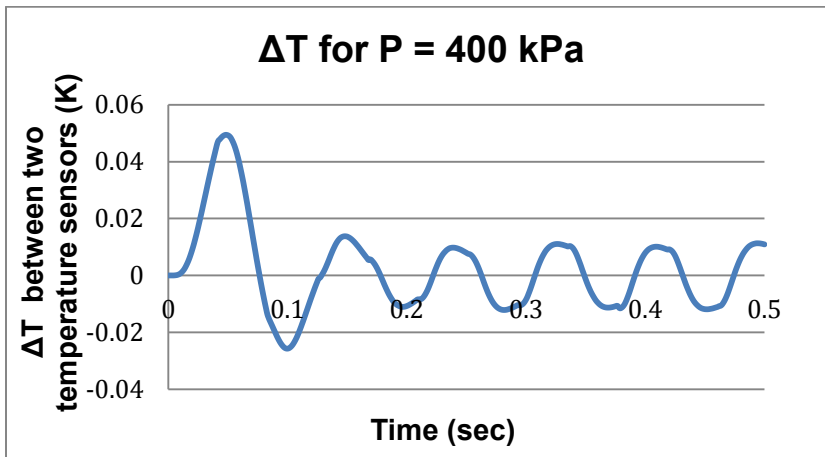
*(c) ΔT between two temperature sensors, P = 75 kPa*



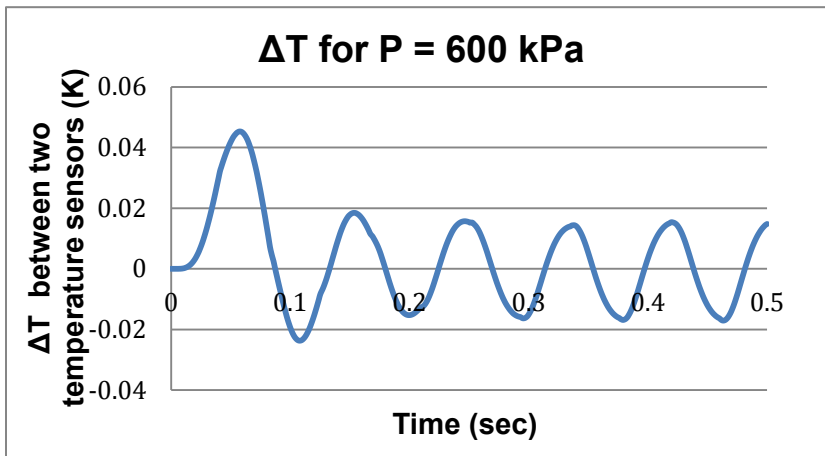
**(d)  $\Delta T$  between two temperature sensors,  $P = 100$  kPa**



**(e)  $\Delta T$  between two temperature sensors,  $P = 200$  kPa**

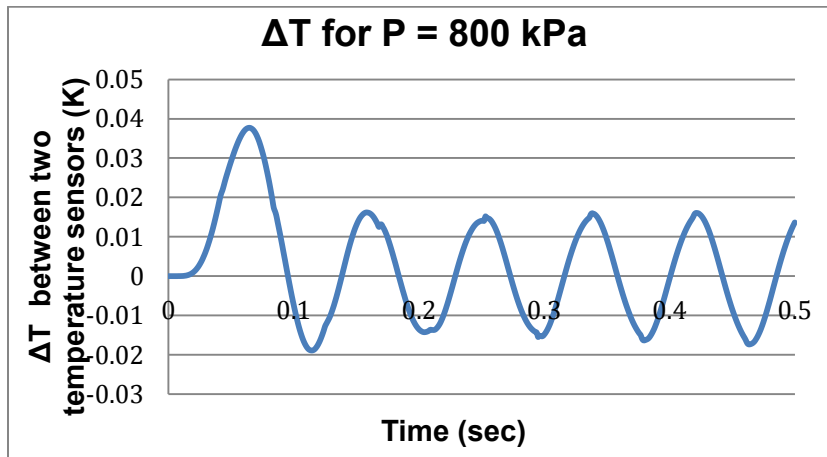


*(f) ΔT between two temperature sensors, P = 400 kPa*



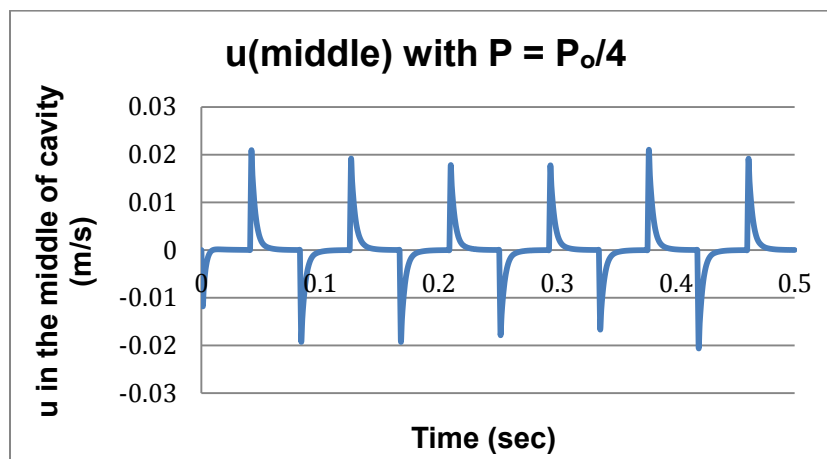
*(g) ΔT between two temperature sensors, P = 600 kPa*



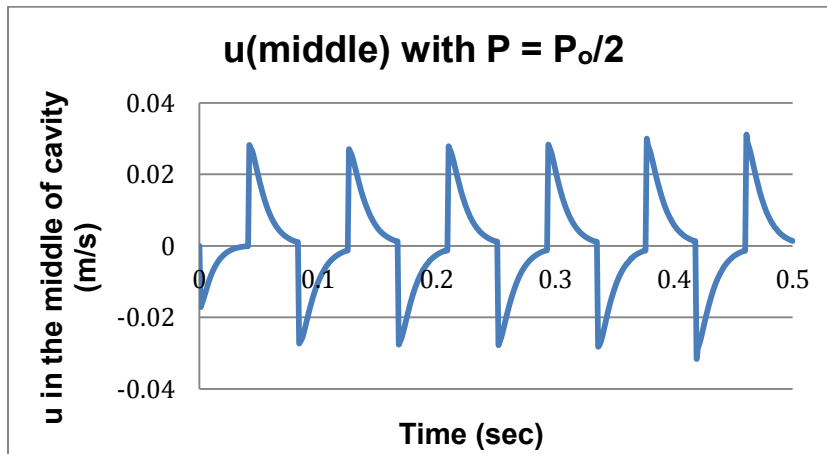


(h)  $\Delta T$  between two temperature sensors,  $P = 800$  kPa

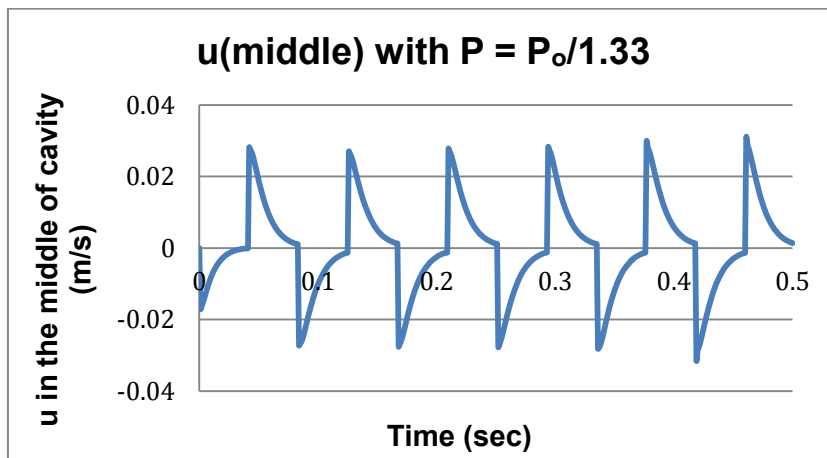
Figure 2-A  $\Delta T$  plot between two temperature sensors, by varying pressure. Cavity filled with air and angular rate is 1rad/sec.



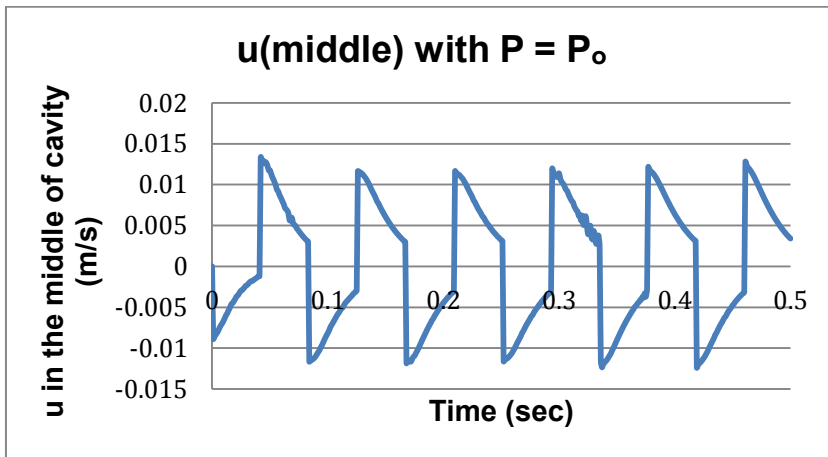
(a)  $u$  in the middle of cavity, pressure = pressure<sub>0</sub>/4



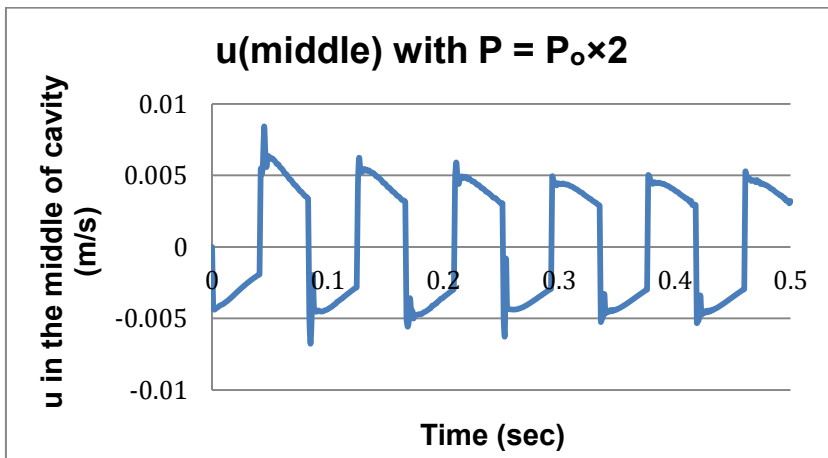
*(b)  $u$  in the middle of cavity, pressure = pressure<sub>o</sub>/2*



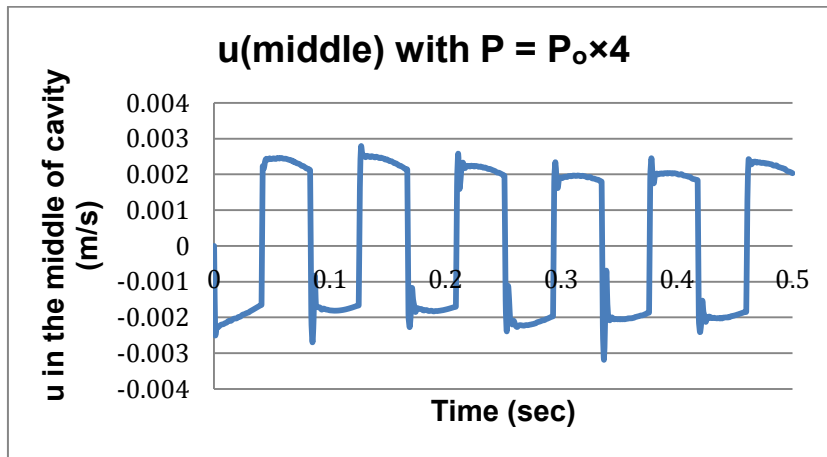
*(c)  $u$  in the middle of cavity, pressure = pressure<sub>o</sub>/1.33*



**(d)  $u$  in the middle of cavity, pressure = pressure<sub>0</sub>**

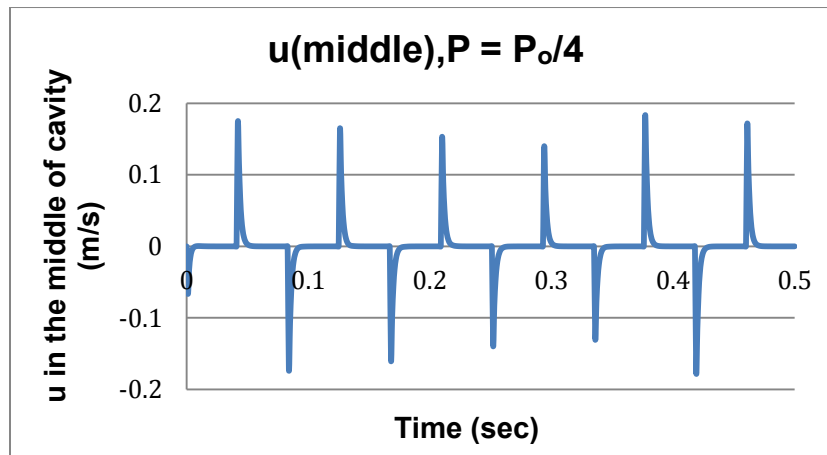


**(e)  $u$  in the middle of cavity, pressure = pressure<sub>0</sub> × 2**

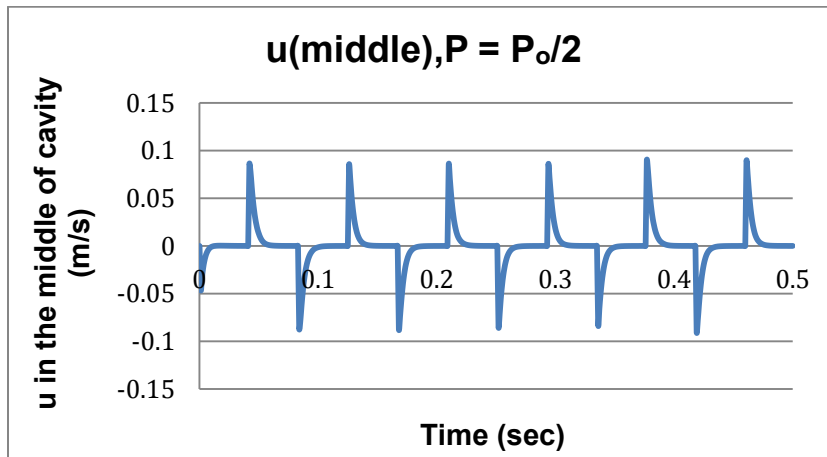


**(f)  $u$  in the middle of cavity, pressure = pressure<sub>0</sub> × 4**

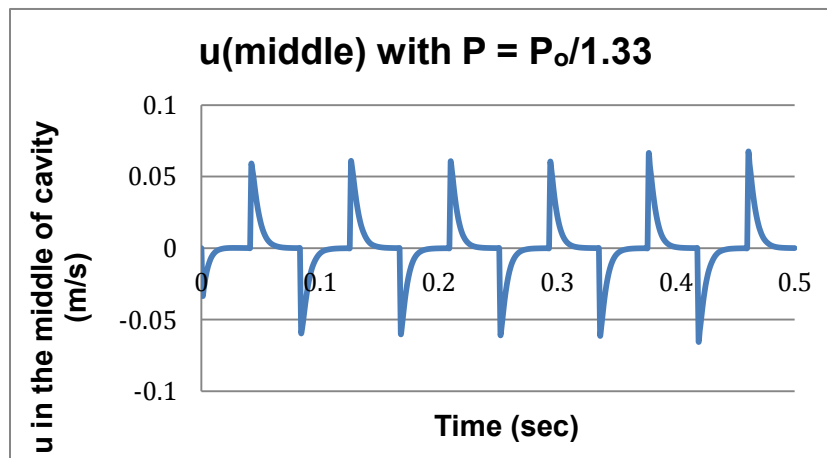
**Figure 3-A Monitoring  $u$  in the middle of cavity by varying pressure. Cavity filled with  $SF_6$ , and angular rate is 1rad/sec.**



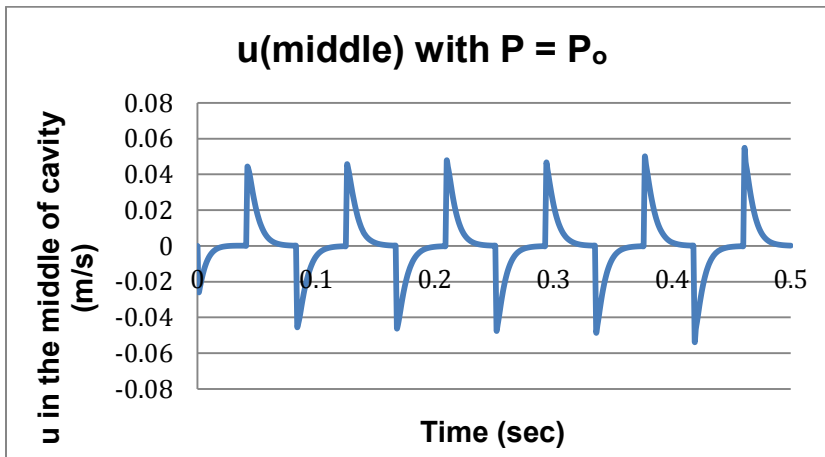
**(a)  $u$  in the middle of cavity, pressure = pressure<sub>0</sub> / 4**



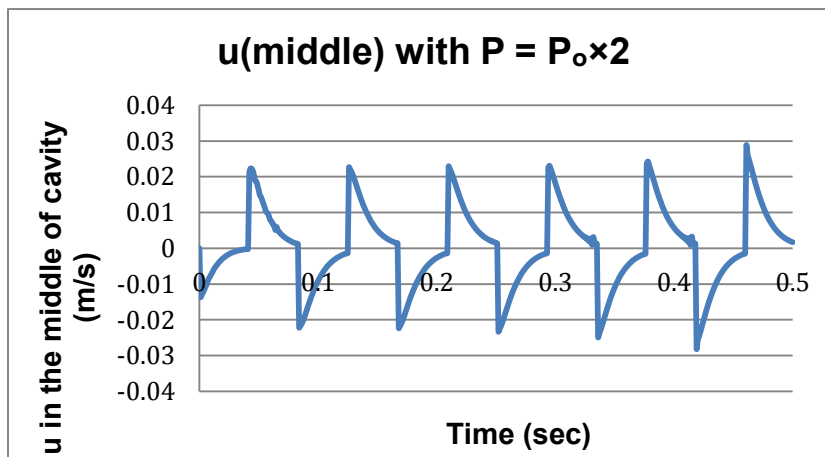
*(b) u in the middle of cavity, pressure = pressure<sub>o</sub>/2*



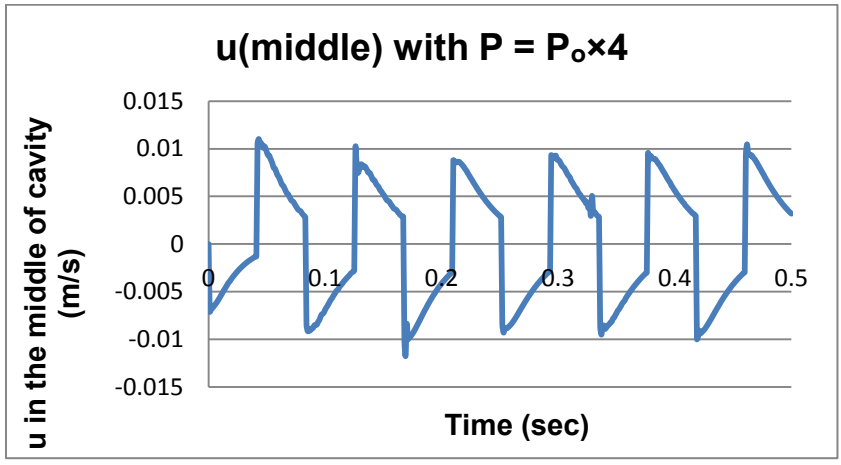
*(c) u in the middle of cavity, pressure = pressure<sub>o</sub>/1.33*



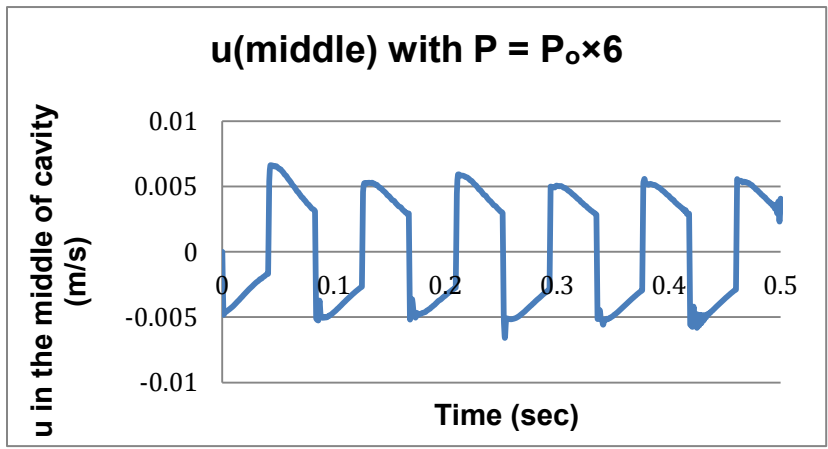
**(d)  $u$  in the middle of cavity, pressure = pressure<sub>0</sub>**



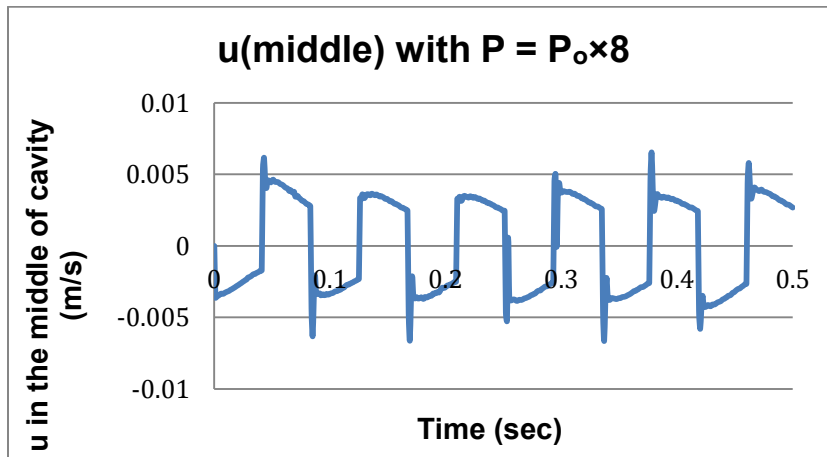
**(e)  $u$  in the middle of cavity, pressure = pressure<sub>0</sub> × 2**



**(f)  $u$  in the middle of cavity, pressure = pressure<sub>0</sub> × 4**

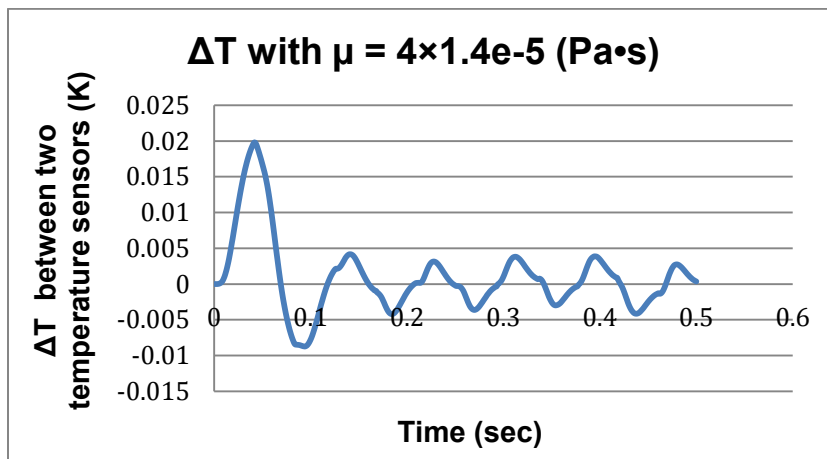


**(g)  $u$  in the middle of cavity, pressure = pressure<sub>0</sub> × 6**



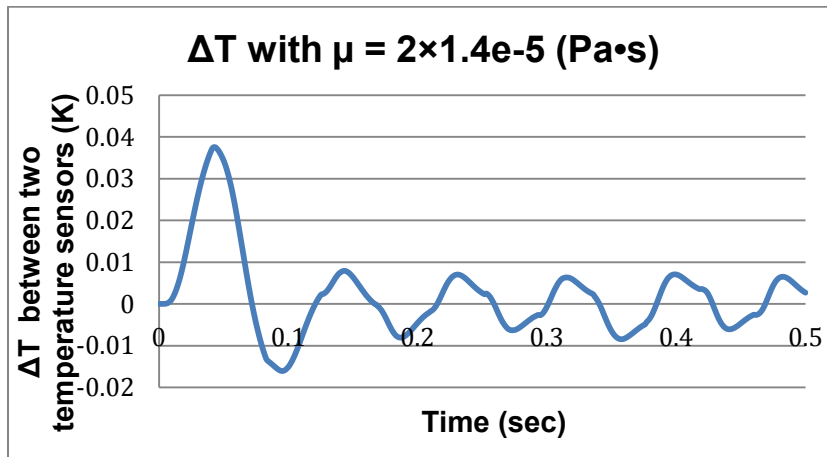
(h)  $u$  in the middle of cavity, pressure = pressure<sub>0</sub> × 8

Figure 4-A Monitoring  $u$  in the middle of cavity by varying pressure. Cavity filled with SF<sub>6</sub>, and angular rate is 1rad/sec.

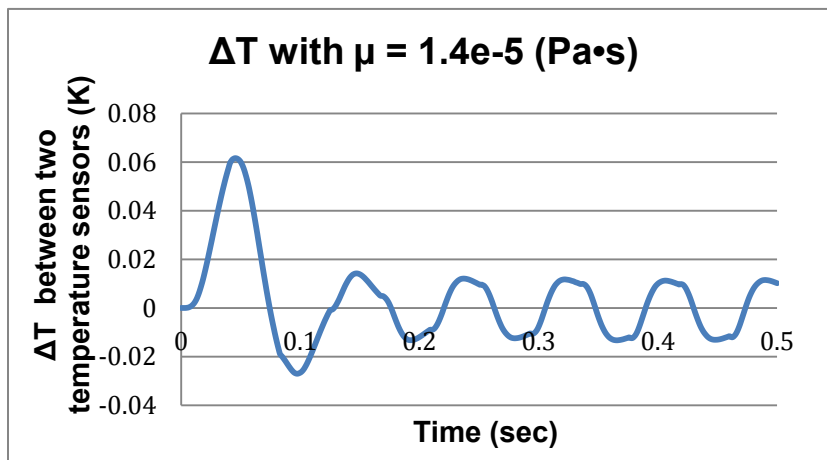


(a)  $\Delta T$  plot between two temperature sensors,  $\mu = 4 \times 1.4e-5$  (Pa·s)

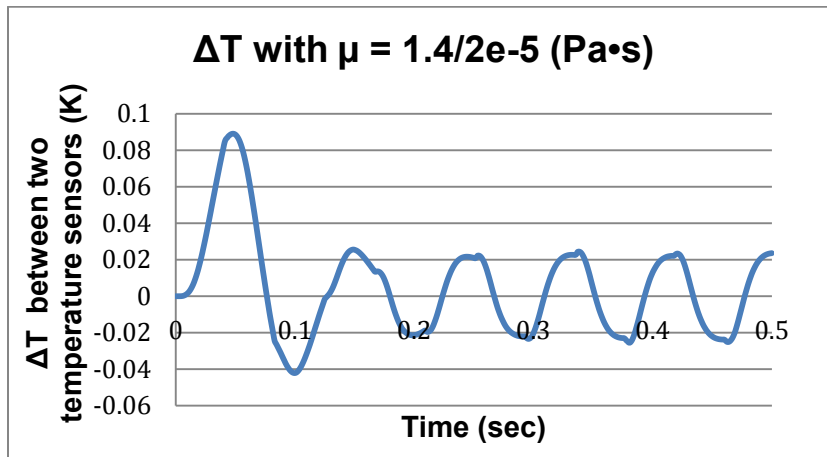




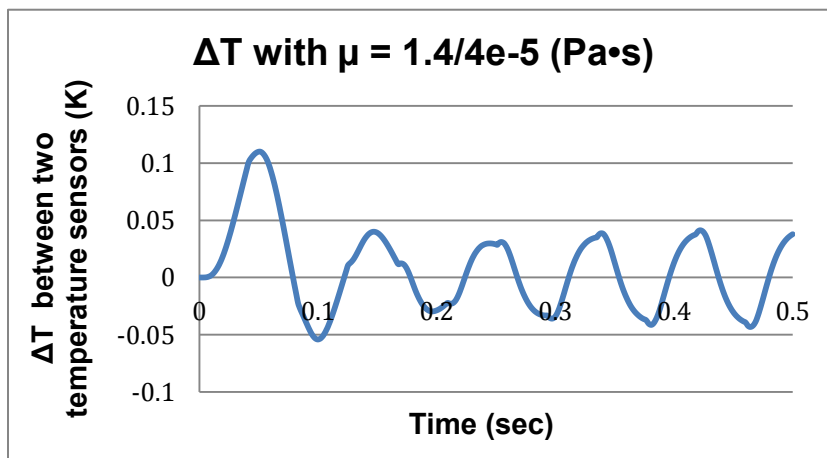
(b)  $\Delta T$  plot between two temperature sensors,  $\mu = 2 \times 1.4e-5$  (Pa·s)



(c)  $\Delta T$  plot between two temperature sensors,  $\mu = 1.4e-5$  (Pa·s)

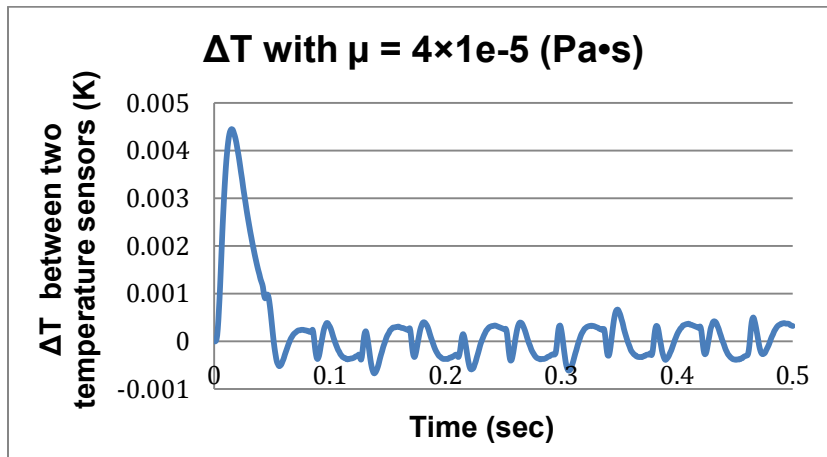


(d)  $\Delta T$  plot between two temperature sensors,  $\mu = 1.4/2e-5$  (Pa·s)

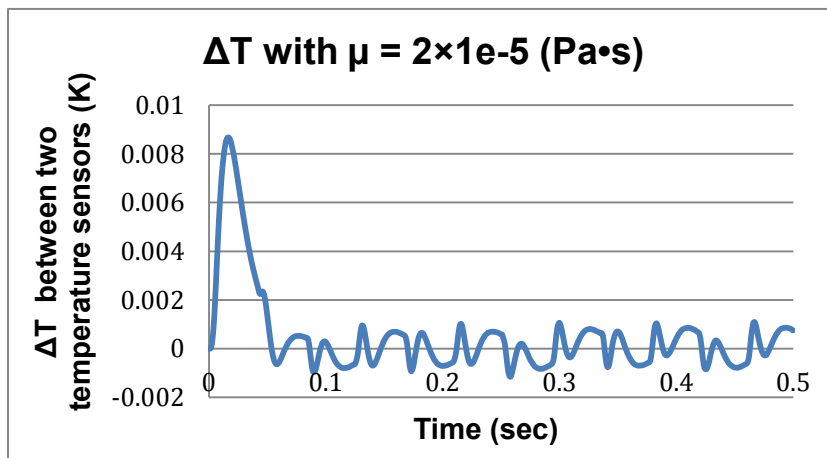


(e)  $\Delta T$  plot between two temperature sensors,  $\mu = 1.4/4e-5$  (Pa·s)

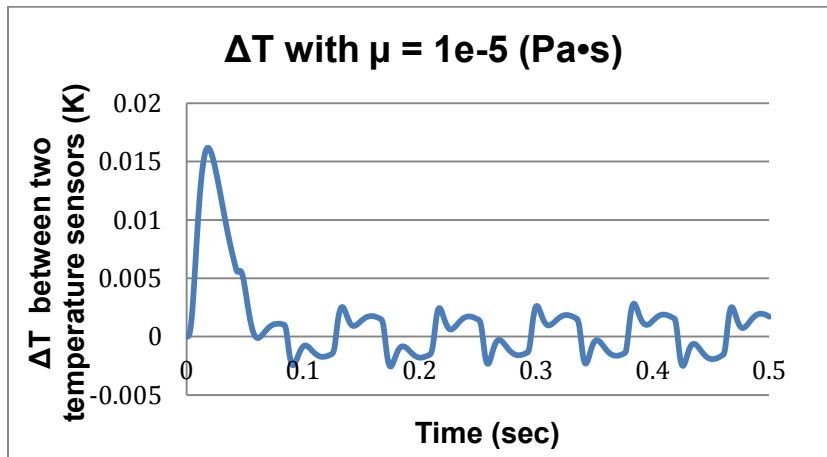
**Figure 5-A Temperature difference plot between two temperature sensors by varying Viscosity. Cavity filled with SF<sub>6</sub> and angular rate is 1rad/sec.**



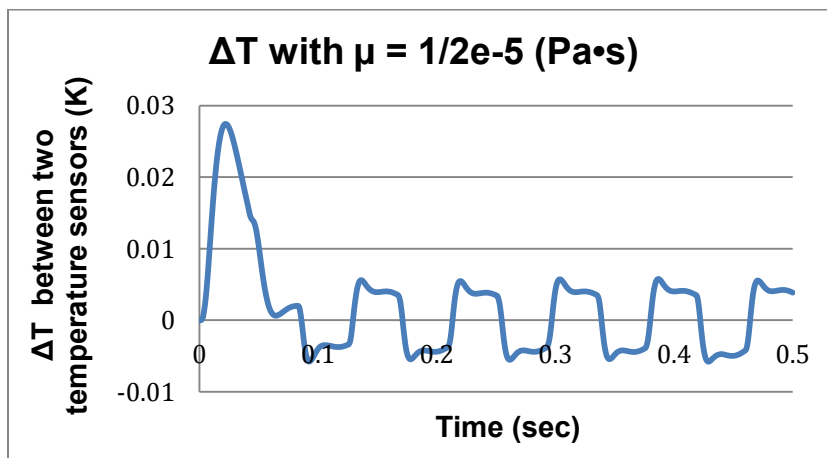
(a)  $\Delta T$  plot between two temperature sensors,  $\mu = 4 \times 10^{-5}$  (Pa·s)



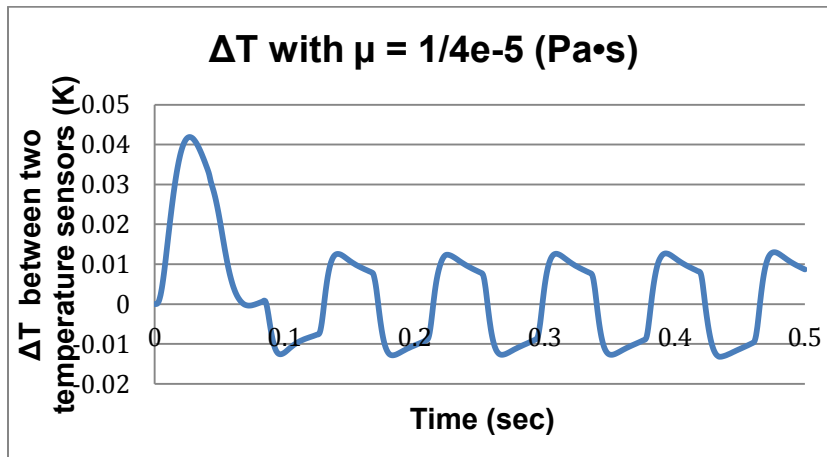
(b)  $\Delta T$  plot between two temperature sensors,  $\mu = 2 \times 10^{-5}$  (Pa·s)



(c)  $\Delta T$  plot between two temperature sensors,  $\mu = 1 \times e-5$  (Pa·s)

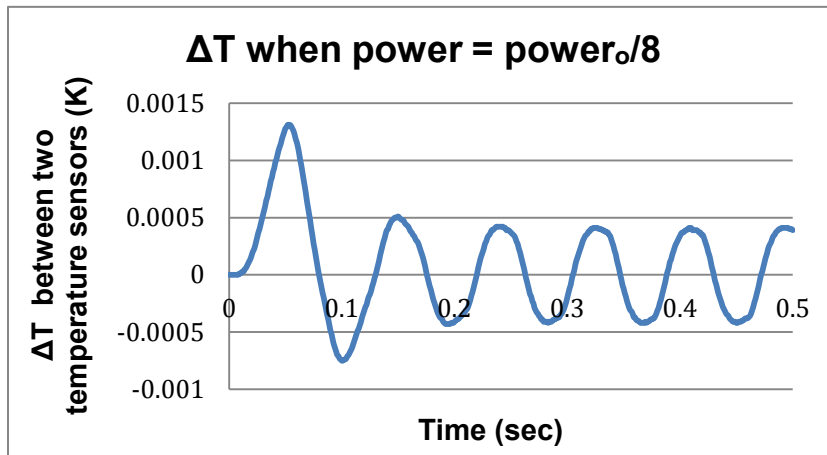


(d)  $\Delta T$  plot between two temperature sensors,  $\mu = 1/2 \times 1e-5$  (Pa·s)

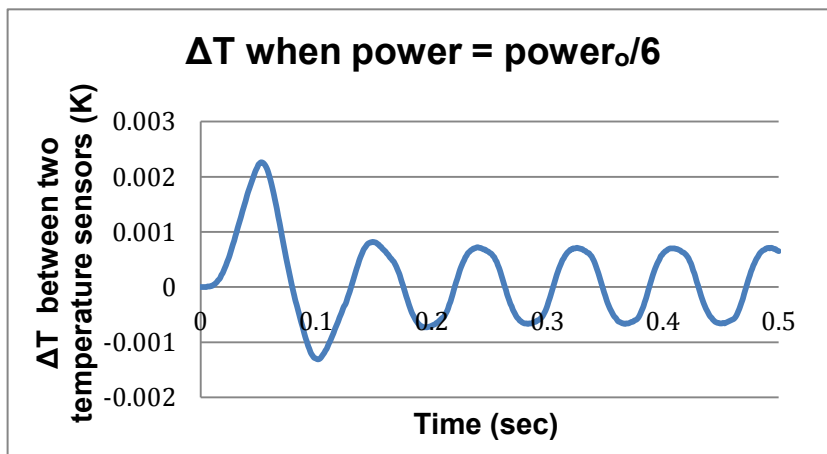


(e)  $\Delta T$  plot between two temperature sensors,  $\mu = 1/4 \times 10^{-5}$  (Pa·s)

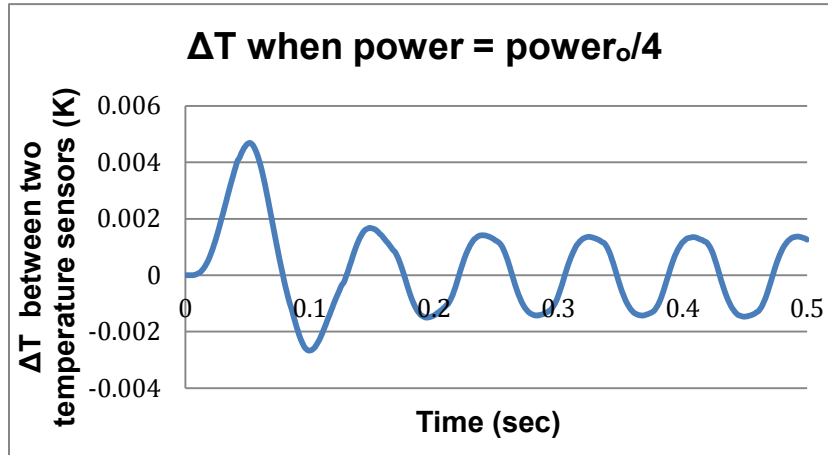
Figure 6-A Temperature difference plot between two temperature sensors by varying Viscosity. Cavity filled with air and angular rate is 1rad/sec.



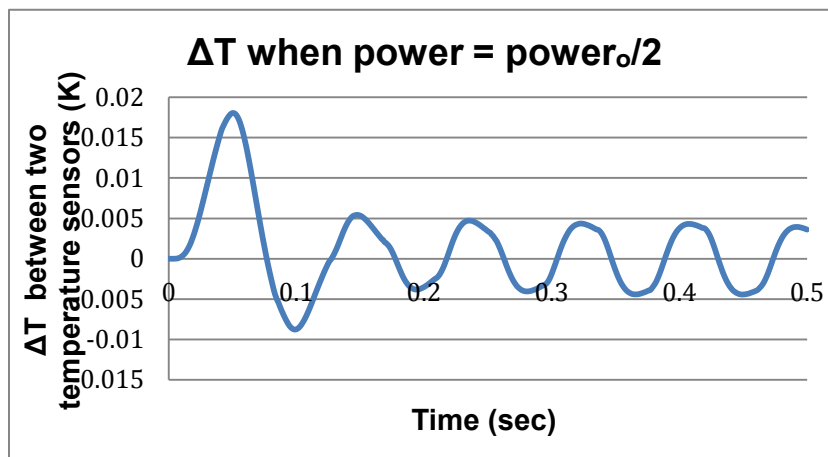
(a)  $\Delta T$  plot between two temperature sensors power = power<sub>0</sub> /8



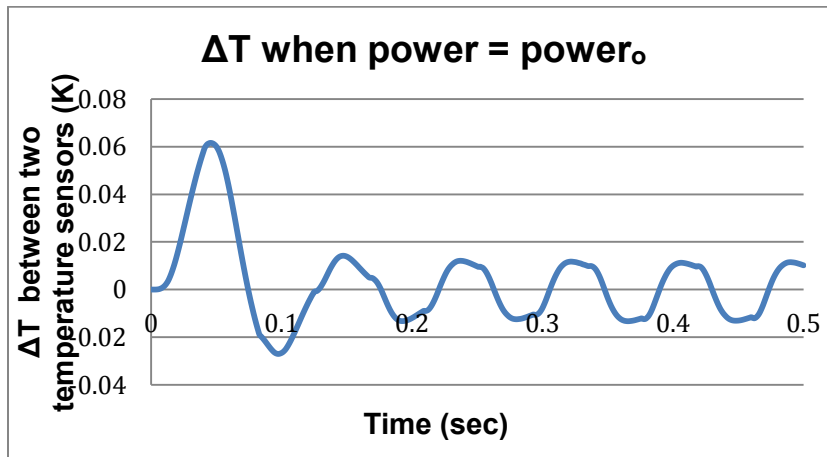
(b)  $\Delta T$  plot between two temperature sensors, power = power<sub>0</sub>/6



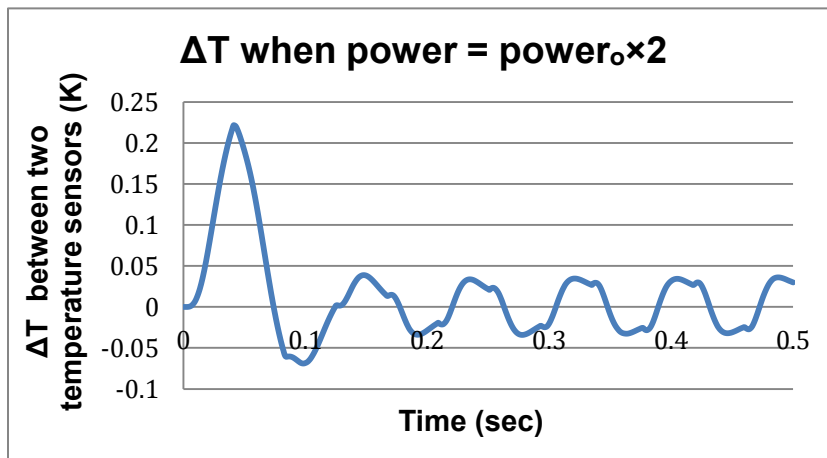
(c)  $\Delta T$  plot between two temperature sensors, power = power<sub>0</sub>/2



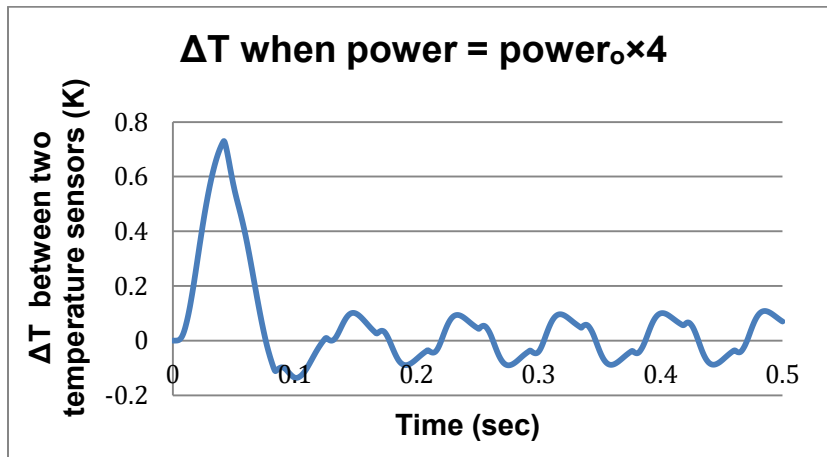
(d)  $\Delta T$  plot between two temperature sensors power = power<sub>0</sub>/2



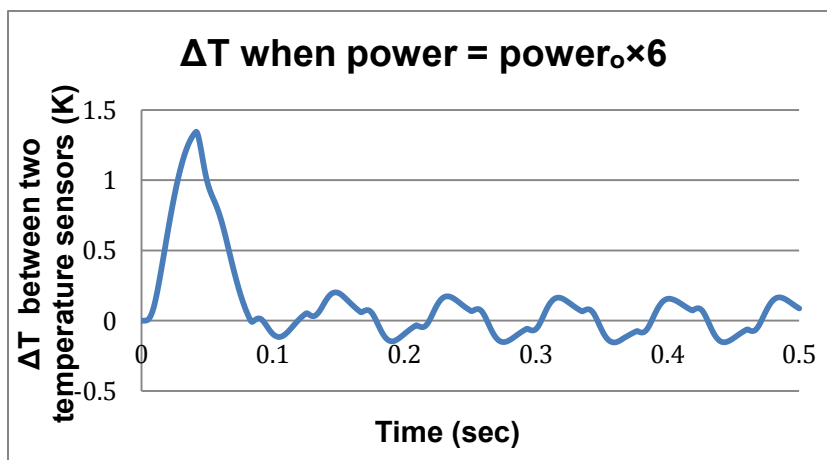
(e)  $\Delta T$  plot between two temperature sensors, power = power<sub>0</sub>



(f)  $\Delta T$  plot between two temperature sensors, power = power<sub>0</sub> × 2

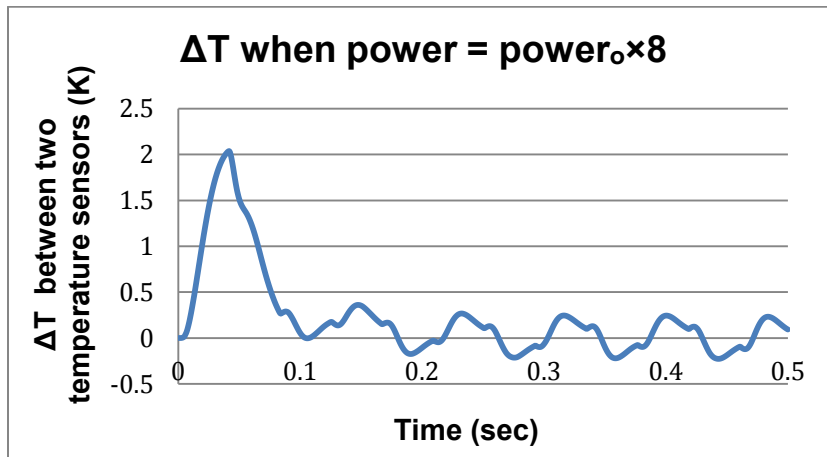


*(g) ΔT plot between two temperature sensors, power = power<sub>0</sub> ×4*



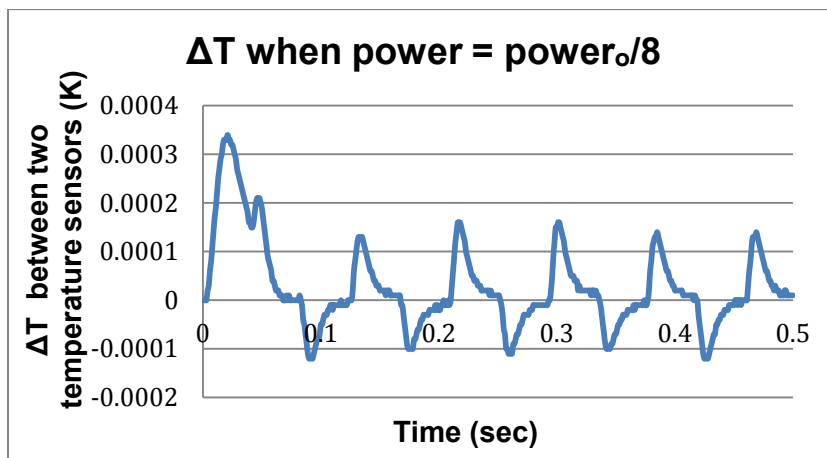
*(h) ΔT plot between two temperature sensors, power = power<sub>0</sub> ×6*



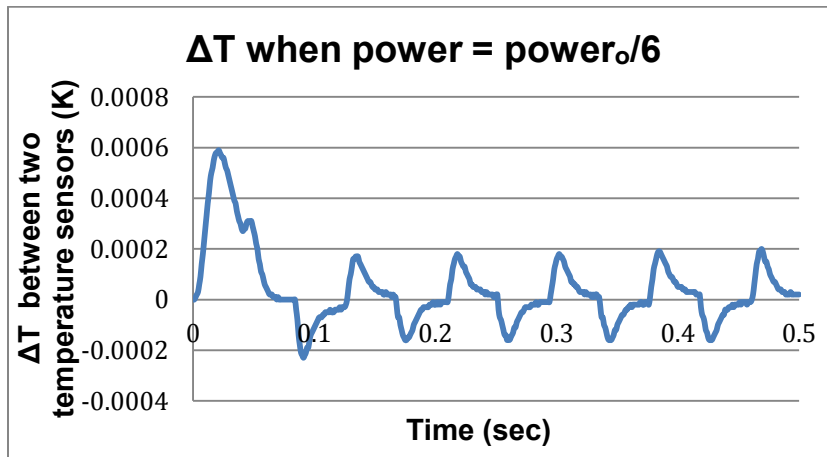


(i)  $\Delta T$  plot between two temperature sensors, power = power<sub>0</sub> × 8

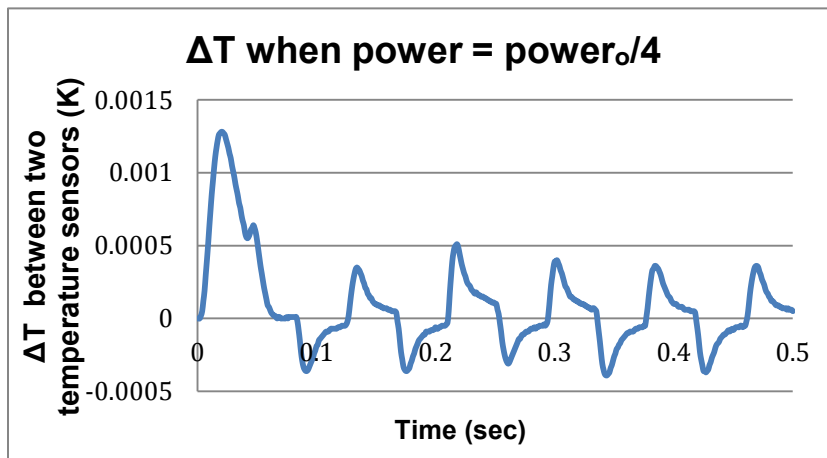
Figure 7-A  $\Delta T$  plot between two temperature sensors by varying power. Cavity filled with air and angular rate is 1 rad/sec.



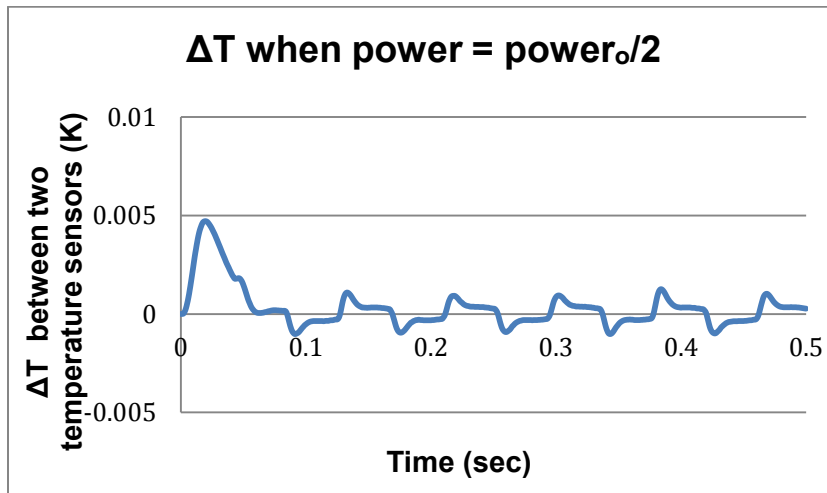
(a)  $\Delta T$  plot between two temperature sensors, power = power<sub>0</sub> / 8



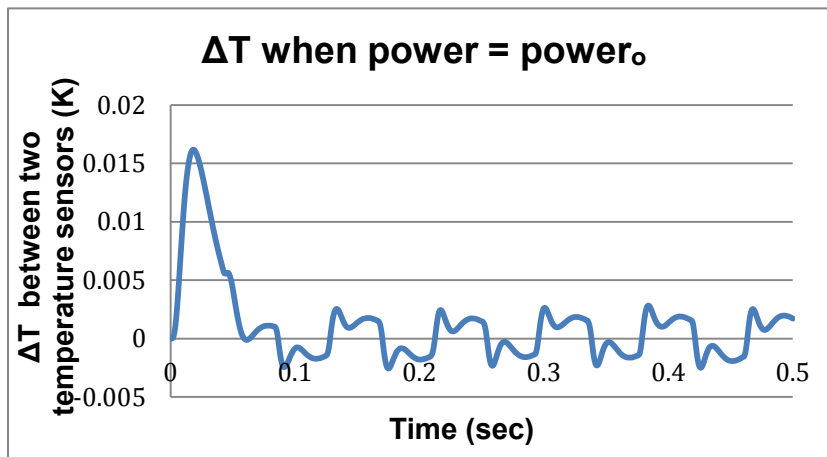
(b)  $\Delta T$  plot between two temperature sensors, power = power<sub>0</sub>/6



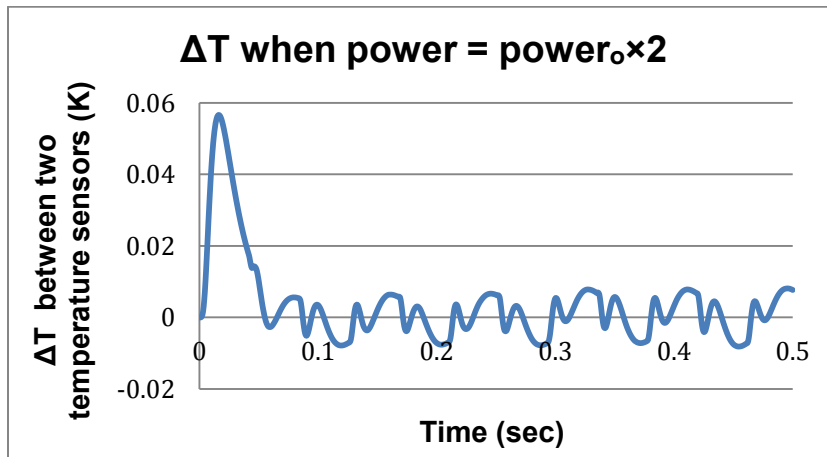
(c)  $\Delta T$  plot between two temperature sensors, power = power<sub>0</sub>/4



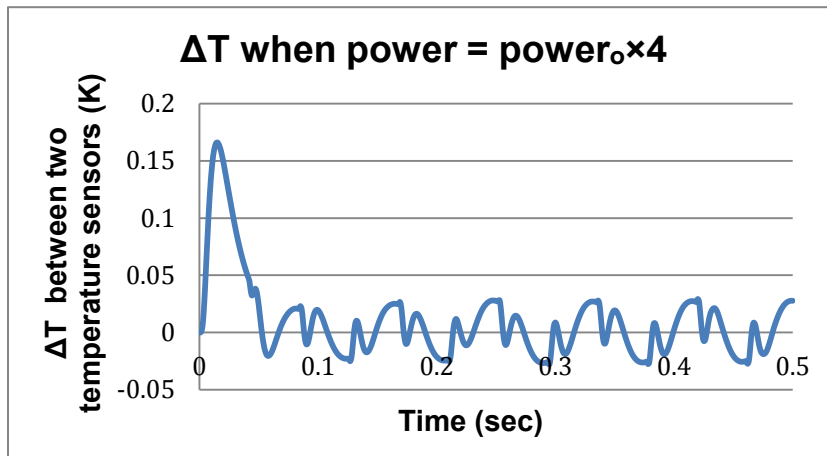
(d)  $\Delta T$  plot between two temperature sensors, power = power<sub>0</sub>/2



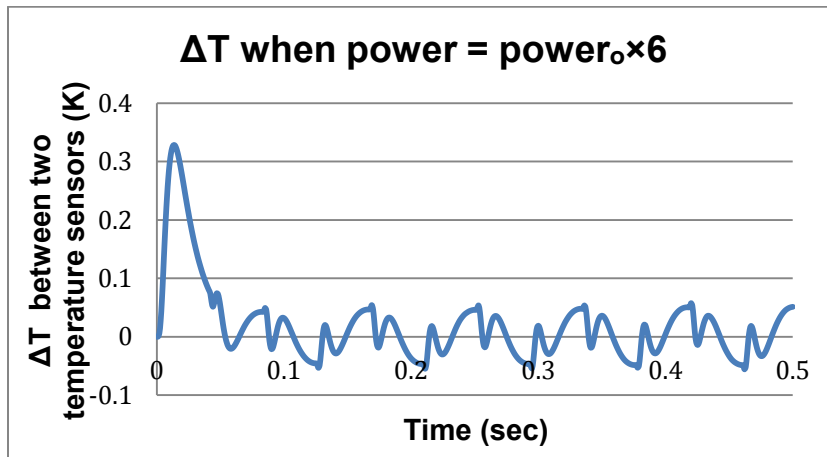
(e)  $\Delta T$  plot between two temperature sensors, power = power<sub>0</sub>



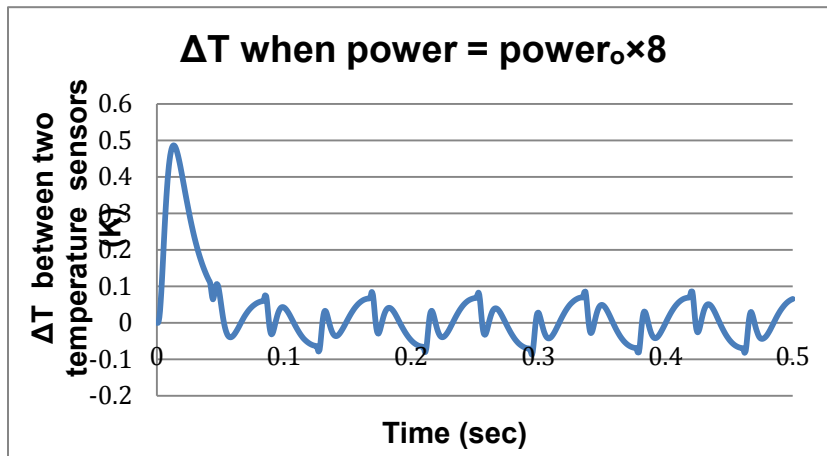
(f)  $\Delta T$  plot between two temperature sensors, power = power<sub>0</sub> × 2



(g)  $\Delta T$  plot between two temperature sensors, power = power<sub>0</sub> × 4



(h)  $\Delta T$  plot between two temperature sensors, power = power<sub>0</sub> × 6



(i)  $\Delta T$  plot between two temperature sensors, power = power<sub>0</sub> × 8

Figure 8-A  $\Delta T$  plot between two temperature sensors by varying power. Cavity filled with air and angular rate is 1rad/sec.